

**NASA CONTRACTOR  
REPORT**

**NASA CR-1774**



**NASA CR**

*C-1*

0061073

TECH LIBRARY KAFB, NM

**LOAN COPY: RETURN TO  
AFWL (DOGL)  
KIRTLAND AFB, N. M.**

**RECIRCULATION CHARACTERISTICS  
OF A SMALL-SCALE VTOL  
LIFT ENGINE POD**

*by Gordon R. Hall*

*Prepared by*

**NORTHROP CORPORATION**

Hawthorne, Calif.

*for Lewis Research Center*

**NATIONAL AERONAUTICS AND SPACE ADMINISTRATION • WASHINGTON, D. C. • MAY 1971**



0061073

1. Report No. <b>NASA CR-1774</b>	2. Government Accession No.	3. Recipient's Catalog No.	
4. Title and Subtitle <b>RECIRCULATION CHARACTERISTICS OF A SMALL-SCALE VTOL LIFT ENGINE POD</b>		5. Report Date <b>May 1971</b>	
		6. Performing Organization Code	
7. Author(s) <b>Gordon R. Hall</b>		8. Performing Organization Report No. <b>None</b>	
		10. Work Unit No.	
9. Performing Organization Name and Address <b>Northrop Corporation Hawthorne, California</b>		11. Contract or Grant No. <b>NAS 3-10498</b>	
		13. Type of Report and Period Covered <b>Contractor Report</b>	
12. Sponsoring Agency Name and Address <b>National Aeronautics and Space Administration Washington, D. C. 20546</b>		14. Sponsoring Agency Code	
15. Supplementary Notes			
16. Abstract  Reported herein are exhaust gas ingestion and recirculating flow field characteristics of a small-scale VTOL lift engine pod containing two simulated engines. Results are presented for tests designed to investigate transient development of the recirculating flow field, steady state ingestion and recirculating flow field characteristics, and dynamic simulation of takeoff and landing. The steady state test results include effect of nozzle height and spacing, effect of inlet and exhaust flow conditions, and effect of wind speed and direction.			
17. Key Words (Suggested by Author(s)) <b>VTOL airplane Hot gas ingestion</b>		18. Distribution Statement <b>Unclassified - unlimited</b>	
19. Security Classif. (of this report) <b>Unclassified</b>	20. Security Classif. (of this page) <b>Unclassified</b>	21. No. of Pages <b>112</b>	22. Price* <b>\$ 3.00</b>



## PREFACE

This report documents the results of an exploratory investigation of the effectiveness of various concepts designed to reduce hot gas ingestion in VTOL lift engines. The work was performed as a part of NASA Contract NAS 3-10498 entitled "Concepts to Reduce Hot Gas Ingestion in VTOL Lift Engines." This contract provided for a series of exploratory experimental investigations, the primary objective being to determine the relative effectiveness and merits of various exhaust gas ingestion suppression concepts for application to VTOL aircraft. Secondary objectives of the contract were: (1) to establish modeling criteria and test techniques required for proper simulation of full-scale VTOL recirculation and ingestion phenomena in small-scale investigations; and (2) to gain a better understanding of VTOL recirculating flow fields. The NASA Project Manager was Nestor Clough of the Lewis Research Center Special Projects Division.

The investigations were conducted with a small-scale lift engine pod model in which both dual turbojet and turbofan engines were simulated, and with a geometrically similar full-scale lift engine pod containing dual turbojet engines. Potential ingestion suppression concepts (which were limited to investigation in the small-scale tests) included: (1) shielding devices integral with the engine pod which act to deflect the reflected upwash gases away from the inlets; (2) concepts designed to alter the issuing exhaust jets (such as exhaust vectoring and jet suppression nozzles); and (3) ground plane platforms which alter the impingement process of the exhaust jets on the ground so that the potential upwash is laterally removed from the proximity of the engine pod.

Prior to performing the small-scale investigation of various ingestion suppression concepts, it was essential that the validity of small-scale investigations of recirculation and ingestion phenomena be demonstrated more thoroughly than has been demonstrated heretofore. Thus, program effort related to this objective was performed first, with the full-scale results of this effort documented separately in Reference 1 and the full-scale/small-scale scaling comparisons documented in Reference 2.

Further, it was essential to comprehensibly establish the ingestion and recirculating flow field characteristics for the baseline small-scale model prior to performing the investigation of ingestion suppression concepts. Reported herein are the results of the ingestion and recirculating flow field characteristics of the basic engine pod model.



## TABLE OF CONTENTS

SUMMARY . . . . .	1
INTRODUCTION . . . . .	4
SYMBOLS . . . . .	5
TEST FACILITY AND MODEL . . . . .	6
Test Facility . . . . .	6
Model . . . . .	7
INSTRUMENTATION . . . . .	9
PROCEDURE . . . . .	10
Test Conditions . . . . .	10
Test Procedure . . . . .	10
Data Reduction . . . . .	11
DISCUSSION . . . . .	12
Exhaust Jet Calibration . . . . .	12
Jet Pressure Profiles . . . . .	12
Jet Alignment . . . . .	13
Start-Up Tests . . . . .	14
Flow Field Development . . . . .	14
Thermal Environment . . . . .	15
Steady State Tests . . . . .	16
Ingestion Characteristics . . . . .	16
Ingestion Indices . . . . .	20
Ingestion Trends . . . . .	21
Pod Pressure Distribution . . . . .	24
Dynamic Simulation Tests . . . . .	27
Takeoff . . . . .	27
Landing . . . . .	28
SUMMARY OF RESULTS . . . . .	30
REFERENCES . . . . .	32

# RECIRCULATION CHARACTERISTICS OF A SMALL-SCALE VTOL LIFT ENGINE POD

By

Gordon R. Hall  
Northrop Corporation, Hawthorne, California

## SUMMARY

An investigation of the exhaust gas ingestion and recirculation flow field characteristics of a small-scale VTOL lift engine pod containing two simulated engines has been conducted. Results were obtained on the transient development of the recirculating flow field, steady state ingestion and recirculating flow field characteristics, and dynamic simulation of takeoff and landing.

### Flow Field Development

Development of the steady state recirculating flow field was found to occur within a few hundred milliseconds using either a trap door or exhaust vector door start-up technique. With the trap door start-up, the initial flow field develops in a non-symmetrical way due to superposition of the trap door motion on the spreading of the ground jet flow.

### Ingestion Characteristics

The inlet thermal environment was found to be highly sporadic, exhibiting closely spaced temperature spikes (up to about 150° F above ambient) which typically persisted for a small fraction of a second and encompassed anywhere from a small fraction of the inlet area to the majority of the inlet area. During time intervals between temperature spikes, the inlet thermal environment was typically ambient.

Correlation of the thermal environment along the sides of the pod (in the plane of the inlets) with the engine inlet thermal environment supports the concept of the upwash or fountain, being the predominant source of ingestion.

Ingestion levels (as measured by cumulative time average indices indicative of inlet temperature level, temperature distortion, and temperature rates of rise) were found to be independent of time over the data acquisition period of 30 seconds.

### Ingestion Trends

Ingestion was found to increase significantly with nozzle spacing, S/D, over the

range of  $S/D$  investigated ( $S/D = 4.90 - 9.80$ ). Ingestion was found to increase or decrease with model height above the ground plane,  $H/D$ , depending upon the values of  $H/D$  and  $S/D$ .

With headwind, ingestion was found to decrease significantly for wind speeds greater than about 10 MPH for turbojet exhaust conditions, becoming negligible at about 20 MPH. With crosswind, ingestion was found to increase significantly with ingestion levels for crosswinds of 30 MPH several times more severe than at low wind levels.

Inlet Mach number was found to have a significant effect on ingestion levels. Ingestion was found to be several times more severe for an inlet Mach number of 0.5 than for an inlet Mach number of 0.1.

Ingestion was found to be independent of exhaust pressure over the range investigated ( $P_n/P_\infty = 1.4 - 1.9$ ), and independent of exhaust temperature, when non-dimensionalized with respect to exhaust minus ambient temperature ( $T_n - T_\infty$ ), over the range investigated ( $T_n = 440^\circ\text{F} - 1200^\circ\text{F}$ ).

#### Upwash Strength

Pressure distributions on the undersurface of the pod indicated strong upwash flows, with impingement velocities in excess of 200 ft/sec at low values of  $H/D$ . Upwash strength was found to rapidly decrease with  $H/D$ , and with  $S/D$  at low values of  $H/D$ . At higher values of  $H/D$ , however, upwash strength was found to increase with  $S/D$ .

The strength of the upwash was found to correlate with the path length between the nozzle exit and the pod undersurface at low values of  $H/D$ . At higher values of  $H/D$ , however, entrainment of the upwash by the free jets was found to become the dominant factor governing upwash strength, rather than path length.

Pod pressure distribution (i. e., upwash strength) was found to be independent of exhaust temperature over the range investigated ( $T_n = 440^\circ\text{F} - 1200^\circ\text{F}$ ), and independent of exhaust pressure, when non-dimensionalized with respect to exhaust minus ambient pressure ( $P_n - P_\infty$ ), over the range investigated ( $P_n/P_\infty = 1.4 - 1.9$ ).

Significant reduction in upwash strength was found to occur with headwinds, while crosswinds had little effect on upwash strength.



### Dynamic Simulation

Simulated takeoff and landing tests, in which vertical motion of the model was programmed during the test, showed an instantaneous thermal environment qualitatively similar to that of the steady state tests, with ingestion becoming negligible at about the same value of  $H/D$  as for the steady state tests.

## INTRODUCTION

Direct-lift turbojet or turbofan engines, as well as cruise engines with thrust deflectors are contemplated for use as thrusters on VTOL aircraft. However, when the aircraft is in ground proximity, the engine exhaust gases, which are directed normal to the surface of the ground, can be deflected upward and ingested into the engine inlets.

Experimental work to date with turbojet engines operating as direct-lift thrusters has indicated that hot gas ingestion can be a serious problem (e. g., Reference 3-7), especially for split-engine configurations in which the wing location of the vehicle relative to the propulsion system is ineffective in shielding the engine inlets from the recirculating upwash flow. Ingestion of the recirculating exhaust gases by the engines is of concern due to the rather strong effect that hot gas ingestion can have on engine performance. In particular, ingestion of hot exhaust gases by the engines results in thrust degradation. Additionally, high rates of inlet temperature rise and/or large temperature distortions across the inlet face can result in engine compressor stall.

Recirculation of exhaust gases can also result in aerodynamic forces on the vehicle which arise from the direct impingement of ground plane reflected exhaust flows on the aircraft structure. Additionally, significant aerodynamic forces may result from the circulation of free air about the aircraft, the circulation being induced as a result of flow entrainment by the lifting jets and ground jet flows. Although the pressure levels resulting from induced free air circulation and impingement of reflected exhaust gases are generally low, the surface area is generally quite large. Hence, the total induced force can be large, having an appreciable effect on net lifting capability and aircraft balance in hover.

Reported herein are the results of an investigation of exhaust gas ingestion and recirculating flow field characteristics of a small-scale VTOL lift engine pod containing two simulated engines. Data are presented and analyzed for tests designed to investigate transient development of the recirculating flow field, steady state ingestion and recirculating flow field characteristics, and dynamic simulation of takeoff and landing.

## SYMBOLS

D	nozzle diameter
H	height of pod undersurface from ground plane
P	pressure
$\Delta P$	pod pressure minus ambient pressure
q	jet stagnation pressure minus ambient pressure
r	distance from nozzle centerline
R	nozzle radius
S	distance between nozzle centerlines
T	temperature
Z	vertical distance from nozzle exit

### Ingestion Indices

$\bar{T}$	instantaneous spatial average inlet temperature, $\bar{T} = \frac{1}{n} \sum_{i=1}^n T_i$ , where n equals number of inlet thermocouples
$\Delta \bar{T}$	instantaneous spatial average inlet temperature increment above ambient, $\bar{T} - T_{\infty}$
$\epsilon$	instantaneous temperature distortion within inlet, $T_{\max} - T_{\min}$
$\dot{\bar{T}}$	instantaneous rate of rise of spatial average inlet temperature

### Subscript

n	nozzle
$\infty$	ambient
c.l.	centerline

### Superscript

$\wedge$	time-average (applied to $\Delta \bar{T}$ , $\epsilon$ , and $\dot{\bar{T}}$ )
----------	--

## TEST FACILITY AND MODEL

### Test Facility

The tests were performed at Northrop Corporation, Aircraft Division, VTOL Ground Effects Test Facility. A brief description of this facility is given below, with Reference 8 providing details of the design features and performance capabilities.

Figures 1 and 2 show the facility and model support system. Test models are centrally located with respect to a 40' x 40' smooth and level ground plane located 30" above earth level. Directly below the model is a 14" x 30" trap door through which the exhaust jets flow during temperature stabilization of the model and ducting system. Beneath the trap door is a deflector which diverts the exhaust flow outward beneath the ground plane.

Test models are mounted on a cantilever structure supported by a tripod base. Simulated engine exhaust flow is supplied from bottles of compressed air (Figure 1) and heated to the desired exhaust temperature (up to 1200<sup>0</sup>F) in passing through a pebble bed heater enroute to the model. Simulated engine inlet flow is induced by a vacuum system. The model exhaust and inlet flows are routed along and through, respectively, the support structure. Vertical position of the model, or continuous motion simulating takeoff/landing transients, is accommodated by telescoping assemblies in the exhaust nozzle supply lines and by a flexible hose in the inlet suction lines.

The test area is large enough, and sufficiently vented, to avoid heating of the local "external" environment during periods of sustained testing. Additionally, all vertical obstructions are far enough removed from the exhaust jet source to avoid "jet reflection" effects. Wind protection in the test area is afforded by surrounding buildings and by installation of canvas wind screens (15' high) at the north and west ends of the test area as indicated in Figure 1. With the wind screens installed, local wind conditions within the test site are suppressed to levels typically less than 3 MPH during the morning and early afternoon.

Airflow to simulate wind effects is supplied from a 9' x 12' duct which terminates near the edge of the ground plane. The drive system of the wind generator is an ejector concept which provides secondary to primary airflow in the ratio of about 80 to 1, the secondary air being drawn from the atmosphere and the primary air being

provided by the same bottles of compressed air which supply the model exhaust flow. Uniform, low turbulence winds in excess of 30 MPH can be provided. Orientation of test models with respect to wind direction is achieved by rotation of the model support system.

### Model

The test model, a simulated VTOL lift engine pod containing two "engines," is shown in Figures 3 and 4. Figure 4 shows the model installed with vector doors ( $45^\circ$ ) which were used in the start-up procedure for selected tests rather than the ground plane trap door which was used in the nominal start-up procedure.

The nominal spacing between the two engines,  $S$ , in terms of the 2.25" nozzle diameters,  $D$ , was  $S/D = 7.35$ . Alternate engine spacings of  $S/D = 4.90$  and  $9.80$  were made possible by installation of alternate inlet/nozzle spacing plates forming the inlet and exhaust planes of the model.

Figures 5 and 6 show details of the model inlets and exhaust nozzles. Center-bodies were provided to give close simulation of full-scale inlet and nozzle flows. The inlet flow rate, with the inlets operating at a nominal inlet Mach number of 0.5, was approximately equal to the exhaust nozzle flow rate, when operating at the nominal turbojet and turbofan exhaust pressure ratios of  $P_n/P_\infty = 1.9$  and  $1.4$ , respectively, and nominal exhaust temperatures of  $T_n = 1200^\circ\text{F}$  and  $440^\circ\text{F}$ , respectively.

A perforated plate (.05" holes) was used to separate the exhaust flow supply duct from the nozzle chamber (Figure 6). The plate served to drop the pressure between the supply duct ( $\approx 80$  psia) and the nozzle chamber ( $\approx 26$  psia), thereby allowing a smaller supply duct cross section than would otherwise be required. The plate also eliminated problems of exhaust flow alignment which would have been severe without the plate due to limited space in which to turn the flow vertical within the model.

Inlet suction and exhaust flow were supplied at each end of the model with an internal partition separating the forward engine flow from the aft engine flow. Air suction systems at each end of the model were essential in order to attain the desired inlet flow without geometric distortion of the model, distortion being necessary to accommodate the duct size required for a "single end" suction system.

Heat absorption by the model (and therefore model heating and cooling time) was minimized by insulating the model structure from the hot exhaust flow. The insulation resulted in maximum model structure temperatures (with exception of the nozzle) of about 400° F.

## INSTRUMENTATION

1. Inlet Temperatures - The inlets of the model were instrumented with twelve high response bare bead thermocouples. The locations of the thermocouples were selected to represent equal flow areas within the inlet. The output of these thermocouples was recorded on FM magnetic tape.

The locations and details of construction of the inlet thermocouples are shown in Figures 5 and 7. The sensing element of the thermocouples was fabricated from .003" chromel/alumel wire. Based on Reference 9, the time constant for the thermocouple/flow environment combination was approximately 18 m.s. (or in terms of response to a sinusoidal input signal, flat response within 10 percent up to a frequency of about 5 cps), assuming an ideal butt weld junction through which the local thermal mass is not increased above that of the parent wire. Details of the design considerations relating to the construction concept, junction wire size, junction material, and operational reliability are given in Reference 1.

2. Inlet Proximity Temperatures - Twelve high response bare bead thermocouples (identical to those in the inlets) were cantilevered from the sides of the model in the plane of the inlets (Figure 8). These thermocouples, which were recorded on oscillograph, were located to measure the temperature (and longitudinal concentration) of the upwash flow between the engines.

3. Pod Pressures - Pressure taps were located on the lower surface of the model along the longitudinal centerline (Figure 9). These pressure measurements provided information on the strength and location of the upwash flow between the exhaust jets.

4. Exhaust Measurements - Exhaust nozzle pressure and temperatures were measured with high response sensing elements (three per nozzle ganged together for a single output) and recorded on oscillograph. Figures 6 and 10 show the exhaust nozzle instrumentation detail.

5. External Wind - External wind speed, azimuth, and elevation were monitored prior to testing and recorded continuously on oscillograph during the tests.

## PROCEDURE

### Test Conditions

Table 1 presents a list of the various tests reported. The total test series is broken down into three subcategories as indicated in Table 1. The objective of the first test series (Start-Up Tests) was to evaluate the effects of various start-up techniques on the initial development of the near flow field and ingestion characteristics. The objective of the second series of tests (Steady State Tests) was to investigate the effect of model height ( $H/D$ ) and nozzle spacing ( $S/D$ ), effect of inlet and exhaust flow conditions, and effect of wind speed and direction. The third test series (Dynamic Simulation Tests) provided simulation of takeoff and landing conditions in which model motion occurred during the tests.

### Test Procedures

Prior to each of the tests, external wind conditions were monitored. For the nominally "no wind" tests, wind conditions were less than 3 MPH within the test area. For the "wind" tests, wind velocity was controlled using the wind generator described previously.

Once the desired ambient wind condition was attained, the inlet suction system was set to give an inlet Mach number of 0.5 (nominal), after which time the model and test facility ducting was preheated to the desired exhaust temperature. Upon establishing the desired exhaust conditions, the wind generator was set to give the desired wind velocity (for wind tests only) after which time data acquisition was initiated and the ground plane trap door closed (or model vector doors released for tests using the vector door start-up technique). The trap door closure time was about 150 m.s. and vector door release time approximately 40 m.s. Data acquisition subsequent to trap door closure was typically 40 seconds for the steady state tests.

For the takeoff tests of the dynamic simulation test series, controlled exhaust pressure transients and model motion were programmed to follow model vector door release, the programming accomplished through an automatic sequencing device. For the landing tests of this series, model motion was programmed to follow trap door closure.



## Data Reduction

Data reduction techniques applied to the inlet temperature data were oriented toward statistical analyses due to the random, or fluctuating, nature of the data. For data of this type, a statistical oriented approach to data analysis is essential for objective characterization of the data.

As noted previously, the inlet temperatures were sensed with high response thermocouples and recorded on magnetic tape. For each of the tests, the raw inlet temperature data were played back on analog tapes. In addition, the following temperature indices, yielding quantitative information on the inlet temperature levels, temperature distortion, and temperature rate of rise, were computed from the raw data for each of the steady state tests using a Comcor 175 Analog Computer.

(1) The instantaneous spatial average of the  $n$  individual temperatures within the inlet:

$$\bar{T}(t) = \frac{1}{n} \sum_{i=1}^n T_i(t)$$

(2) The cumulative time-average of (1).

(3) The instantaneous temperature distortion within the inlet:

$$\epsilon(t) = T_{\max}(t) - T_{\min}(t)$$

(4) The cumulative time-average of (3).

(5) The instantaneous rate of rise of (1):

$$\dot{\bar{T}}(t) = \frac{d\bar{T}}{dt}$$

(6) The cumulative time-average of the absolute value of (5).

## DISCUSSION

### Exhaust Jet Calibration

Prior to conducting the tests indicated in Table 1, calibrations of the jet exhausts were made. These calibrations are relevant to subsequent recirculation effects. This was borne out in the findings of Reference 10 which demonstrated that recirculation effects are extremely sensitive to jet exit angles and moderately sensitive to jet dynamic pressure decay (i. e., turbulence) characteristics.

#### JET PRESSURE PROFILES

Dynamic pressure profiles (i. e., jet total less ambient pressure) of the jets were measured at various distances,  $Z$ , from the nozzle exit using a cruciform pressure rake with probes aligned to measure the jet pressure profiles in the fore-aft plane and in the right/left plane (Figure 11). Measurements were made from the nozzle exit up to  $Z/D$  of about 10, with the rake aligned such that the center probe of the cruciform was approximately coincident with a plumb line suspended from the nozzle centerline. The measurements were taken at the nominal turbojet and turbofan exhaust pressure ratios of  $P_n/P_\infty = 1.9$  and  $1.4$ , respectively, and nominal exhaust temperatures of  $T_n = 1200^\circ\text{F}$  and  $440^\circ\text{F}$ , respectively.

The dynamic pressure profiles,  $q$ , nondimensionalized with respect to the dynamic pressure measured within the nozzle,  $q_n$ , are shown in Figures 12 (turbojet) and 13 (turbofan). The depression in the dynamic pressure in the central region of the jets at lower values of  $Z/D$  is indicative of flow separation from the nozzle centerbody. At larger values of  $Z/D$ , the relatively localized effects of the centerbody are not apparent, with the pressure profiles resembling a distribution characteristic of the asymptotic profiles for a conventional open nozzle.

Figure 14 shows the variation in jet centerline dynamic pressure with  $Z/D$ . For comparative purposes, the dynamic pressure decay for a 3" open nozzle supplied by a plenum (i. e., low initial turbulence level) is also shown. Reservoir conditions for the reference nozzle (Reference 11) were  $T_n = 1200^\circ\text{F}$  and  $P_n/P_\infty = 2.0$ . The effect of the nozzle centerbodies is clearly apparent at the smaller values of  $Z/D$ . At the larger values of  $Z/D$ , the rate of dynamic pressure decay is seen to be similar to that of the small-scale reference nozzle.

## JET ALIGNMENT

At the larger values of  $Z/D$ , a small offset of the dynamic pressure peak from vertical (i. e.,  $r/R = 0$ ) is generally observed in Figures 12 and 13. These offset values in the dynamic pressure profiles were used to determine the alignment of the jets relative to vertical, assuming the jet centerline to be defined by the locus of the dynamic pressure peaks. Based on this method, the maximum misalignment of the jets relative to vertical was determined to be less than one degree.

Alternate methods to determine the alignment of the jets were also employed. For example, Figure 15 shows the results of an oil streak technique in which a small pool of oil (approximately equal to the nozzle exit diameter) was placed on the ground plane directly below each of the nozzles. The jets were then turned on, allowing the oil to smear under the viscous action of the radially spreading ground jets. The resulting pattern is essentially radial, except in the region of the interaction plane midway between, and perpendicular to a line joining, the nozzle centerlines. In this region, the opposing ground jet flows meet and are turned outward and upward.

Also indicated in Figure 15 is a vertical projection of the nozzle centerline. Based on the displacement of the jet stagnation points (i. e., convergence point of the radial streak lines) from the vertical projection of the nozzle centerlines, and on the height of the model above the ground plane, the jet misalignment from vertical may be determined. Based on this method, which was performed at reduced exhaust pressure and temperature conditions, the jet alignment, relative to vertical, as before, was determined to be slightly forward and to the right with a resultant misalignment of less than one degree.

Figure 16 shows a flow visualization photograph of the issuing jets with the ground plane trap door open. The visualization was obtained by injecting a small quantity of oil into the hot jets at the nozzle exit, thereby resulting in vaporization and combustion. Although less accurate than the preceding techniques of determining the jet alignment, the results tend to confirm the previous misalignment values. Additionally, the jet spreading as indicated in Figure 16 is in good agreement with the quantitative jet spreading data of Figures 12 and 13.

## Start-Up Tests

Tests were conducted with the objective of evaluating effects of various start-up techniques on the initial development of the near flow field and ingestion characteristics (Table 1-A). Techniques investigated included tests in which turbojet exhaust conditions were established (i. e.,  $P_n/P_\infty = 1.9$ ,  $T_n = 1200^\circ\text{F}$ ) with the ground plane trap door open, followed by trap door closure. The trap door closure time was about 150 m. s.

Similar tests were performed using exhaust vectoring doors in lieu of the ground plane trap door. Figure 17 shows detail of the model vector door in the "vectored" ( $45^\circ$ ) mode. The vector door was released using a "burn-wire" technique in which the wire restraining the door was burned by a discharge of electrical current. The vector door release time from  $45^\circ$  to fully retracted was approximately 40 m. s.

Tests were also performed using the trap door and vector door techniques in conjunction with an exhaust pressure transient. For these tests, the exhaust pressure ratio prior to actuation of the trap door/vector door was  $P_n/P_\infty = 1.2$  (corresponding to an engine idle condition). Following actuation of the trap door/vector door, the exhaust pressure ratio was then increased to the nominal turbojet exhaust pressure ratio of  $P_n/P_\infty = 1.9$  by use of a fast-acting hot gas control valve.

Each start-up mode was run three times for evaluation of repeatability. In addition, separate flow visualization tests were conducted for each start-up mode investigated.

### FLOW FIELD DEVELOPMENT

Figures 18 and 19 show profile and end views, respectively, of the development of the flow field following initiation of trap door closure (corresponding to  $t = 0$ ). Visualization of the flow field was obtained by injecting a small quantity of oil into the exhaust jets at the nozzle exit. Data taken during these tests were limited to flow visualization due to the unknown effect of the oil combustion on the thermal environment of the near flow field. Documentation was obtained on high speed movie film. The data of Figures 18 and 19 are enlarged frames from the high speed movie film.

Between  $t = 0$  and  $t = .08$  seconds in Figures 18 and 19, the issuing jets flow unimpeded through the trap door opening and are deflected parallel to the ground by a deflector beneath the ground plane. At  $t = .08$ , the trap door first intercepts the exhaust jets in closing from right to left in the end view (Figure 19). At this time, an

upflow of exhaust gases midway between the jets is initiated, with the upflow on the right side of the model (behind the model in the profile view) slightly leading the upflow on the left side of the model. As time progresses, the flow field (which can be considered to be composed primarily of a ground jet flow and an upwash in the region between the jets) continues to develop in a relatively symmetrical way in the profile view and in a non-symmetrical way in the end view, until the model is completely enveloped in an environment contaminated with the exhaust gases.

The non-symmetrical development of the flow field in the end view is due to the right-to-left motion of the trap door superimposed on the spreading of the ground jet flow. The result is that the ground jet spreads considerably more rapidly to the left of the model than to the right prior to full closure of the trap door, which occurs at  $t = .15$  seconds. Beyond  $t = .15$ , the flow spreads to the left and right at equal rates until a symmetrical equilibrium flow pattern is developed as seen at  $t = .30$  seconds. Beyond  $t = .30$  seconds, the dynamic flow pattern changes very little although some of the smoke continues to rise as a result of buoyancy forces. It is also of interest to note that the initial rapidly rising column of smoke on the right side of the model is a part of the transient development of the flow which fades away as the equilibrium flow pattern is established.

### THERMAL ENVIRONMENT

Figures 20 through 23 show time histories of the inlet and inlet proximity thermal environment during the first four seconds following start-up for each start-up technique. The time scale reference value of  $t = 0$  corresponds to initiation of trap door/vector door motion prior to which the thermal environment is essentially ambient.

Figure 20 shows data for a trap door start-up at turbojet exhaust conditions. These conditions correspond to the flow field development data of Figures 18 and 19. Note that the initial temperature rise on the right side of the model as indicated in Figure 20 occurs at approximately  $t = .08$  seconds, corresponding to the initial upwash pulse of Figures 18 and 19. The initial temperature rise on the left side of the model is seen to lag that of the right side and the gradient is less. Last to respond is the inlet, represented by  $\bar{T}$ , which is the instantaneous spatial average of the twelve individual thermocouples located within each of the inlets.

Due to the sporadic nature of the thermal environment, it is not possible to accurately determine the time to establish the "steady state" flow field. However,

based on the flow field development movies and on quantitative data like those of Figure 20, the near flow field may be assumed to be fully established within a few hundred milliseconds from  $t = 0$ .

Figure 21 shows data similar to that of Figure 20 except that the initial value of exhaust pressure ratio is  $P_n/P_\infty = 1.2$  corresponding to an engine idle condition. At  $t = 1.2$  seconds, the exhaust pressure is increased to  $P_n/P_\infty = 1.9$  in less than a second by use of a fast-acting hot gas control valve. The exhaust temperature is maintained at approximately  $1200^\circ\text{F}$  throughout the test.

The initial temperature transients following initiation of trap door closure are seen to be similar to those of Figure 20 in which the exhaust pressure ratio was maintained at  $P_n/P_\infty = 1.9$  throughout. Further, there is no obvious change in the thermal environment which can be directly attributed to the exhaust pressure transient beginning at  $t = 1.2$  seconds.

Figures 22 and 23 show similar data using the vector door start-up technique. For the vector door start-up, the thermal environment in the proximity of the inlets reacts almost immediately upon retraction of the vector doors. Both the right and left sides of the model respond simultaneously and with a lower initial gradient than for the trap door start-up of Figures 20 and 21. As for the trap door start-up, the flow field would appear to be fully established within a few hundred milliseconds from  $t = 0$ . Also, there is no obvious effect of the exhaust pressure transient (Figure 23) except that the temperature field shifts aft.

#### Steady State Tests

#### INGESTION CHARACTERISTICS

Figures 24 through 28 show time histories from various tests which illustrate the basic character of the inlet thermal environment for two engine and single engine operation, including the effect of wind. The data were obtained by playback of the raw data from magnetic tape.

Although the data presented are for turbojet exhaust conditions at  $H/D = 4$  and  $S/D = 7.35$ , they are generally characteristic of operation at turbofan exhaust conditions and other values of  $H/D$  and  $S/D$ , with differences being predominantly in the levels of the data rather than in the general character of the data. The data are also representative of full scale ingestion characteristics as seen in Reference 1 which reports the ingestion characteristics of a geometrically similar, and similarly in-

strumented, full-scale engine pod model.<sup>1</sup>

### Two Engine Operation

Figures 24, 25, and 26 show time histories of the inlet temperature environment for two engine operation at low wind, 20 MPH headwind, and 20 MPH crosswind, respectively.

Low Wind - For low wind conditions in which the exhaust gas ingestion is dominated by the upwash, or fountain, resulting from mutual interaction of the jets and the ground plane (Figure 15), several general characteristics of the data are immediately obvious. First of all, it is observed that the forward inlet is essentially at the pre-run ambient temperature throughout the test with the exception of some occasional temperature spikes after trap door closure (i. e.,  $t = 0$ ). In contrast, the aft inlet is significantly above the pre-run ambient temperature throughout the test.

Non-symmetrical distribution of exhaust ingestion by the inlets as indicated by Figure 24 was also found to be typical at low wind conditions at other values of  $H/D$  and  $S/D$ , at other exhaust conditions, and found to occur in full-scale tests with a similar configuration (Reference 1). Due to geometric symmetry of the model in the region between the inlets, the ingestion prone inlet was found to vary from test to test. In a few tests, the ingestion was found to shift from one inlet to the other within the test.

The non-symmetrical distribution of exhaust gas ingestion in a configuration with geometric symmetry at low wind conditions is the result of the low stability characteristics of the upwash which, when coupled with the inlet suction flow field, results in a fluid amplifier effect. The net result occurring within the combined upwash/inlet flow field is an unstable upwash flow which is predominantly entrained within one inlet or the other as indicated in Figure 29, the particular inlet depending upon such small biases such as slight differences in the exhaust jet pressure levels, minor angular misalignment of the jets with respect to the ground plane, and random wind effects. For more detailed discussion of these effects on upwash stability, the reader is referred to Reference 10. For discussion of additional aspects of non-symmetrical ingestion as related to full-scale tests, the reader is referred to Reference 1.

---

<sup>1</sup>Detailed comparisons of full-scale/small-scale recirculation characteristics as related to scaling are presented in Reference 2.

Another obvious characteristic of the data of Figure 24 is the sporadic nature of the inlet temperature environment. Temperature spikes are observed which typically persist for a small fraction of a second, and frequently reach levels in excess of  $100^{\circ}\text{F}$  above ambient. These temperature spikes, or pulses, are sometimes very local in nature as evidenced by simultaneous response of only a few thermocouples, while at other times they are observed to encompass a large section of the inlet as evidenced by simultaneous response of the majority of the thermocouples. During time intervals between temperature spikes, the temperature level is typically ambient. In no test was a prolonged temperature rise observed which could be considered a "steady" temperature, rather than a series of closely spaced temperature pulses.

Similarly, the upwash temperature environment in the proximity of the inlets, as measured by the instrumentation indicated in Figure 8, was found to exhibit temperature fluctuation characteristics much like those of the inlets (e.g., Figures 20 through 23). The inlet proximity traces, however, were found to be somewhat "smoother" than the inlet traces due to the lower velocity of the flow past the thermocouples, the flow velocity affecting both the thermocouple response and the passage time of hot gas bubbles for a given spatial temperature gradient. The result is that local fluctuations in the range of  $50^{\circ}\text{F}$  -  $100^{\circ}\text{F}$  were observed, with peak fluctuations up to about  $150^{\circ}\text{F}$ . Further, the relative level of thermal activity in the proximity of the inlets was found to correlate with the inlet environment in that the activity in the proximity of the ingestion prone inlet was found to be considerably greater than that in the proximity of the non-ingestion prone inlet.

Analysis of the inlet and inlet proximity thermal environments suggests an upwash model composed predominantly of large clumps of hot gas (as evidenced by the simultaneous response of several inlet proximity thermocouples). In approaching the inlet, acceleration of the flow results in stretching of the clumps, or bubbles, into elongated stream tubes which may occupy anywhere from a very small fraction of the inlet cross section to the major portion of the inlet cross-section.

Headwind - Figure 25 shows the inlet temperature environment for two engine operation with a 20 MPH headwind. Major reduction in ingestion levels from the low wind data of Figure 24 is observed. Specifically, the forward inlet (i.e., upstream with respect to the wind) shows minor temperature pulses, typically less than  $25^{\circ}\text{F}$ , distributed over the entire inlet. The aft inlet (i.e., downstream with respect to the



wind) typically shows somewhat sharper, higher level, temperature pulses which are more spatially localized.

The more uniform temperature pulses observed in the forward inlet indicate a well mixed flow of exhaust gases which are swept up from the ground plane in the far field and blown back over the pod. The sharper, more localized pulses of the aft inlet indicate an upwash which, although predominantly suppressed and deflected by the wind, is occasionally entrained within the inlet flow.

The above physical model of the flow field with headwind is supported by the high speed movie documentation. Visualization of the flow field was obtained by injecting a small quantity of oil into the exhaust jets at the nozzle exit following acquisition of the inlet thermal data. Figure 30 shows enlarged frames from a high speed movie showing the interaction of the wind with the forward flowing ground jet.

At the 10 MPH wind speed (Figure 30a), the ground jet is seen to flow out of the field of view while still attached to the ground plane. At a point outside of the field of view, the ground jet dynamic pressure decays to a value such that the jet separates from the ground plane and flows back toward the model, eventually completely enveloping the model (note that Figure 30a is a frame taken during the transient flow of the smoke, whereas at steady state, the entire frame is darkened with smoke).

At the 20 MPH and 30 MPH wind speeds (Figures 30b and 30c, respectively), the separation point of the ground jet from the ground plane is clearly seen, with the separation point closer to the model at the higher wind speed and the trajectory of the back flowing exhaust gases lower. Figures 30b and 30c, unlike Figure 30a, correspond to steady state flow visualization.

Crosswind - Figure 26 shows the inlet temperature environment for two engine operation with a 20 MPH crosswind. The fluctuating character of the data observed at low wind continues to persist at crosswind conditions. The ingestion is more severe and, unlike the low wind data, was found to be relatively evenly distributed within the two inlets. The increased severity and the relatively symmetrical distribution of ingestion in both inlets were found to be typical at all values of  $H/D$  and at turbofan exhaust conditions for crosswind conditions.

Figure 31 shows the interaction of the crosswind with the ground jet flow. The effect of the crosswind on the ground jet flow is seen to be qualitatively similar to the

headwind data of Figure 30, but with the point of ground jet separation from the ground plane occurring farther from the model and the trajectory of the backflowing exhaust gases being higher than for the corresponding headwind. The ground jet separation point is farther from the model due to the reinforced ground jet in the cross flow direction as determined previously in Reference 1. The high trajectory is due to the fact that the crosswinds, in flowing parallel to the upwash, have little effect on the strength of the upwash as will be shown in later discussions of the upwash strength.

### Single Engine Operation

Figures 27 and 28 show the inlet temperature environment for single operation for low wind and 20 MPH headwind, respectively.

Low Wind - In contrast to the data of Figure 24 (typical of operation with two engines at low wind) are the data of Figure 27, which are typical of single engine operation at low wind conditions. For single engine operation, the engine exhaust jet strikes the ground, spreads radially along the ground, and eventually rises as a result of buoyancy forces. The resulting ingestion level is low, with localized peak temperatures generally less than  $10^{\circ}\text{F}$  above ambient.

Headwind - At high wind conditions with single engine operation (Figure 28), ingestion characteristics were found to be much like those for upstream engine for two engine operation at high wind conditions. Namely, temperature pulses typically less than  $25^{\circ}\text{F}$  are frequently observed, the pulses being distributed over the entire inlet and resulting from exhaust gases which are swept up from the ground plane in the far field and blown back over the pod as discussed previously for headwind conditions with two engine operation.

## INGESTION INDICES

### Instantaneous Indices

Figures 32 through 36 present time histories of the spatial average inlet temperature ( $\bar{T}$ ), the temperature distortion within the inlet ( $\epsilon$ ), and the rate of rise of the spatial average temperature ( $\dot{\bar{T}}$ ), obtained from the raw data of Figures 24 through 28.

Since the temperature spikes observed in the raw data are generally localized, the corresponding peak values of  $\bar{T}$  are accordingly less than the localized peak values

of the individual temperatures observed in the raw data. Thus, traces of  $\bar{T}$ , while still rather sporadic in nature, are considerably smoother than the individual temperature traces of the raw data. The generally localized nature of ingestion is also indicated by the distortion parameter,  $\epsilon$ , which frequently shows large values of temperature distortion without significant increase in  $\bar{T}$  above the pre-run ambient temperature level.

### Cumulative Time-Averages

The instantaneous temperature indices for each of the steady state tests of Table 1-B were cumulatively time averaged in order to provide a single run-average index for each of the fluctuating quantities  $\bar{T}$ ,  $\epsilon$ , and  $\dot{\bar{T}}$ . These time-average quantities were obtained by continuous integration and division by time using an analog computer, the computing process beginning 2 seconds following trap door closure and continuing for 30 seconds thereafter.<sup>1</sup> For the case of  $\dot{\bar{T}}$ , the integral taken was that of the absolute value rather than of the algebraic value (the integral of the algebraic value of  $\dot{\bar{T}}$  must be zero unless there is a net increase in  $\bar{T}$  with time).

The cumulative time averages of  $\bar{T}$ ,  $\epsilon$ , and  $\dot{\bar{T}}$  were found to be independent of the period of computation (provided the period of computation was greater than a couple of seconds which was required to dampen fluctuations of the instantaneous quantities). That is, although the quantities  $\bar{T}$ ,  $\epsilon$ , and  $\dot{\bar{T}}$  are of a highly fluctuating nature on a short time basis, there was no net change in the average value of these quantities over the duration of the tests (i. e., the data were stationary in statistical terms). Thus, run-average indices, which are independent of time and representative of inlet temperature level ( $\Delta \hat{\bar{T}}$ ), temperature distortion ( $\hat{\epsilon}$ ), and temperature rate of rise  $|\hat{\dot{\bar{T}}}|$ , are provided for each of the steady state tests.

### INGESTION TRENDS

Figures 37 through 44 show ingestion trends for two engine operation in terms of the above-described run-average indices  $\Delta \hat{\bar{T}}$ ,  $\hat{\epsilon}$ , and  $|\hat{\dot{\bar{T}}}|$ . The data shown are for the ingestion prone inlet except at crosswind conditions. At crosswind conditions, the distribution of ingestion between the two inlets was found to be relatively equal (as discussed previously) in which case the data represent the average value for the two

---

<sup>1</sup>In a few tests, the ingestion was found to shift from one inlet to the other during the test. For these tests, the averaging was performed over a suitable time interval during which the ingestion remained stabilized within one inlet.

inlets. In general, the trends indicated by each of the indices  $\Delta \hat{T}$ ,  $\hat{\epsilon}$ , and  $|\hat{T}|$  were found to be similar.

### Turbojet Operation

Figures 37 through 39 show effects of H/D, S/D, and wind at turbojet exhaust conditions. As can be seen in Figure 37, the effect of S/D is quite pronounced, with increased ingestion associated with increase in S/D at all values of H/D. At S/D = 9.80, ingestion is seen to decrease with increasing H/D; however, even at the highest value of H/D tested, ingestion is more severe than at any value of H/D for lesser values of S/D.

At S/D = 7.35, ingestion is seen to generally decrease with H/D with the exception of a hump in the curves in the region from H/D = 4-6. This hump was also observed in the full-scale/small-scale results of Reference 2 (also at S/D = 7.35) which showed good agreement between the full-scale and small-scale data.

At S/D = 4.90, a rather peculiar trend with H/D is indicated. Ingestion is seen to be most severe at H/D  $\approx$  6 and rapidly decreases with either a decrease or increase in H/D, becoming negligible at H/D = 2 and H/D = 8. This trend (as are all the trends of Figures 37 through 44) is confirmed by the inlet proximity thermocouple instrumentation indicated in Figure 8.

Although the low ingestion at H/D = 2 for S/D = 4.90 is not completely understood, it is speculated that the velocity of the upwash (which is maximum for this configuration as will be shown later) is too high to be susceptible to the suction effect produced by the flowing inlets and/or the high velocity/highly coherent upwash at this condition is effectively deflected away from the inlets as a result of the impingement process on the undersurface of the pod. The former explanation was found to be the case in Reference 10 in which an image plane was placed midway between two simulated lift engines. The effect of the image plane was to significantly increase the strength of the upwash, with a resulting significant decrease in the level of hot gas ingestion by the inlets.

Figure 38 shows the effect of wind on ingestion. The data show significant reduction in ingestion for headwinds greater than about 10 MPH, with ingestion becoming negligible at about 20 MPH as discussed previously for the time histories of the raw inlet temperature data.

The effect of crosswind, however, is adverse (also discussed previously for the time histories of the raw inlet temperature data). The inlet temperature level ( $\Delta \hat{T}$ ) is seen to increase with increasing wind speed, until at 30 MPH, the level becomes about three times more severe than the low wind level. The effect on temperature rate of rise ( $|\hat{T}|$ ) is even greater. The distortion ( $\hat{\epsilon}$ ), however, is relatively unaffected by the crosswind. This is due to the fact that much of the ingestion occurring with crosswind results from backflow of well mixed exhaust gases across the model (i.e., Figure 31).

Figure 39 shows the effect of a 20 MPH wind over the range of H/D investigated. Ingestion is seen to be negligible at all values of H/D with the 20 MPH headwind, while the 20 MPH crosswind aggravates the ingestion problem (with the exception of the distortion as indicated above) at all values of H/D.

### Turbofan Operation

Figures 40 and 41 show the effect of H/D and wind at turbofan exhaust conditions. The trends are virtually identical to those for turbojet exhaust conditions, but the ingestion levels are lower due to the cooler turbofan exhaust temperature (440<sup>0</sup>F as opposed to 1200<sup>0</sup>F). Specifically, the hump in the curves in the region of H/D = 4-6 is again confirmed for the nozzle spacing of S/D = 7.35. In addition, the effects of headwind and crosswind are similar to those at turbojet exhaust conditions, except that ingestion is considerably more sensitive to headwinds due to the reduced strength of the upwash at turbofan exhaust conditions.

### Effect of Inlet and Exhaust Conditions

Figure 42 shows the effect of inlet Mach number on ingestion. The data show a rather strong effect of inlet Mach number, with ingestion levels reduced by a factor of about two for a decrease in inlet Mach number from 0.5 to 0.2. It is noted that this result is opposed to that of Reference 10 which concluded that there was little effect of inlet Mach number for a pair of simulated engines at about the same S/D and H/D as reported here, but without an interconnecting pod (i.e., the engines were isolated). Although the difference in the two results is not fully understood, it is conjectured that the pod, in blocking and reducing the strength of the upwash, renders the upwash flow more susceptible to changes in the inlet suction strength.

Figure 43 shows the effect of varying exhaust conditions on ingestion. A matrix

of nine exhaust conditions was tested varying from a turbofan pressure/temperature combination to a turbojet pressure/temperature combination. The data show the ingestion is relatively independent of exhaust pressure level over the range investigated but is strongly dependent on exhaust temperature.

Figure 44 shows the same data as Figure 43, but with the ingestion indices divided by the exhaust to ambient temperature differential,  $T_n - T_\infty$ . When correlated in this manner, the data are seen to be independent of exhaust temperature as well as exhaust pressure. This result is consistent with the findings of Reference 10 in which the same conclusion was reached. Also, this result has implications with respect to modeling of ingestion phenomena in facilities where real engine exhaust conditions are not attainable.

## POD PRESSURE DISTRIBUTION

### Two-Engine Operation

Low Wind - At low wind conditions, the ground jets in the region between the engines flow toward one another, eventually interacting in the plane midway between the jet centerline (Figure 15). Within the interaction process, the ground jet flows are turned outward and upward as indicated in Figure 45. The upward flow continues unimpeded until reaching the undersurface of the pod, where it impinges and is deflected around, and up, the sides of the pod.

It is noted that although ingestion was generally found to be significant in one engine or the other for two engine operation, but not in both, the upwash between the ground plane and the pod was found to be relatively symmetrical, with the upwash asymmetry discussed previously occurring between the pod undersurface and the plane of the inlets.

The upwash of exhaust gases produces a pressure field on the vehicle undersurface which can, in general, result in significant force levels when considering the total surface area affected. Characteristic of the pressure distribution for two engine operation is a positive pressure field approximately midway between the engines, with a negative pressure field on either side, the level of the pressure field being strongly dependent on  $H/D$  and  $S/D$ . The positive pressure field results from impingement of the upwash flow, or fountain, on the engine pod at velocities in excess of 200 fps at the lower values of  $H/D$ . The negative pressure field on either side of the positive

pressure field results from high mass flow entrainment by the jets (and, to a lesser extent, entrainment by the upwash flow), coupled with limited area from which to draw the free air necessary to satisfy the scavenging characteristics of the jets (Figure 45).

Figures 46 and 47 show the effect of  $H/D$  and  $S/D$  on the pressure field on the undersurface of the pod for turbojet exhaust conditions. The data show a rapid decline in the strength of the upwash with increasing  $H/D$  and with increasing  $S/D$  at low values of  $H/D$  (i. e.,  $H/D \lesssim 5$ ). At the higher values of  $H/D$ , however, the trend with  $S/D$  reverses, showing an increase in upwash strength with increasing  $S/D$ . Note that the upwash strength is maximum at  $H/D = 2$  and  $S/D = 4.90$  where ingestion, as discussed previously, was found to be negligible.

The decrease in upwash strength with  $H/D$  and  $S/D$  at low values of  $H/D$  is primarily the result of the increase in path length, and associated mixing, of the exhaust gases in traveling from the exhaust nozzle to the undersurface of the pod. The path length effect is overridden at higher values of  $H/D$ , however, where closer spacing of the nozzles results in a merging tendency of the free jets (Figure 16), and more importantly for the combinations of  $H/D$  and  $S/D$  tested, results in an increased influence of the entrainment field produced by the free jets due to the reduced strength of the upwash. Thus, the entrainment field of the jets has a significant retarding effect on the upflow of exhaust gases which can result in entrainment of the upwash back into the jets before reaching the undersurface of the pod (e. g.,  $H/D > 7$  at  $S/D = 4.90$  in Figure 47).

The effect of path length between the exhaust jets and the pod undersurface is shown in Figure 48 in which the upwash strength is correlated in terms of the path length  $2H + S/2$ . The correlation is seen to be quite good at the lower values of  $H/D$ . At the higher values of  $H/D$ , however, the path length correlation breaks down due to the aforementioned jet merging and entrainment effects.

Figures 49 and 50 show the effect of exhaust conditions on the pressure distributions. Figure 49 compares data for turbojet and turbofan exhaust conditions. The turbojet and turbofan data are qualitatively similar, with the turbofan pressure distributions being lower due to the lower exhaust pressure level.

Figure 50 shows pressure distributions for a matrix of exhaust conditions covering the pressure/temperature range from turbofan to turbojet exhaust conditions. The data are non-dimensionalized with respect to the difference between the exhaust jet

pressure and ambient pressure. Excellent correlation is obtained in showing that the pressure distributions are essentially independent of exhaust pressure when non-dimensionalized as shown, and also independent of exhaust temperature level. In addition, as would be expected, the pressure distributions were found to be independent of inlet Mach number.

Effect of Wind - Figures 51, 52, and 53 show the effect of wind speed and direction on the pod undersurface pressure for turbojet and turbofan exhaust conditions. The data show significant reductions in the strength of the upwash with headwind (i. e., wind normal to the plane of the upwash), while the crosswind (i. e., wind parallel to the plane of the upwash) has a much lesser effect. The turbojet and turbofan data are qualitatively similar, with the turbofan data being more sensitive to wind due to the reduced strength of the upwash at low wind conditions.

Figures 54 and 55 show the variation in pod pressure with  $H/D$  at high wind for turbojet exhaust conditions. The strong effect of the headwind relative to crosswind noted above is seen to prevail over the range of  $H/D$ , with the data indicating total suppression of the upwash flow for  $H/D > 6$  with the 20 MPH headwind.

#### Single Engine Operation

Figure 56 shows pressure distributions, including the effect of wind speed, for single engine operation at turbojet and turbofan exhaust conditions. For single engine operation at low wind, the induced pressure on the pod undersurface results from induced circulation set up by entrainment of free air by the jet, the resulting induced pressure distribution being considerably less than for two engine operation (note the change in scale of Figure 56 from the previous figures), and decreasing with distance from the operating engine.

With headwind, the pressure field downstream of the exhaust jet is similar to flow in the near wake of a bluff body in that the exhaust jet presents a cylindrical blockage to the wind. The result is a separated base flow region downstream of the jet in which the negative pressure field increases with wind speed. For the turbojet data, wake closure is indicated by the abrupt rise in pressure near the aft nozzle.



## Dynamic Simulation Tests

A series of tests was conducted in which takeoff and landing transients were simulated by preprogrammed vertical motion of the model (Table 1-C). For the take-off tests, the vector door start-up technique was used followed by an exhaust pressure transient from idle to full power, and subsequently, by model motion taking the model from an initial height of  $H/D = 4$  up to  $H/D \approx 18$ . The average vertical acceleration of the model during the height transients was approximately  $1g$ , resulting in a terminal velocity of the model of about 8 ft/sec.

The  $1g$  acceleration of the model was dictated by dynamic scaling laws which, for dynamic similarity, require accelerations which are inversely proportional to the model linear scale, assuming the same exhaust velocities of the model and the full-scale vehicle being simulated, and assuming that the frequency of the temperature oscillations in the near flow field scale with the Strouhal number as demonstrated in Reference 2. Thus, for the model investigated, the  $1g$  acceleration would correspond to realistic lift-off acceleration levels in the range of  $.1g - .2g$  for a full-scale vehicle, depending upon the vehicle size.

As a result of higher acceleration, the model time scale is compressed such that corresponding events in the full-scale vehicle being simulated occur at times greater than those for the model by the ratio of the inverse of the model linear scale. Thus, 1 second in the model linear scale would correspond to 5-10 seconds in the full scale, again depending upon the size of the vehicle being simulated.

For the landing tests, the model was accelerated rapidly to about 4 ft/sec from an initial height of  $H/D \approx 18$ . The 4 ft/sec velocity was then maintained until the model reached a height of  $H/D = 4$ , at which point vertical motion was terminated. For the landing tests, the exhaust pressure was maintained at the initial full power condition throughout.

The results of the dynamic simulation tests are presented in Figures 57 through 66.

### TAKEOFF

Figures 57, 58, and 59 show time histories of the inlet and inlet proximity thermal environment for two engine operation at turbojet exhaust conditions for low wind, 20 MPH headwind, and 20 MPH crosswind, respectively. At the low wind, a

significant increase in the thermal environment is seen to occur following release of the model vectoring doors ( $t = 0$ ), predominantly in the proximity of the aft inlet. Upon increasing the exhaust pressure level from the idle condition to the full power condition, the adverse thermal environment shifts toward the forward inlet. During the subsequent height transient, the thermal environment rapidly returns to pre-run ambient levels, becoming negligible at  $H/D \approx 14$ .

With the 20 MPH headwind (Figure 58), the thermal environment remains essentially ambient throughout the test (as for the equivalent steady-state wind tests discussed previously), with the exception of a few rather minor temperature pulses in the proximity of the inlets which have no significant effect on the spatial average inlet temperature,  $\bar{T}$ . In contrast, the 20 MPH crosswind produces an adverse thermal environment, resulting in significant ingestion of hot gases by the inlets which continue to persist at reduced (but significant) levels throughout and beyond the height transient which takes the model to  $H/D = 18$ .

Figure 60 shows equivalent data for turbofan exhaust conditions at low wind. The data are qualitatively similar to that of Figure 57 (turbojet exhaust conditions at low wind), but at reduced levels due to the cooler exhaust jet.

Figure 61 shows data for single jet operation with turbojet exhaust conditions at low wind. For these conditions, the thermal environment remains at essentially pre-run ambient temperature throughout the test.

## LANDING

Figures 62, 63, and 64 present time histories of the local thermal environment during landing with turbojet exhaust conditions at low wind, 20 MPH headwind, and 20 MPH crosswind, respectively. At low wind, the thermal environment is essentially ambient during the height transient down to  $H/D \approx 14$  at which point the inlet plane of the model enters the region of the upwash. The thermal environment continues to become more severe as the model drops lower, with the upwash predominately in the region of the forward inlet, until "touch-down" at  $H/D = 4$  is reached, beyond which steady state conditions prevail.

With the 20 MPH headwind (Figure 63), the thermal environment remains at essentially ambient conditions throughout the landing transient, with the exception of a few minor temperature pulses which occur after "touch-down." In contrast are the

data of Figure 64 for the 20 MPH crosswind which show a thermal environment above ambient at the initial height of  $H/D = 18$  which increases significantly below  $H/D \approx 8$ .

Figure 65 shows landing data for turbofan exhaust conditions at low wind. Again, as for takeoff, the data are qualitatively similar to the data for turbojet exhaust conditions, but at a reduced level due to the cooler exhaust jet.

Figure 66 shows data for single jet operation with turbojet exhaust conditions at low wind. As for "takeoff," the thermal environment remains at essentially prerun ambient temperature throughout the test.

## SUMMARY OF RESULTS

An investigation of the exhaust gas ingestion and recirculation flow field characteristics of a small-scale VTOL lift engine pod containing two simulated engines has been conducted. Results were obtained on the transient development of the recirculating flow field, steady state ingestion and recirculating flow field characteristics, and dynamic simulation of takeoff and landing. A summary of the principal results is given below.

### Flow Field Development

1. Development of the steady state recirculating flow field was found to occur within a few hundred milliseconds using either a trap door or exhaust vector door start-up technique. With the trap door start-up, the initial flow field develops in a non-symmetrical way due to superposition of the trap door motion on the spreading of the ground jet flow.

### Ingestion Characteristics

1. The inlet thermal environment was found to be highly sporadic, exhibiting closely spaced temperature spikes (up to about  $150^{\circ}\text{F}$  above ambient) which typically persisted for a small fraction of a second and encompassed anywhere from a small fraction of the inlet area to the majority of the inlet area. During time intervals between temperature spikes, the inlet thermal environment was typically ambient.

2. Correlation of the thermal environment along the sides of the pod (in the plane of the inlets) with the engine inlet thermal environment supports the concept of the upwash, or fountain, being the predominant source of ingestion.

3. Ingestion levels (as measured by cumulative time average indices indicative of inlet temperature level, temperature distortion, and temperature rate of rise) were found to be independent of time over the data acquisition period of 30 seconds.

### Ingestion Trends

1. Ingestion was found to increase significantly with nozzle spacing,  $S/D$ , over the range of  $S/D$  investigated ( $S/D = 4.90 - 9.80$ ). Ingestion was found to increase or decrease with model height above the ground plane,  $H/D$ , depending upon the values of  $H/D$  and  $S/D$ .

2. Ingestion was found to decrease significantly for headwinds greater than

about 10 MPH for turbojet exhaust conditions, becoming negligible at about 20 MPH. Ingestion was found to increase significantly with crosswinds, with ingestion for crosswinds of 30 MPH several times more severe than at low wind levels.

3. Ingestion was found to increase significantly with inlet Mach number, being several times more severe for an inlet Mach number of 0.5 than for an inlet Mach number of 0.1.

4. Ingestion was found to be independent of exhaust pressure over the range investigated ( $P_n/P_\infty = 1.4 - 1.9$ ), and independent of exhaust temperature, when non-dimensionalized with respect to exhaust minus ambient temperature ( $T_n - T_\infty$ ), over the range investigated ( $T_n = 440^\circ\text{F} - 1200^\circ\text{F}$ ).

#### Upwash Strength

1. Pressure distributions on the undersurface of the pod indicated strong upwash flows, with impingement velocities in excess of 200 ft/sec at low values of  $H/D$ . Upwash strength was found to rapidly decrease with  $H/D$ , and with  $S/D$  at low values of  $H/D$ . At higher values of  $H/D$ , however, upwash strength was found to increase with  $S/D$ .

2. Upwash strength was found to correlate with the path length between the nozzle exit and the pod undersurface at low values of  $H/D$ . At higher values of  $H/D$ , however, entrainment of the upwash by the free jets was found to become the dominant factor governing upwash strength, rather than path length.

3. Pod pressure distribution (i.e., upwash strength) was found to be independent of exhaust temperature over the range investigated ( $T_n = 440^\circ\text{F} - 1200^\circ\text{F}$ ), and independent of exhaust pressure, when non-dimensionalized with respect to exhaust minus ambient pressure ( $P_n - P_\infty$ ), over the range investigated ( $P_n/P_\infty = 1.4 - 1.9$ ).

4. Significant reduction in upwash strength was found to occur with headwinds, while crosswinds had a much less effect on upwash strength.

#### Dynamic Simulation

1. Simulated takeoff and landing tests, in which vertical motion of the model was programmed during the test, showed an instantaneous thermal environment qualitatively similar to that of the steady state tests, with ingestion becoming negligible at about the same value of  $H/D$  as for the steady state tests.

## REFERENCES

1. Hall, G. R., "Recirculation and Ingestion Characteristics of a Large-Scale VTOL Lift Engine Pod." NASA CR-72410, August 1968.
2. Hall, G. R., "Scaling of VTOL Recirculation Effects." NASA CR-1625, August 1970.
3. Lavi, R., "Parametric Investigations of VTOL Ground Proximity Effects." AIAA Paper Number 67-44, July 1967.
4. McLemore, H. C., Smith, C. C., Jr., "Hot-Gas Ingestion Investigation of Large-Scale Jet VTOL Fighter-Type Models." NASA TN-D-4609, June 1968.
5. Lavi, R., Hall, G. R., Stark, W. W., "Full-Scale Ground Proximity Investigation of a VTOL Fighter Model Aircraft." NASA CR-1098, June 1968.
6. Kirk, J. A., Barrack, J. P., "Reingestion Characteristics and Inlet Flow Distortion of V/STOL Lift Engine Fighter Configurations." AIAA Journal of Aircraft, March - April 1969.
7. McLemore, H. Clyde, Smith, C. C., Jr., and Hemeter, P. G., "Generalized Hot-Gas Ingestion Investigation of Large-Scale Jet VTOL Fighter-Type Models." NASA TN-D-5581, January 1970.
8. Watson, W. W., Weddell, A., Murakoshi, A., "Real Time, Real Temperature Jet V/STOL Test Facility." AIAA Paper Number 69-310, March 1969.
9. Hall, G. R., Bogdanovic, J. A., "Response of Bare Wire Thermocouples to Temperature Variations in a Jet Engine Intake." AIAA Journal of Aircraft, July - August 1967.
10. Hall, G. R., Rogers, K. H., "Recirculation Effects Produced by a Pair of Heated Jets Impinging on a Ground Plane." NASA CR-1307, May 1969.
11. Higgins, D. C., Kelly, D. P., Wainwright, T. W., "Exhaust Jet Wake and Thrust Characteristics of Several Nozzles Designed for VTOL Downwash Suppression." NASA CR-373, January 1966.

TABLE 1. TEST CONDITIONS

(A) Start-Up Tests

No. Engines	H/D	S/D	Exhaust Condition	Wind Condition	Start-Up Mode
2	4	7.35	Turbojet	<3 MPH	Full exh. press. → Trap door closure Full exh. press. → Vector door release Idle exh. press. → Trap door closure → Full exh. press. Idle exh. press. → Vector door release → Full exh. press.

Note: (1) Each start-up mode run 3 times for repeatability evaluation.

(2) Exhaust pressure transient from idle to full pressure indicated below:

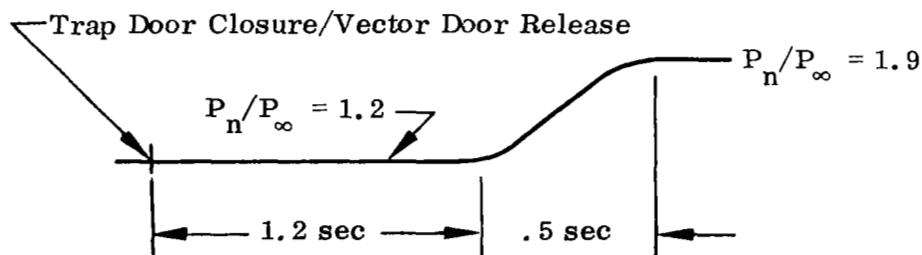


TABLE 1 (cont'd). TEST CONDITIONS

## (B) Steady-State Tests

No. Engines	H/D	S/D	Exhaust Condition	Wind Condition	
				Speed	Direction
2 ↓	2 4 6 8	4.90 ↓	Turbojet ↓	<3 MPH ↓	--- ↓
2 ↓	2 4* 6 8 12	7.35 ↓	Turbojet ↓	<3 MPH ↓	--- ↓
2 ↓	2 4 6 8	9.8 ↓	Turbojet ↓	<3 MPH ↓	--- ↓
2 ↓	4 ↓	7.35 ↓	Turbojet ↓	5 MPH 10 20 30	Headwind ↓
2 ↓	4 ↓	7.35 ↓	Turbojet ↓	10 MPH 20 30	Crosswind ↓
2 ↓	2 6 8 12	7.35 ↓	Turbojet ↓	20 MPH ↓	Headwind ↓
2 ↓	2 6 8 12	7.35 ↓	Turbojet ↓	20 MPH ↓	Crosswind ↓
1 ↓	4 ↓	7.35 ↓	Turbojet ↓	<3 MPH 5 10 20 30	--- Headwind ↓
2 ↓	2 4 6 8 12	7.35 ↓	Turbofan ↓	<3 MPH ↓	--- ↓
2 ↓	4 ↓	7.35 ↓	Turbofan ↓	10 MPH 20 30	Headwind ↓
2 ↓	4 ↓	7.35 ↓	Turbofan ↓	10 MPH 20 30	Crosswind ↓

\*Effect of inlet Mach number variation from the nominal value of 0.5 was also investigated at this test condition.

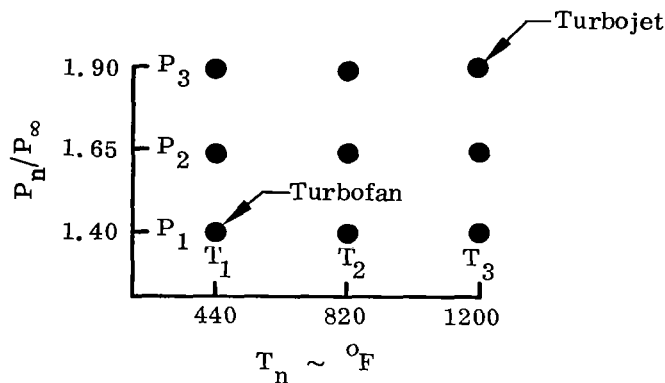


TABLE 1 (cont'd). TEST CONDITIONS

(B) Steady-State Tests (cont'd)

No. Engines	H/D	S/D	Exhaust Condition	Wind Condition	
				Speed	Direction
1 ↓	4 ↓	7.35 ↓	Turbofan ↓	<3 MPH 10 20 30	Headwind ↓
2 ↓	4 ↓	7.35 ↓	P <sub>2</sub> /T <sub>1</sub> P <sub>3</sub> /T <sub>1</sub> P <sub>1</sub> /T <sub>2</sub> P <sub>2</sub> /T <sub>2</sub> P <sub>3</sub> /T <sub>2</sub> P <sub>1</sub> /T <sub>3</sub> P <sub>2</sub> /T <sub>3</sub>	<3 MPH ↓	--- ↓

Note: (1) Trap door start-up.  
(2) Exhaust pressure/temperature matrix indicated below:



(C) Dynamic Simulation Tests

No. Engine	H/D	S/D	Exhaust Condition	Wind Condition		Model Motion		
				Speed	Direction	Mode	Model Acceleration	Model Terminal Velocity
2 ↓	Variable ↓	7.35 ↓	Turbojet ↓	<3 MPH	---	Takeoff	1.0 g	8 fps
1 ↓	↓	↓	Turbofan ↓	20 MPH	Headwind	↓	↓	↓
1 ↓	↓	↓	Turbojet ↓	20 MPH	Crosswind	↓	↓	↓
2 ↓	Variable ↓	7.35 ↓	Turbojet ↓	<3 MPH	---	Landing	-1.5 g	4 fps
1 ↓	↓	↓	Turbofan ↓	20 MPH	Headwind	↓	↓	↓
1 ↓	↓	↓	Turbojet ↓	20 MPH	Crosswind	↓	↓	↓
1 ↓	↓	↓	Turbofan ↓	<3 MPH	---	↓	↓	↓
1 ↓	↓	↓	Turbojet ↓	<3 MPH	---	↓	↓	↓

Note: Vector door start-up for takeoff tests.

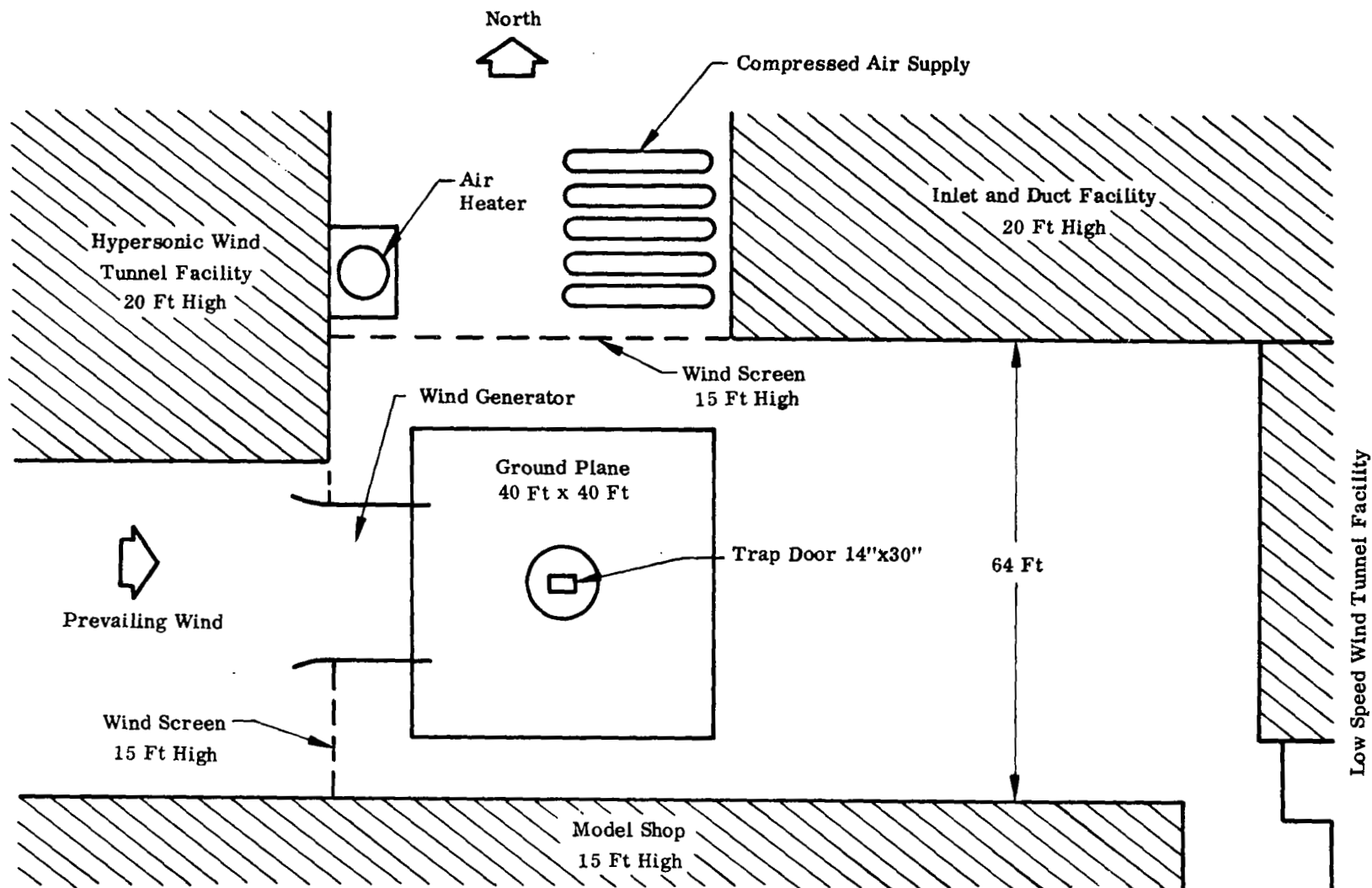


FIGURE 1. NORTHROP V/STOL GROUND EFFECTS TEST FACILITY

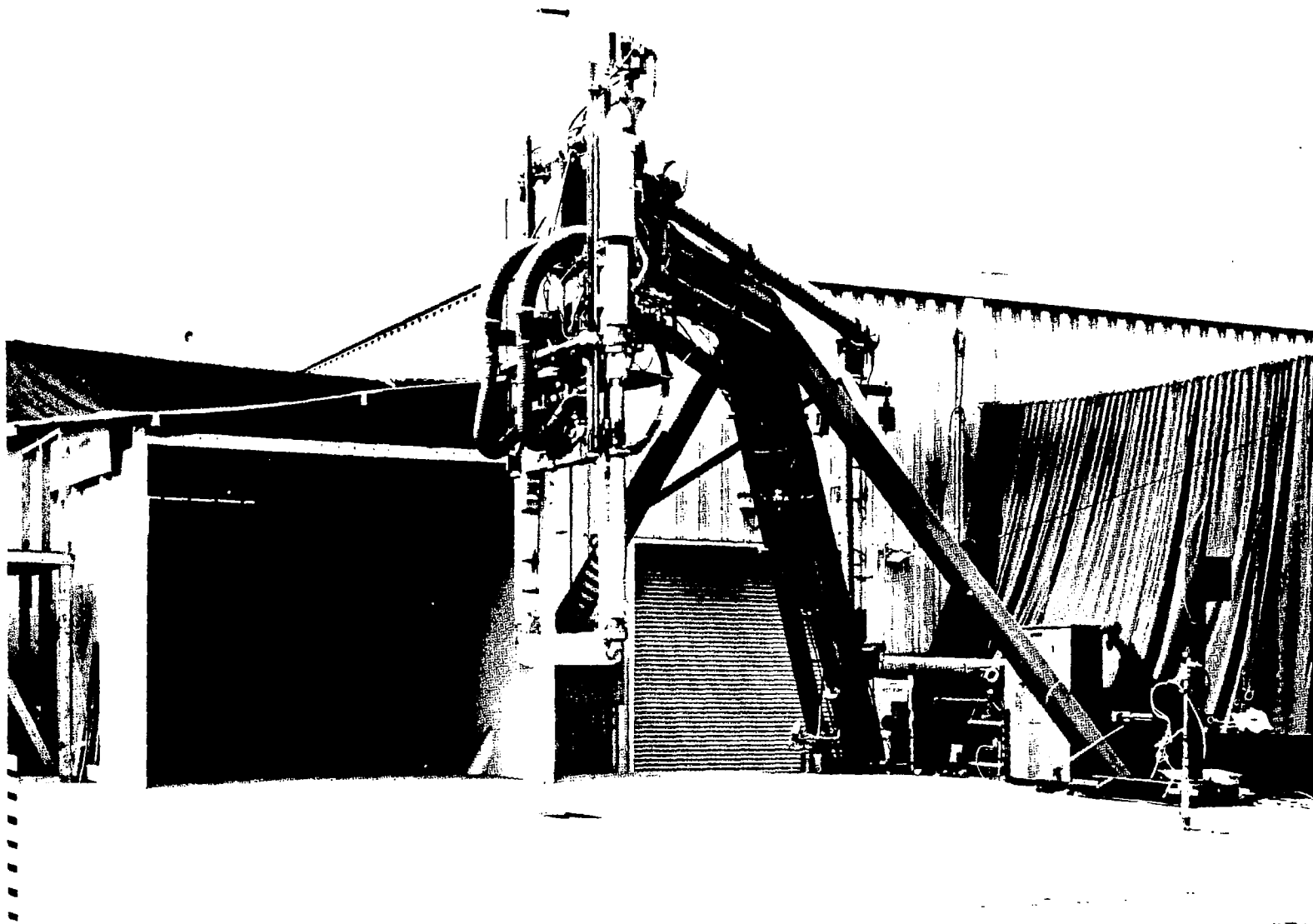


FIGURE 2. NORTHROP V/STOL GROUND EFFECTS TEST FACILITY

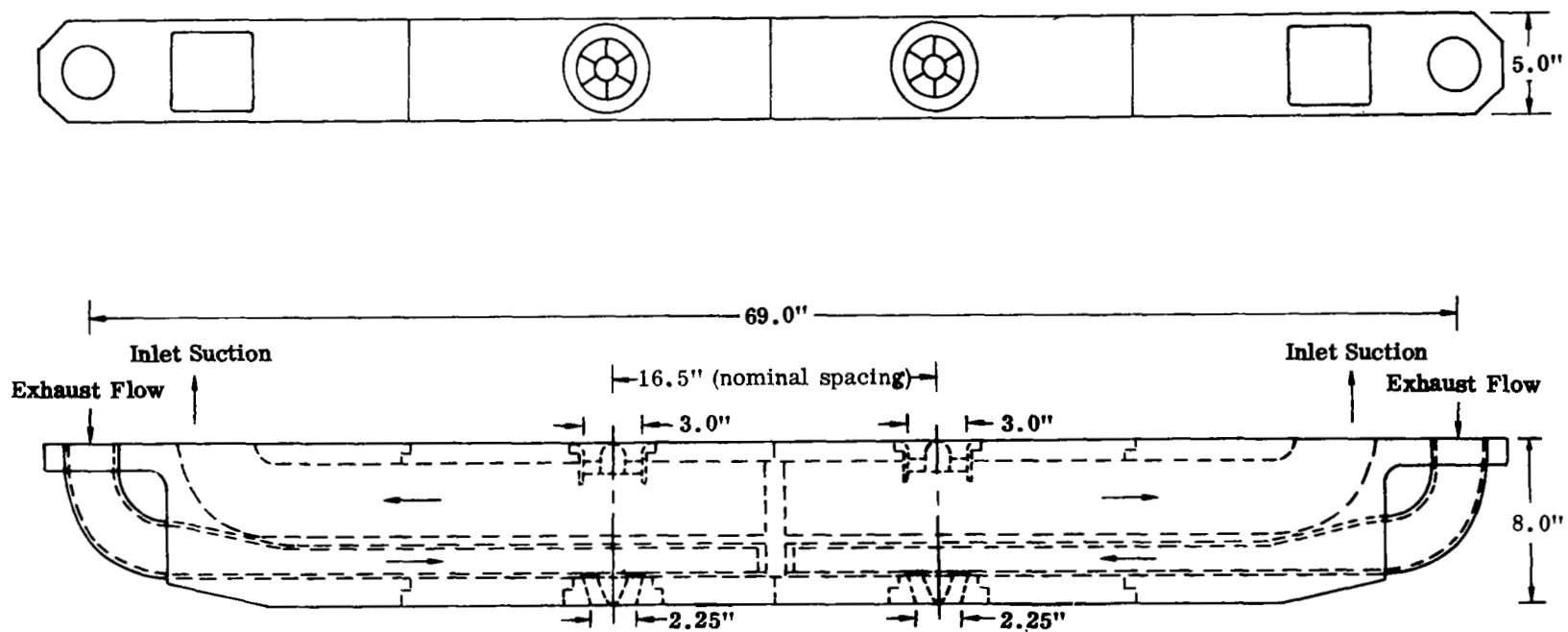


FIGURE 3. ENGINE POD MODEL

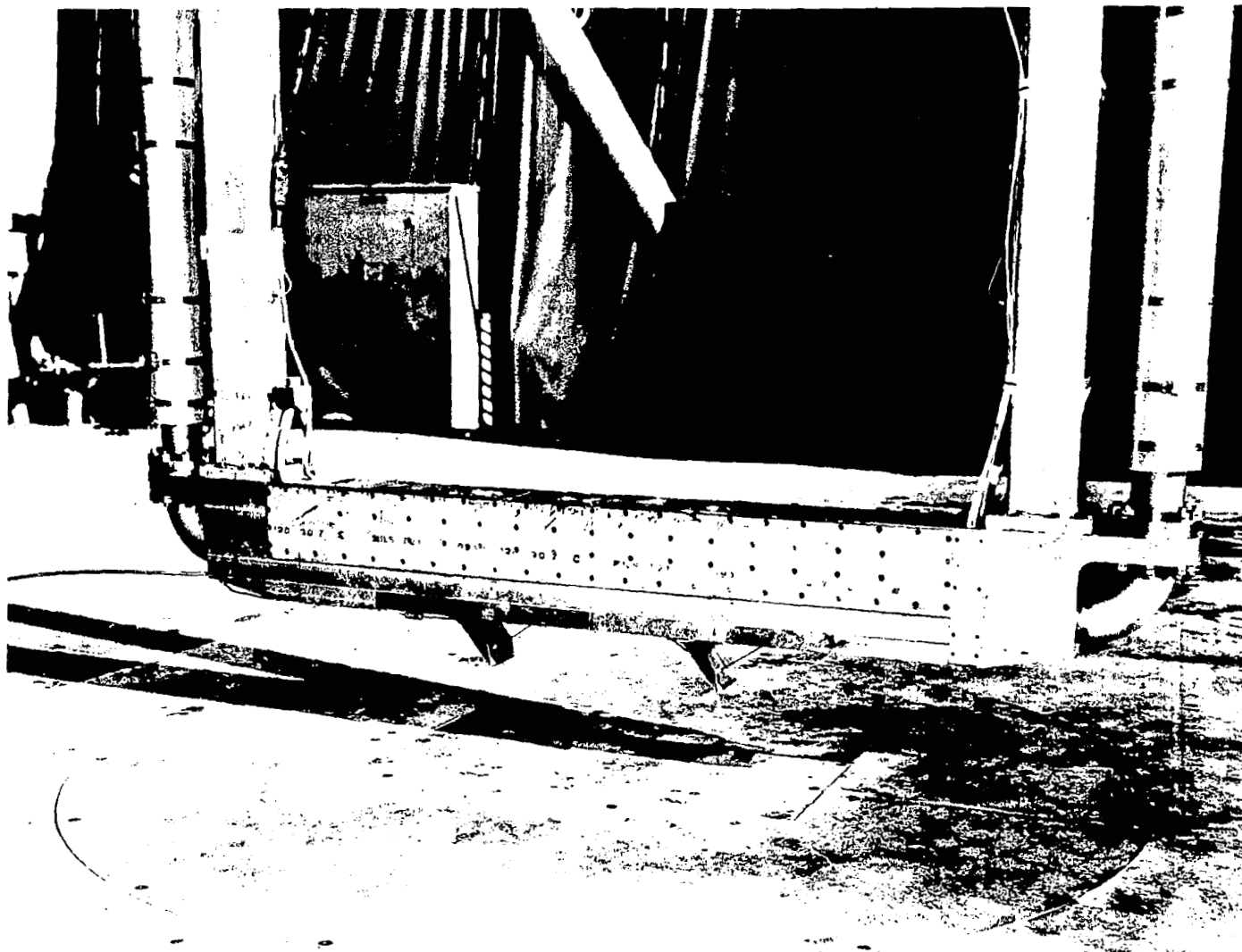


FIGURE 4. ENGINE POD MODEL

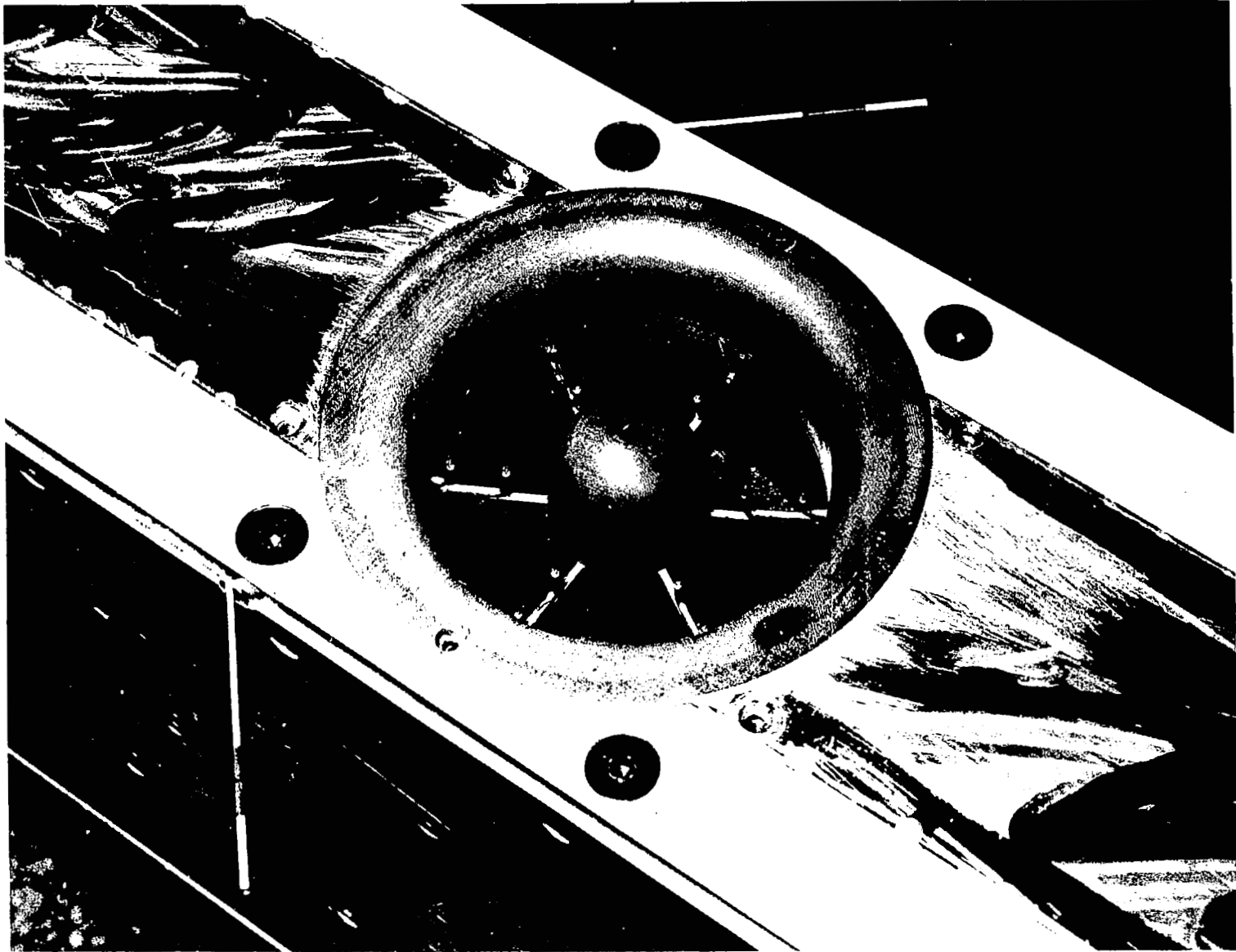


FIGURE 5. INLET DETAIL

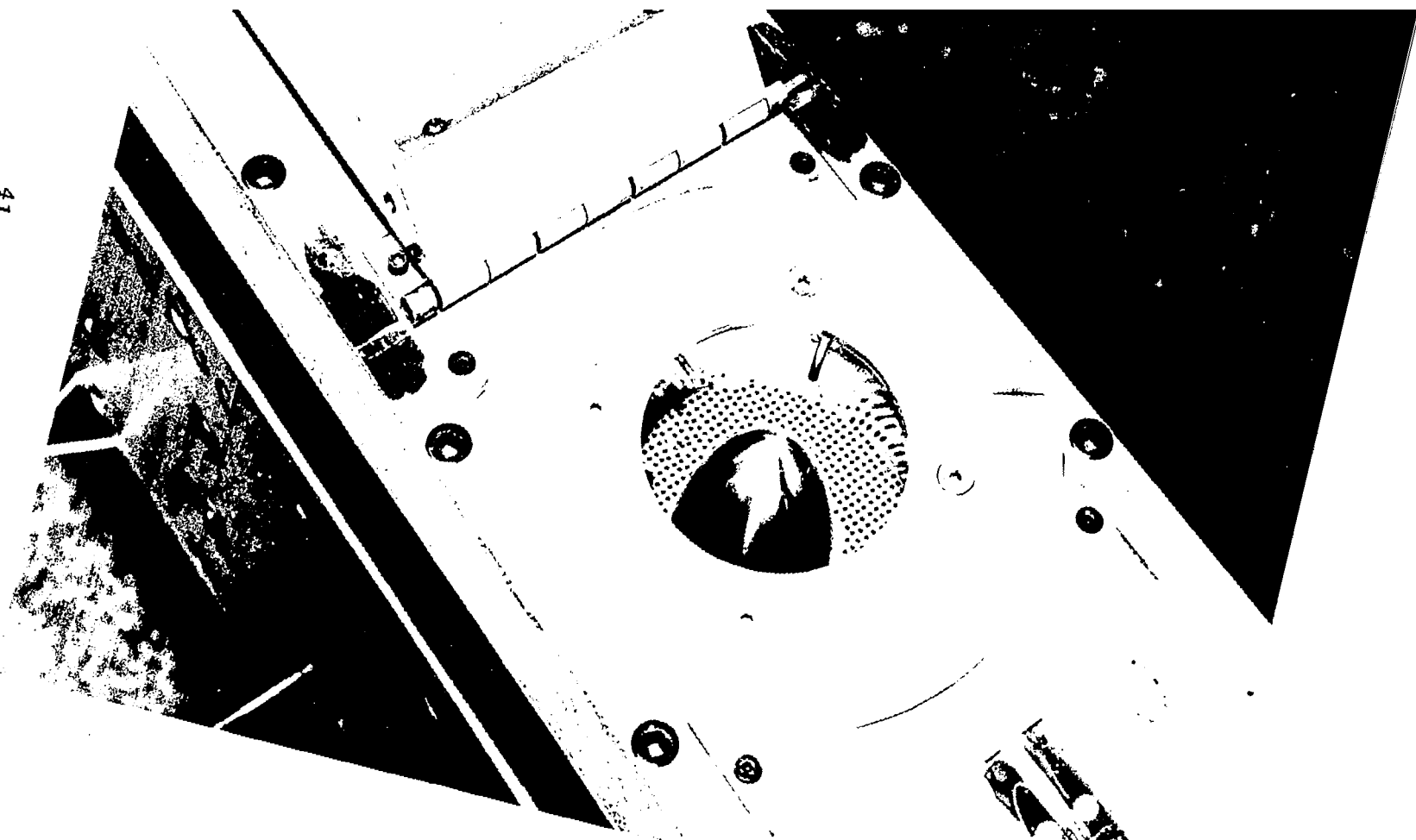


FIGURE 6. EXHAUST NOZZLE DETAIL

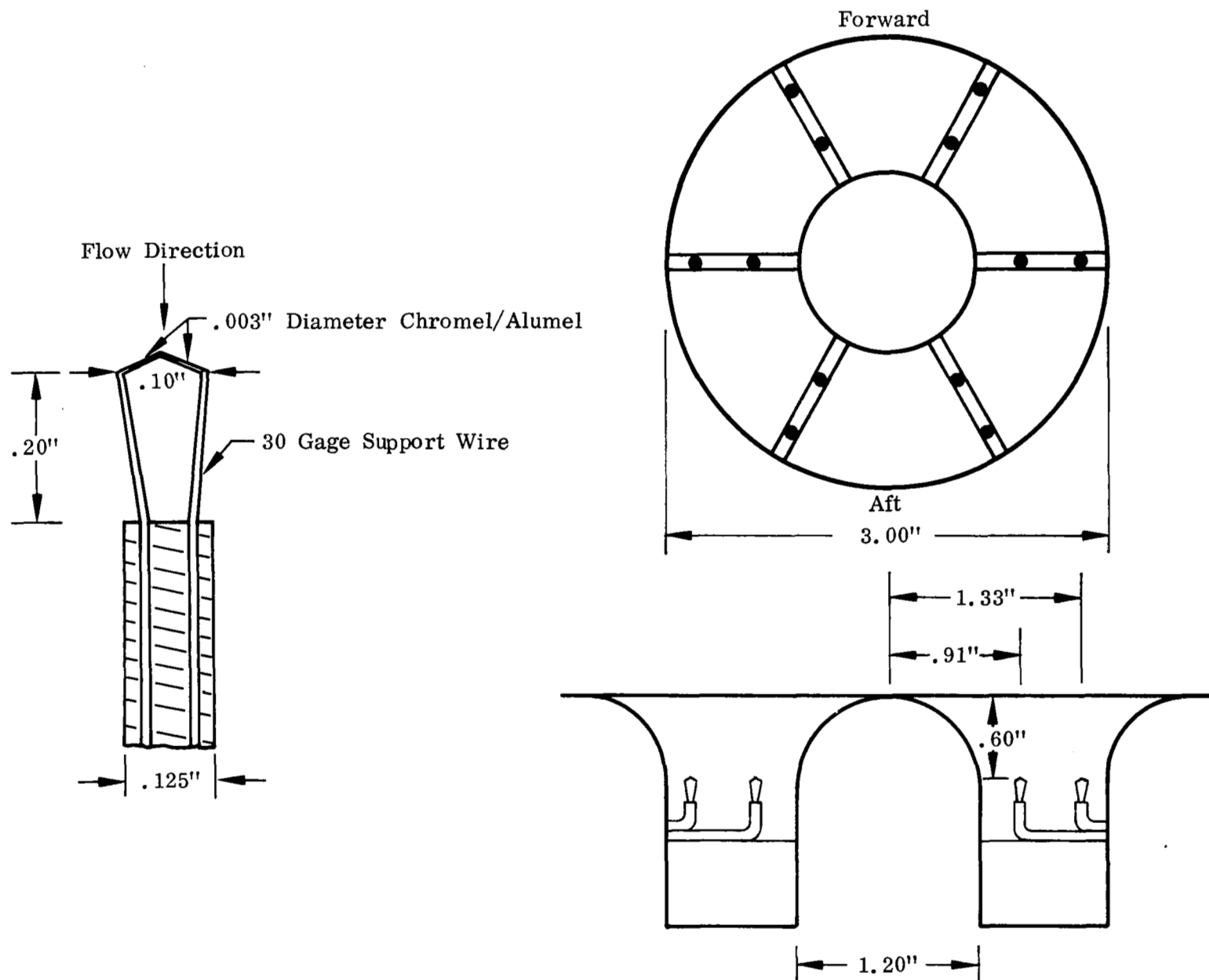
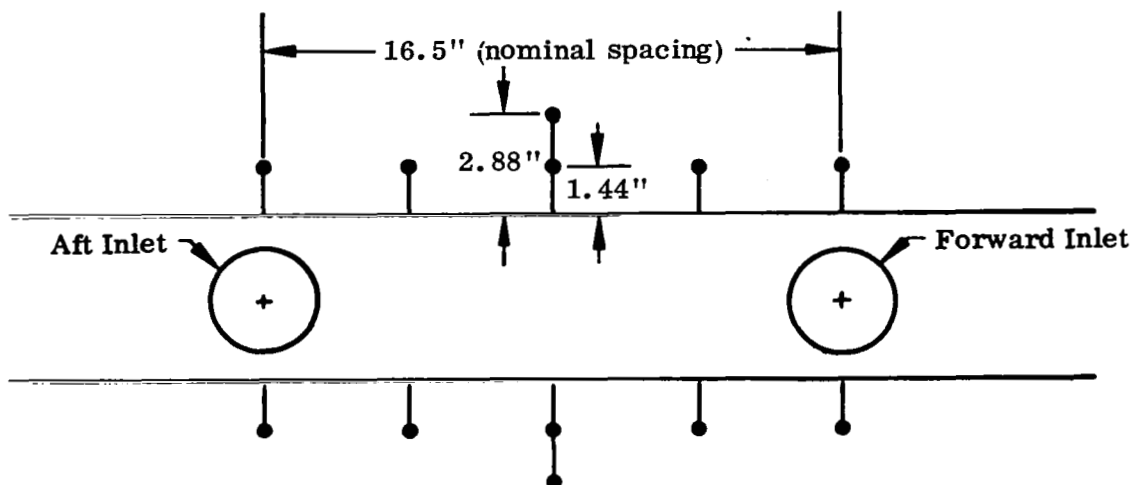


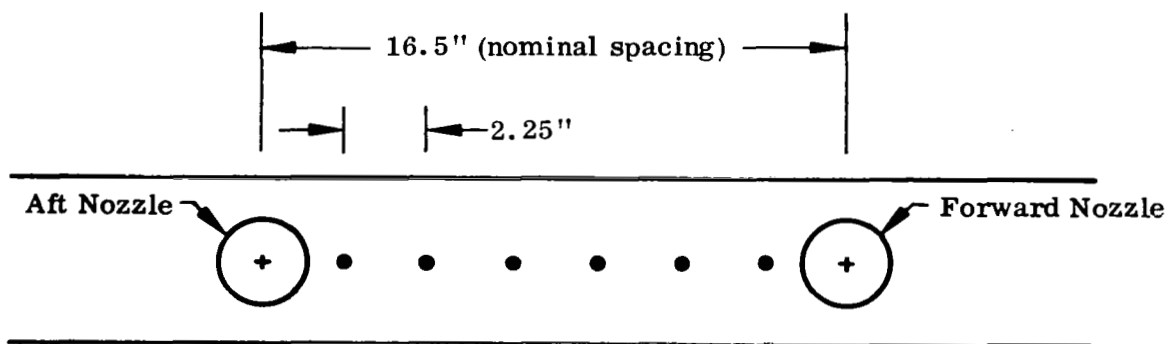
FIGURE 7. INLET THERMOCOUPLE INSTRUMENTATION





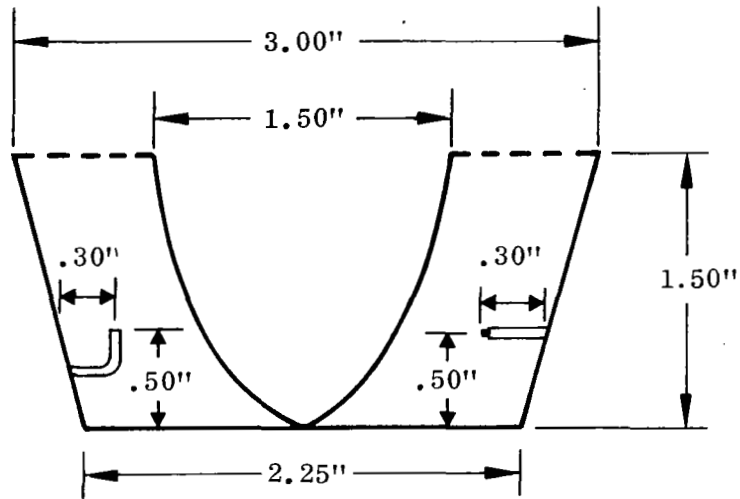
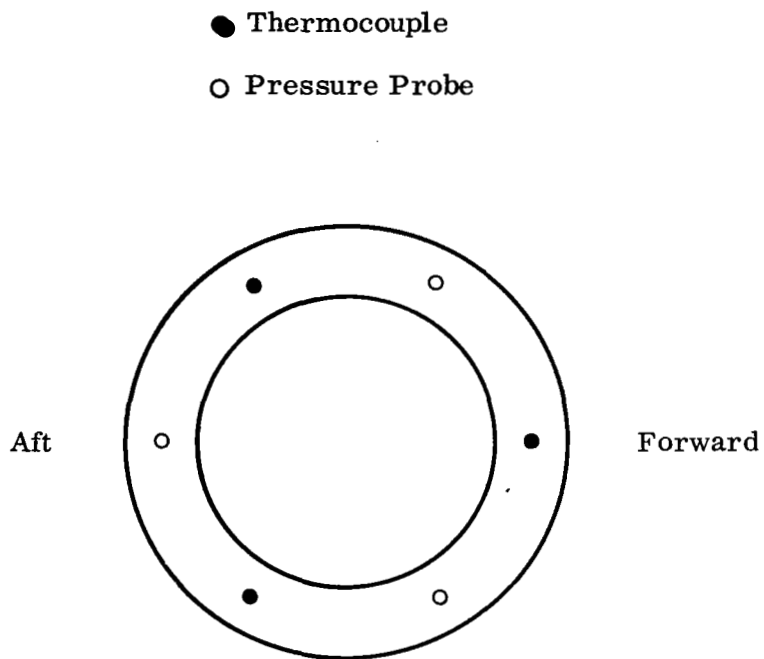
Note: T-C's located in plane of the inlets

FIGURE 8. INLET PROXIMITY THERMOCOUPLES



Note: Pressure taps located on pod lower surface

FIGURE 9. POD PRESSURE INSTRUMENTATION



Note: Thermocouples/pressure probes ganged together to provide single temperature/pressure readout.

FIGURE 10. EXHAUST NOZZLE INSTRUMENTATION

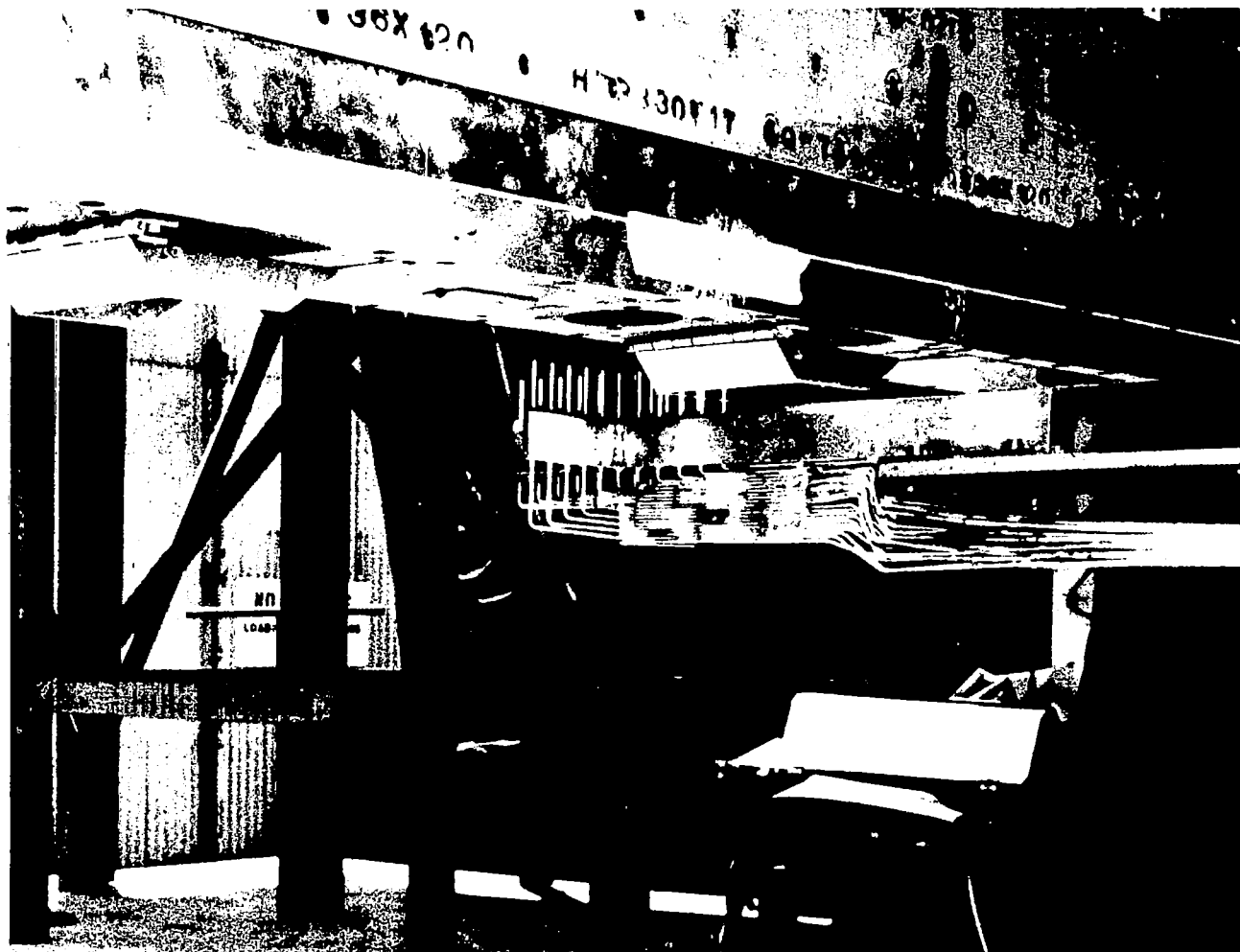
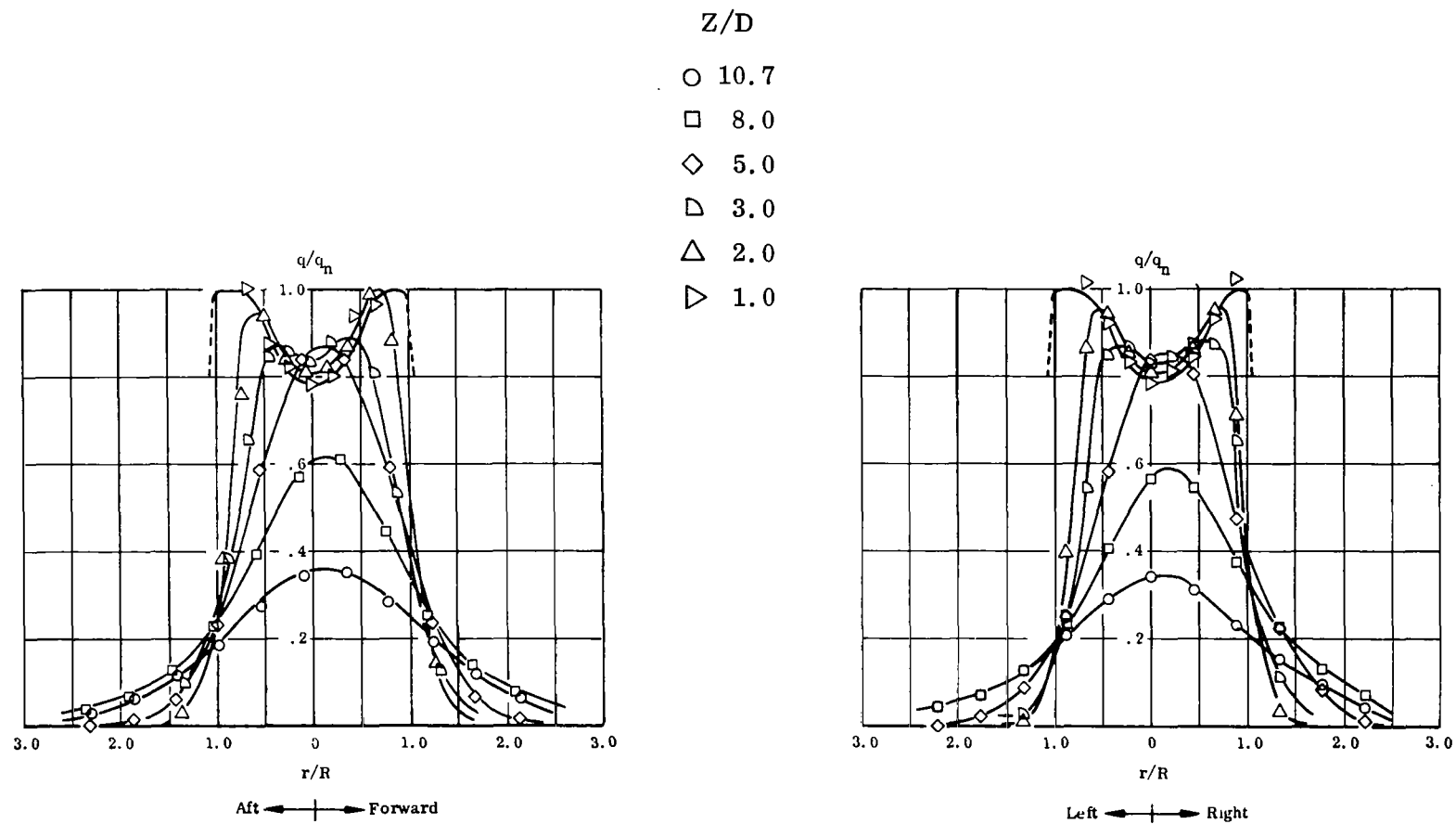
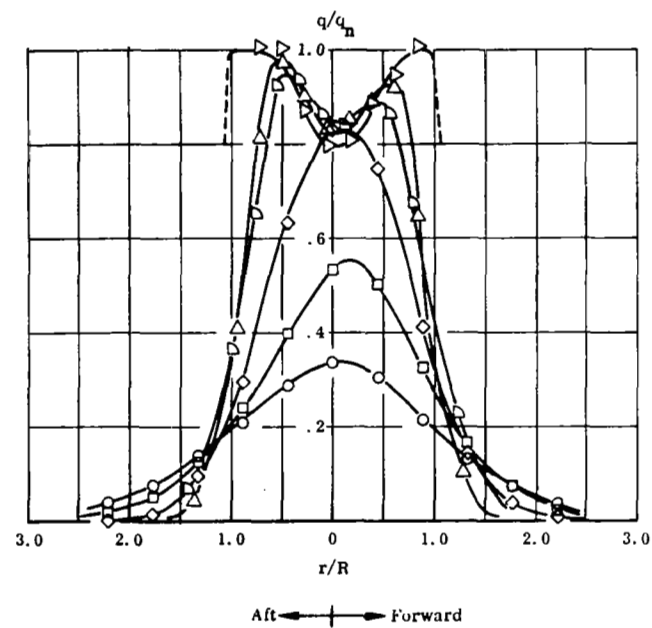
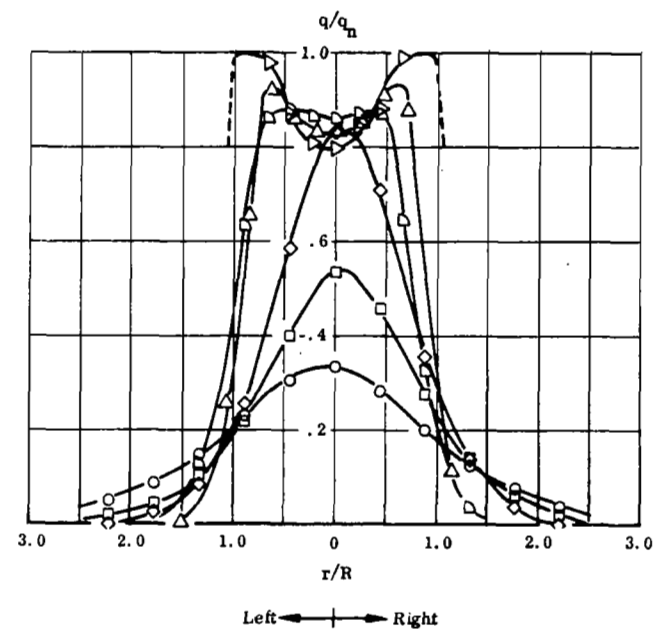


FIGURE 11. EXHAUST JET CALIBRATION RAKE



(a) FORWARD NOZZLE

FIGURE 12. EXHAUST JET CALIBRATION - TURBOJET

 $Z/D$  $\circ$  10.7 $\square$  8.0 $\diamond$  5.0 $\triangleright$  3.0 $\triangle$  2.0 $\triangleright$  1.0

(b) AFT NOZZLE

FIGURE 12 (cont'd). EXHAUST JET CALIBRATION - TURBOJET

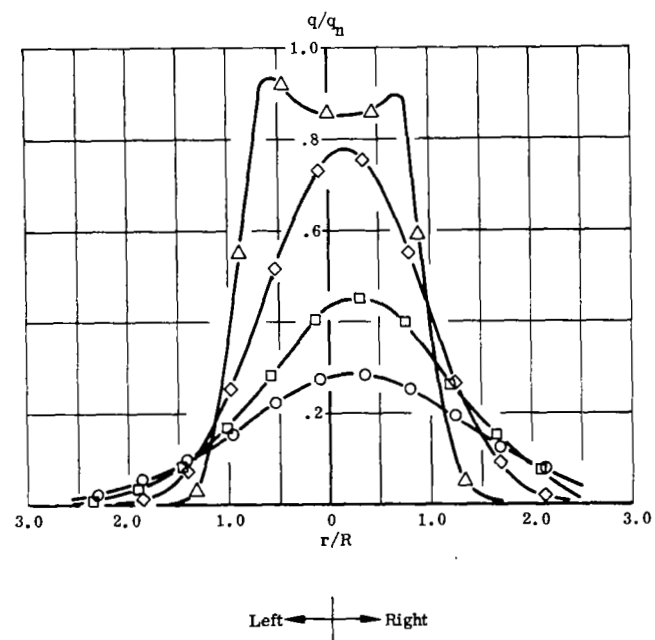
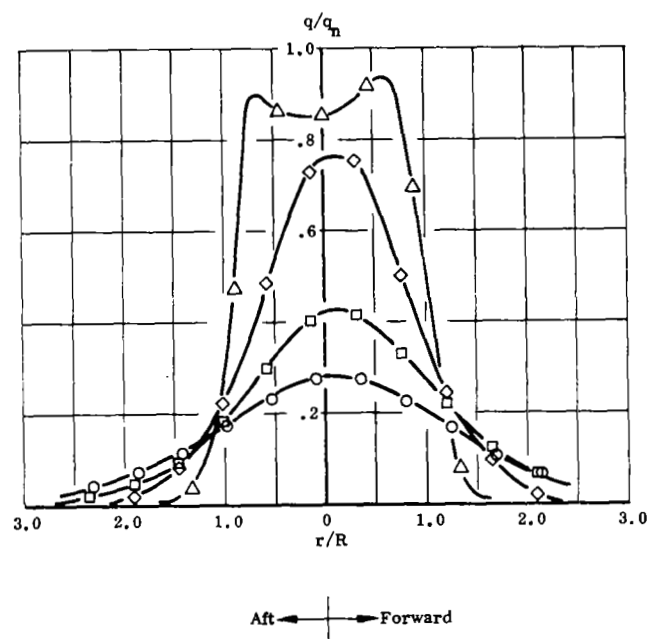
$Z/D$

○ 10.7

□ 8.0

◇ 5.0

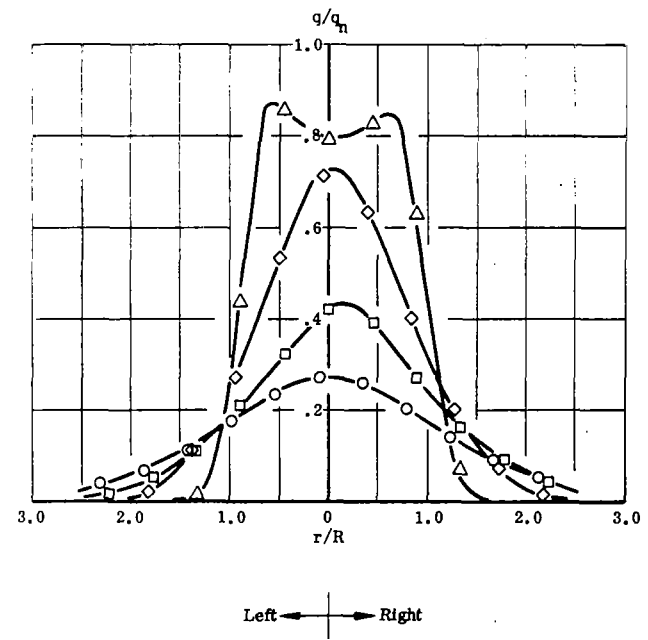
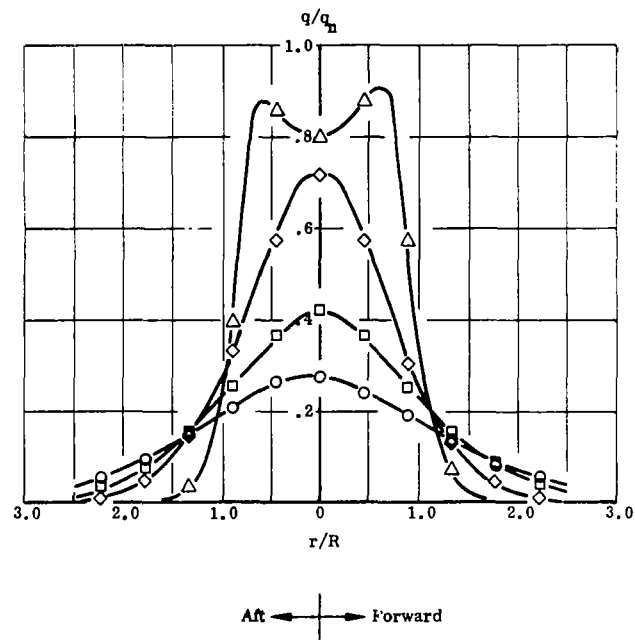
△ 2.0



(a) FORWARD NOZZLE

FIGURE 13. EXHAUST JET CALIBRATION - TURBOFAN

$Z/D$   
 ○ 10.7  
 □ 8.0  
 ◇ 5.0  
 △ 2.0



(b) AFT NOZZLE

FIGURE 13 (cont'd). EXHAUST JET CALIBRATION - TURBOFAN

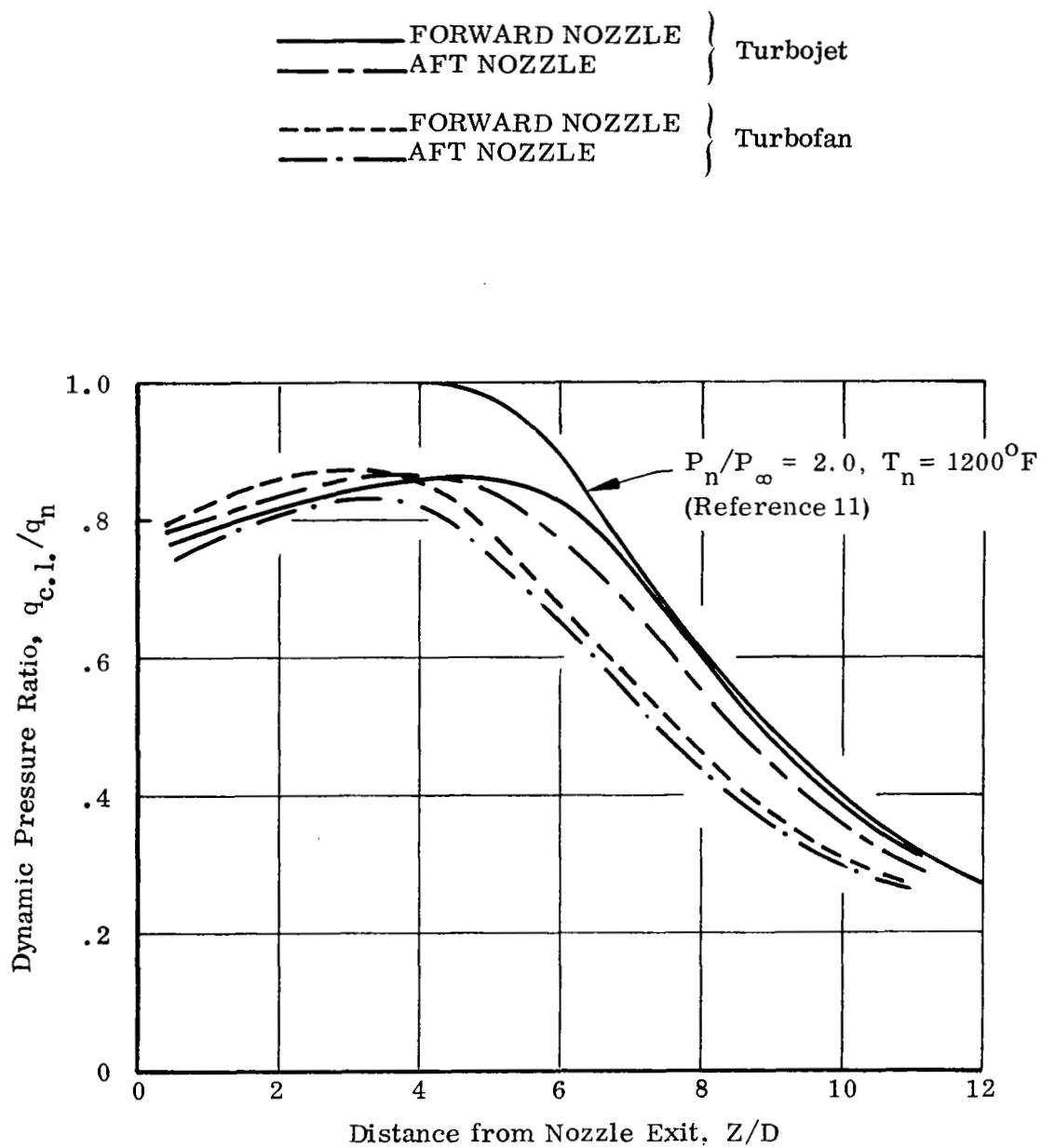


FIGURE 14. EXHAUST JET CENTERLINE DYNAMIC PRESSURE DECAY



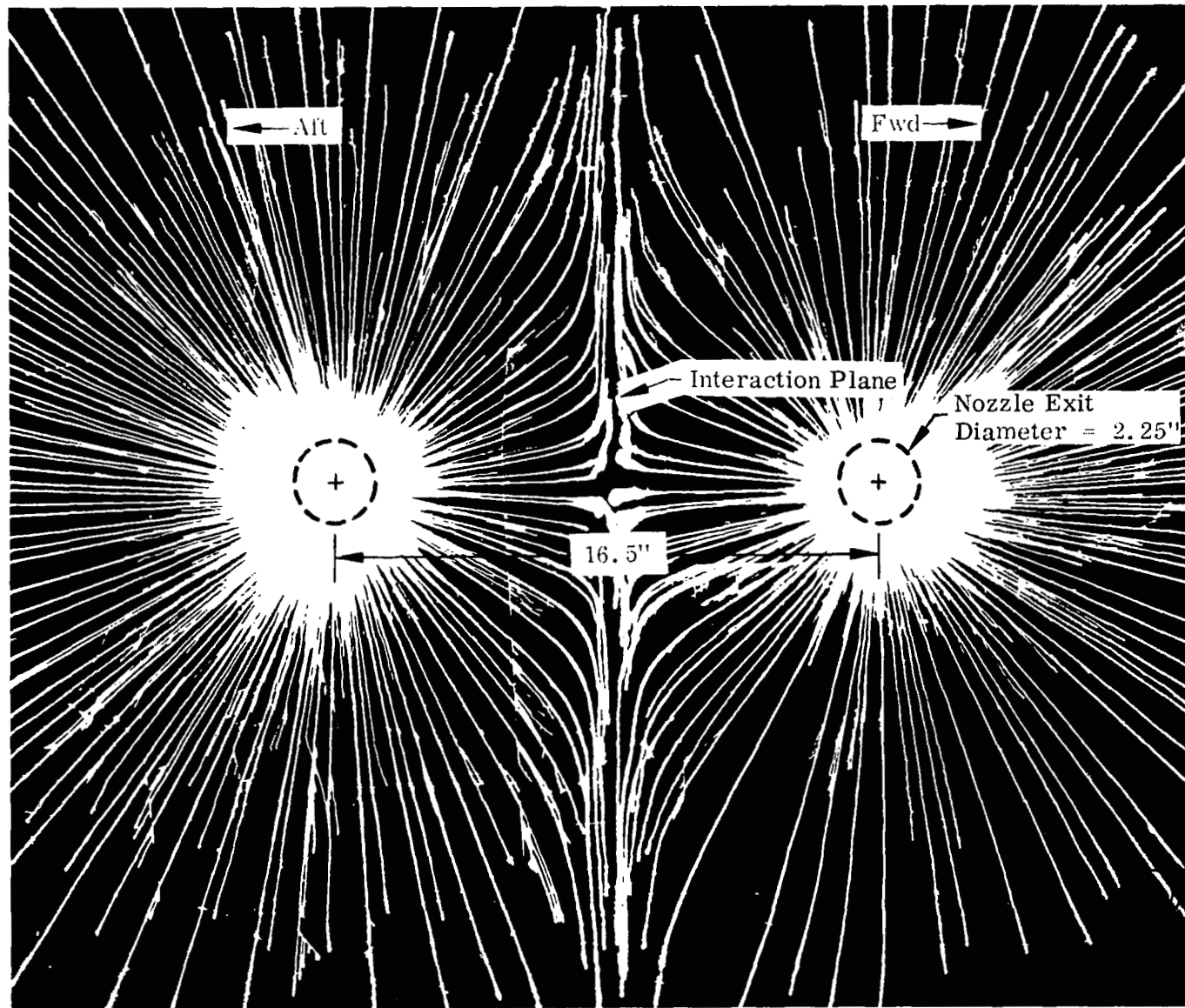


FIGURE 15. GROUND PLANE OIL STREAK PATTERN

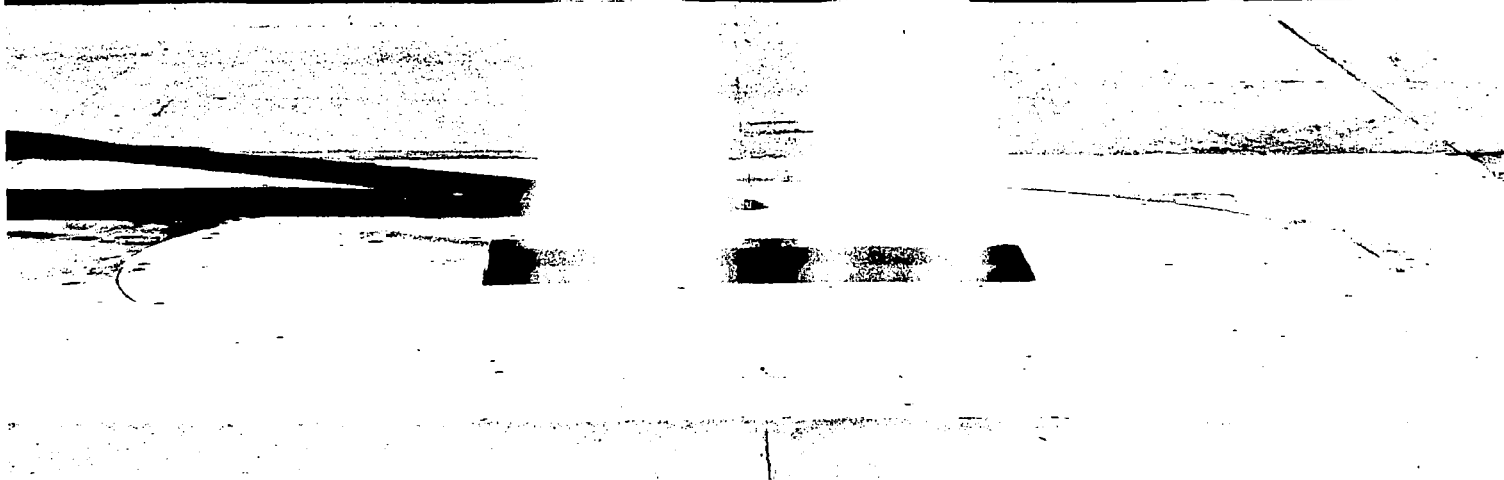
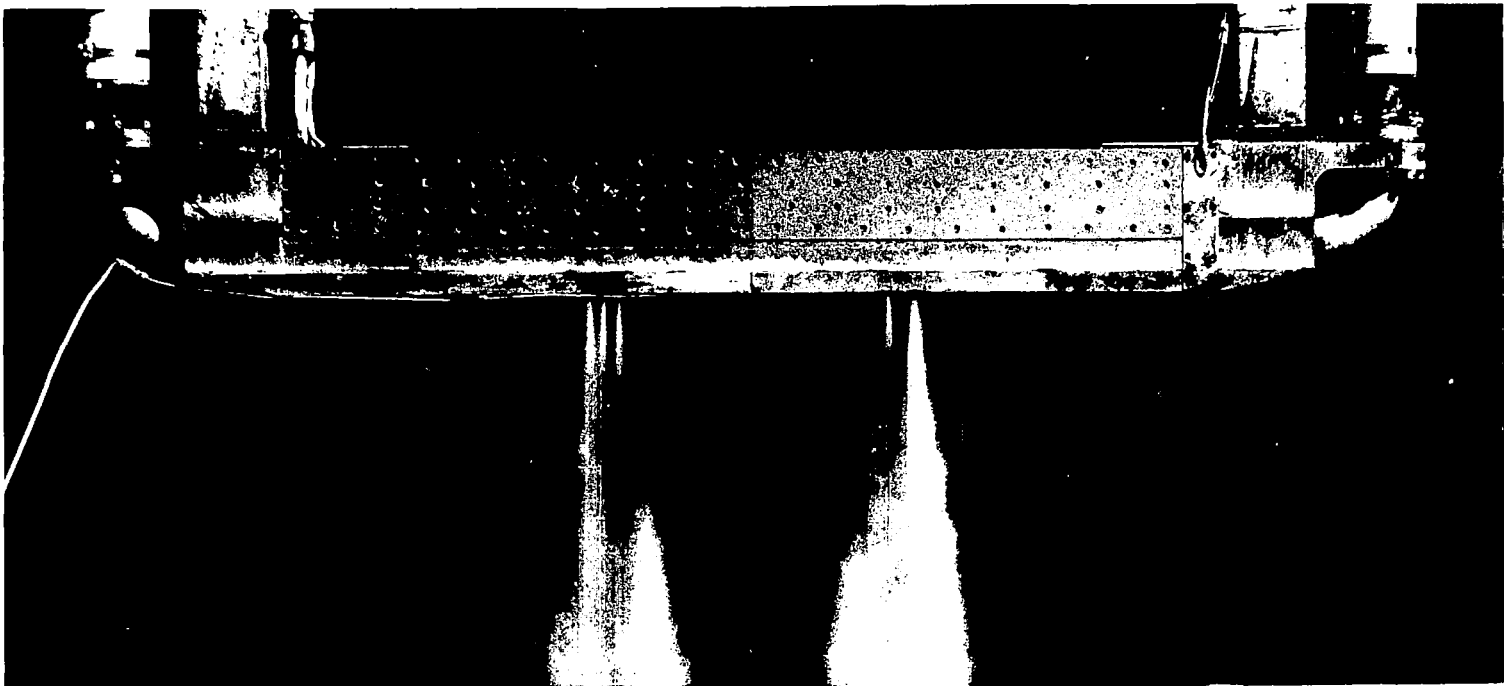


FIGURE 16. EXHAUST JET FLOW VISUALIZATION

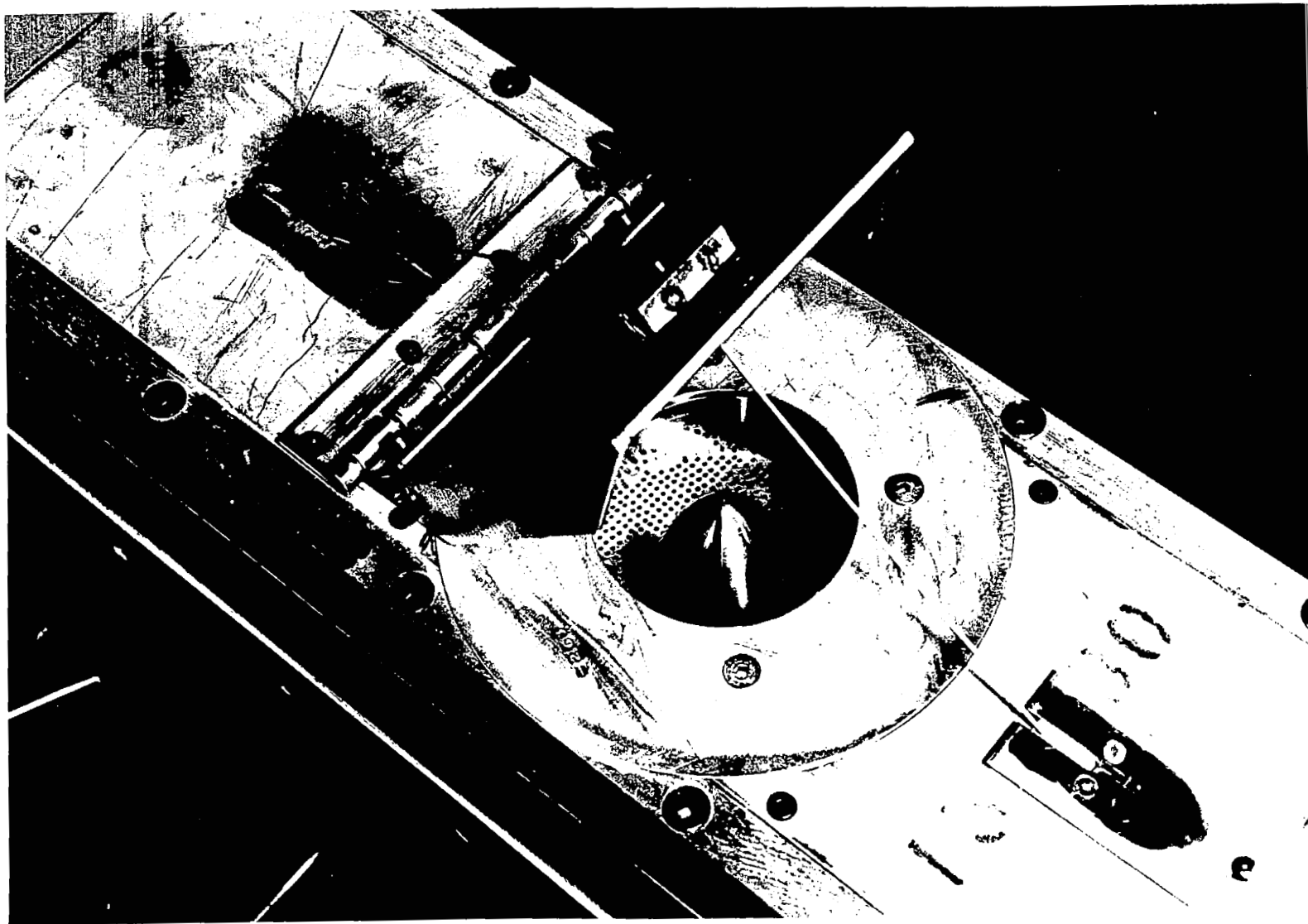
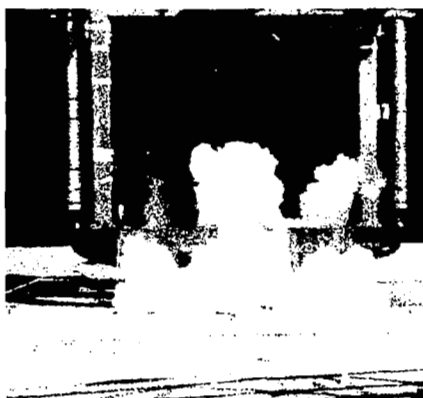


FIGURE 17. EXHAUST VECTOR DOOR

Two Engine Operation  
Turbojet  
 $H/D = 4$   
 $S/D = 7.35$



$t = .08$  seconds



$t = .10$  seconds



$t = .12$  seconds



$t = .16$  seconds



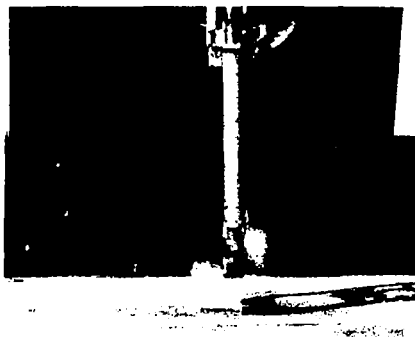
$t = .20$  seconds



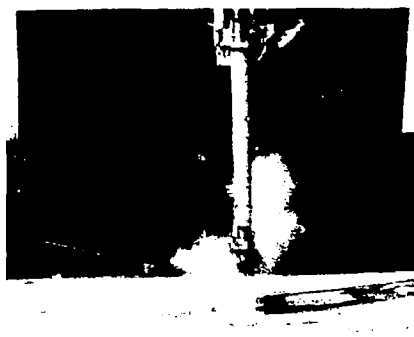
$t = .30$  seconds

FIGURE 18. FLOW FIELD DEVELOPMENT WITH TRAP DOOR  
START-UP - PROFILE VIEW

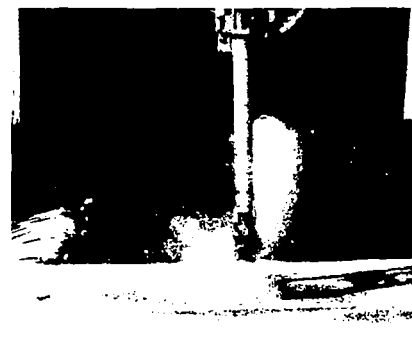
Two Engine Operation  
Turbojet  
 $H/D = 4$   
 $S/D = 7.35$



$t = .08$  seconds



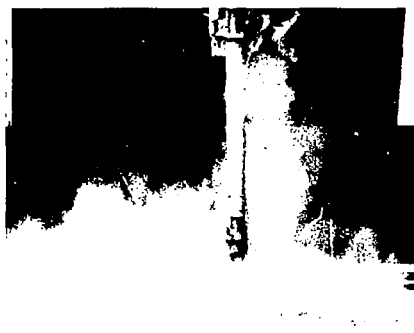
$t = .10$  seconds



$t = .12$  seconds



$t = .16$  seconds



$t = .20$  seconds



$t = .30$  seconds

FIGURE 19. FLOW FIELD DEVELOPMENT WITH TRAP DOOR  
START-UP - END VIEW

Two Engine Operation  
Turbojet  
H/D = 4, S/D = 7.35  
Wind < 3 MPH

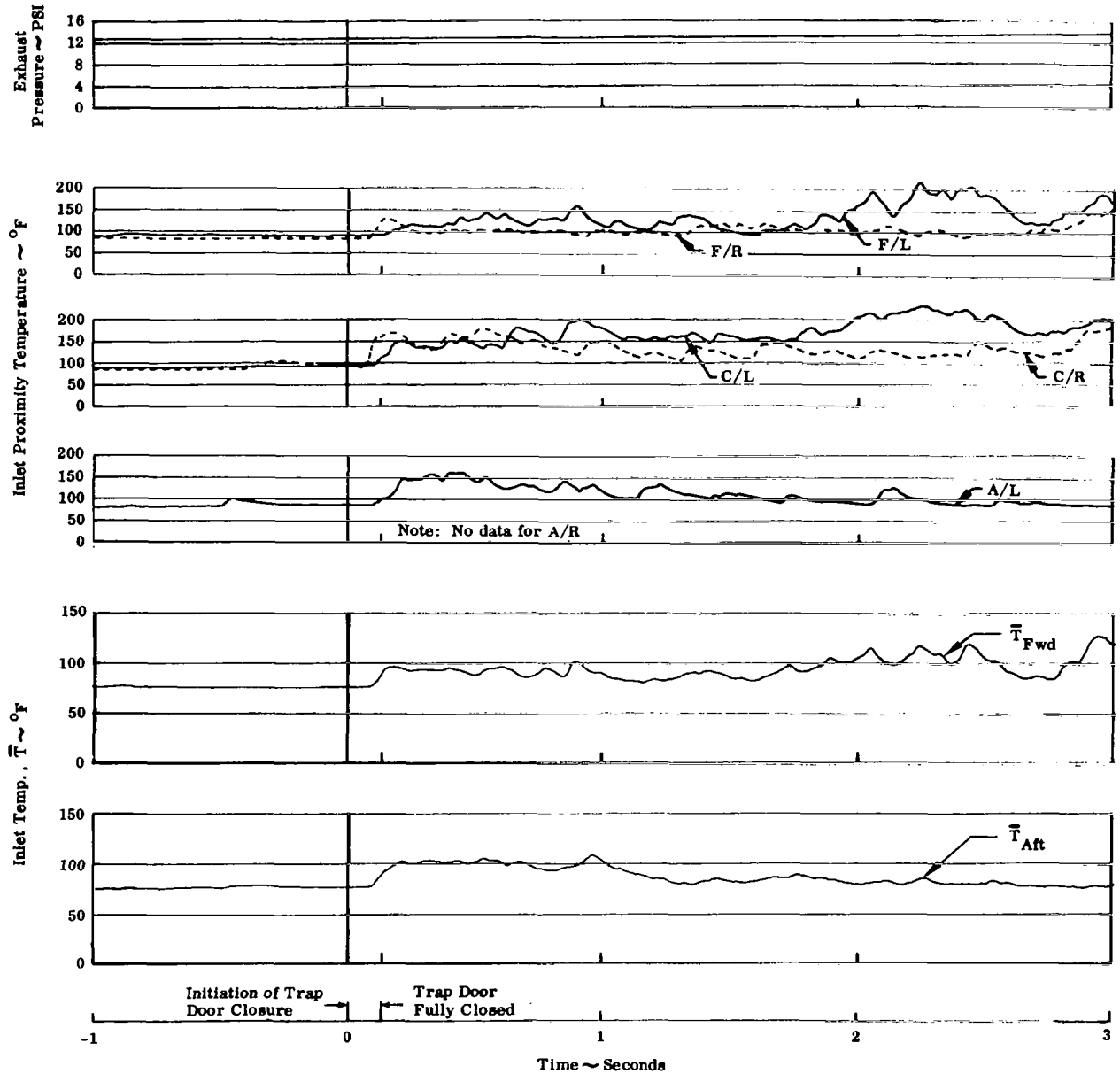
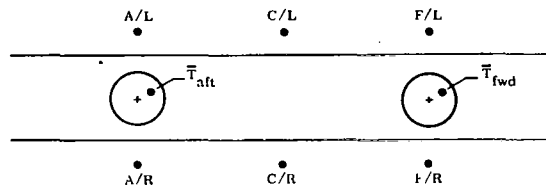


FIGURE 20. START-UP TRANSIENT - TRAP DOOR WITH CONSTANT EXHAUST PRESSURE

Two Engine Operation  
Turbojet  
H/D = 4, S/D = 7.35  
Wind < 3 MPH

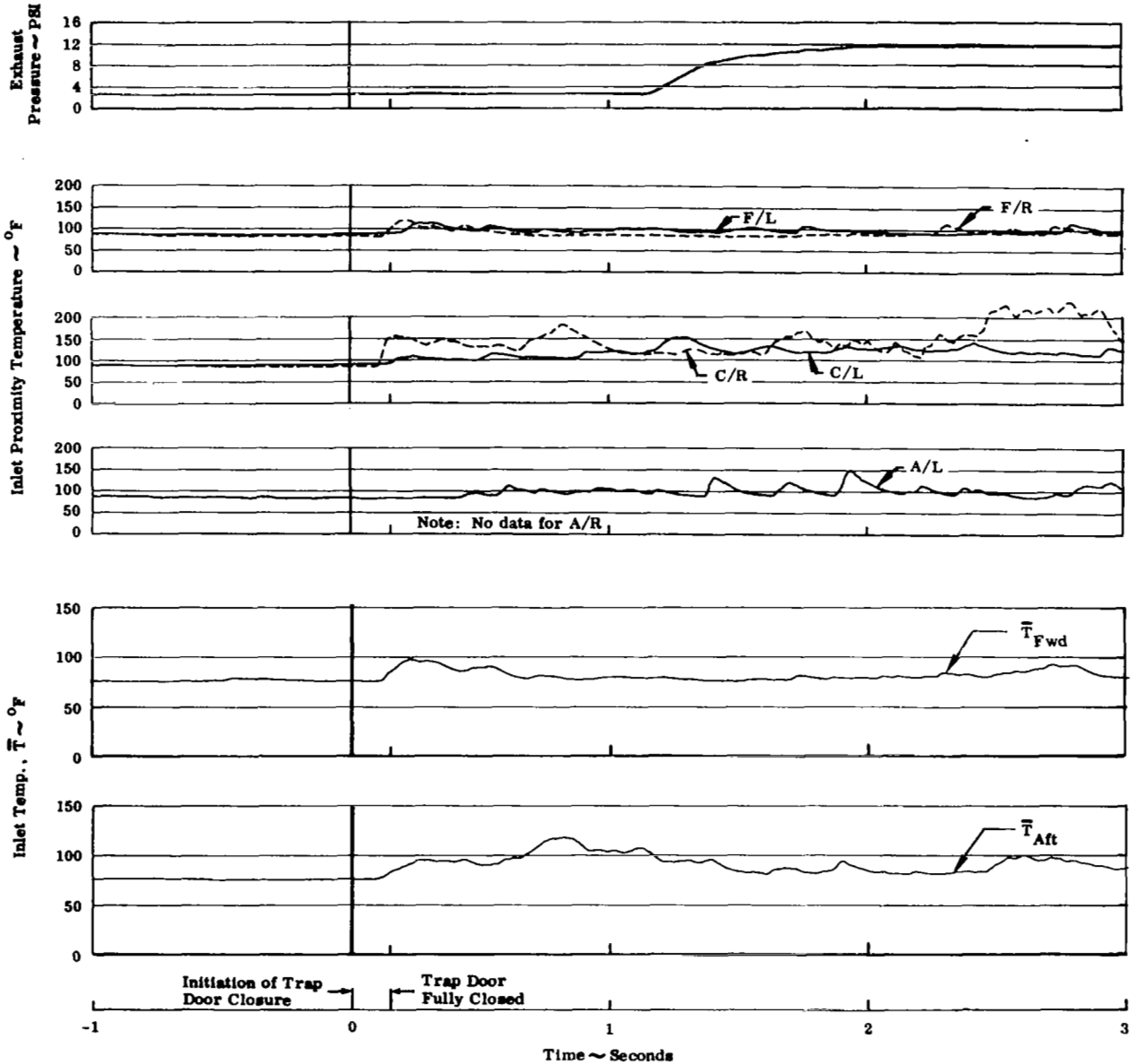
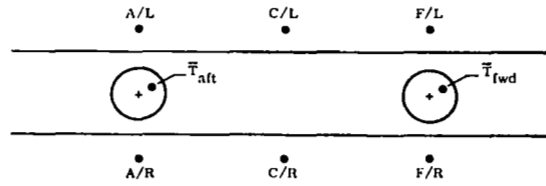


FIGURE 21. START-UP TRANSIENT - TRAP DOOR WITH VARIABLE EXHAUST PRESSURE

Two Engine Operation  
Turbojet  
H/D = 4, S/D = 7.35  
Wind < 3 MPH

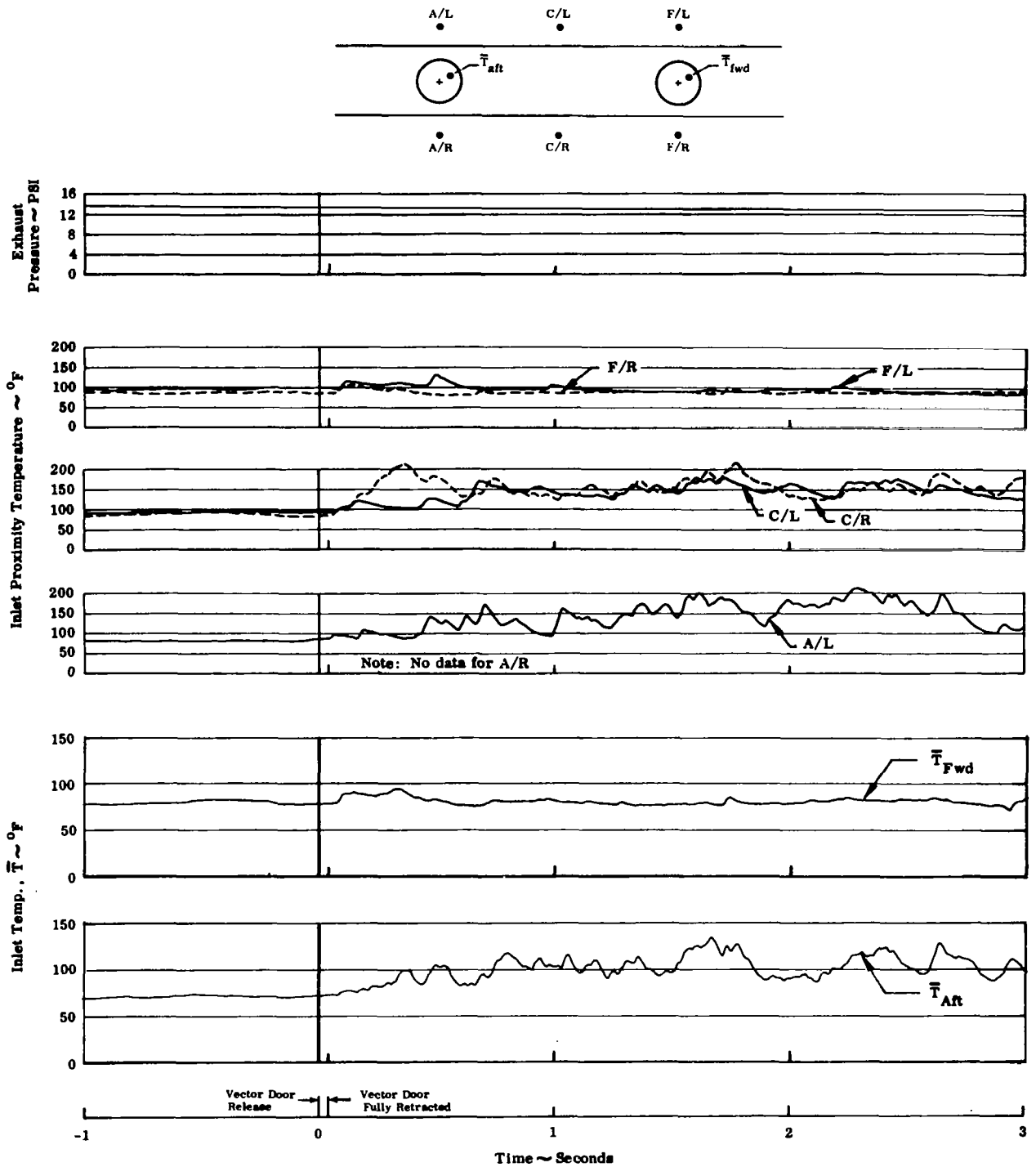


FIGURE 22. START-UP TRANSIENT - VECTOR DOOR WITH CONSTANT EXHAUST PRESSURE



Two Engine Operation  
Turbojet  
H/D = 4, S/D = 7.35  
Wind < 3 MPH

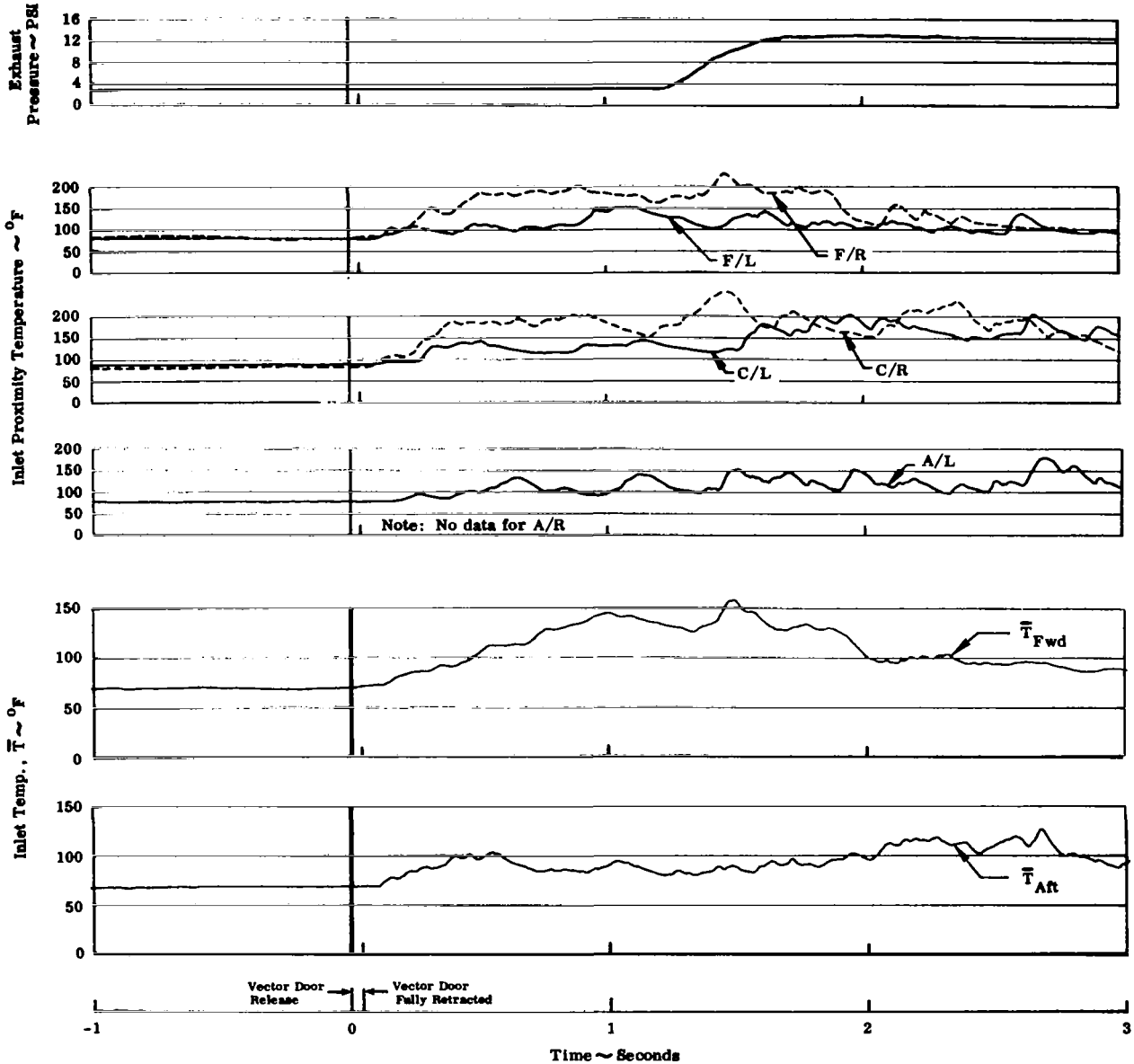
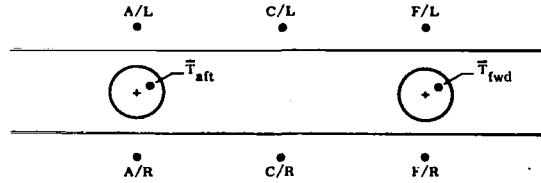


FIGURE 23. START-UP TRANSIENT - VECTOR DOOR WITH VARIABLE EXHAUST PRESSURE

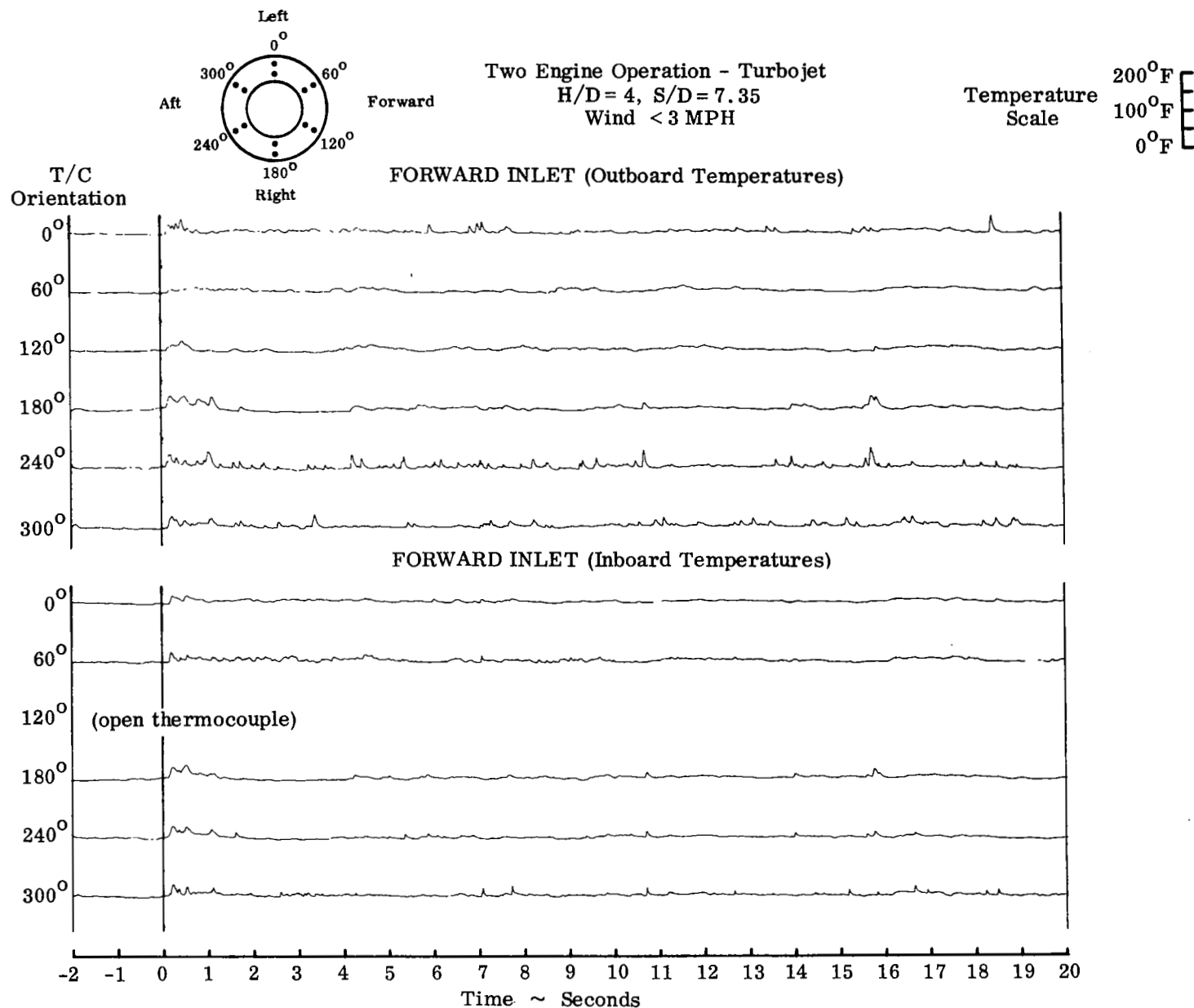
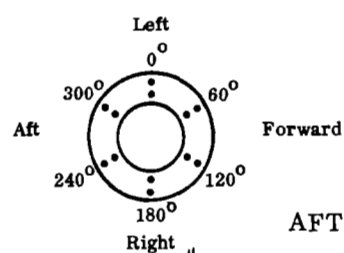


FIGURE 24. INLET TEMPERATURE HISTORY - LOW WIND

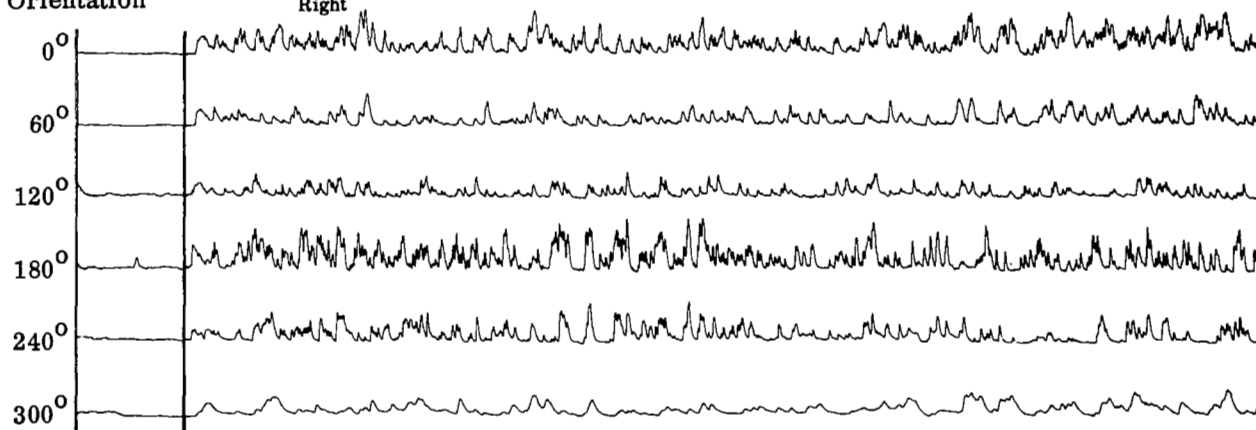


Two Engine Operation - Turbojet  
H/D = 4, S/D = 7.35  
Wind < 3 MPH

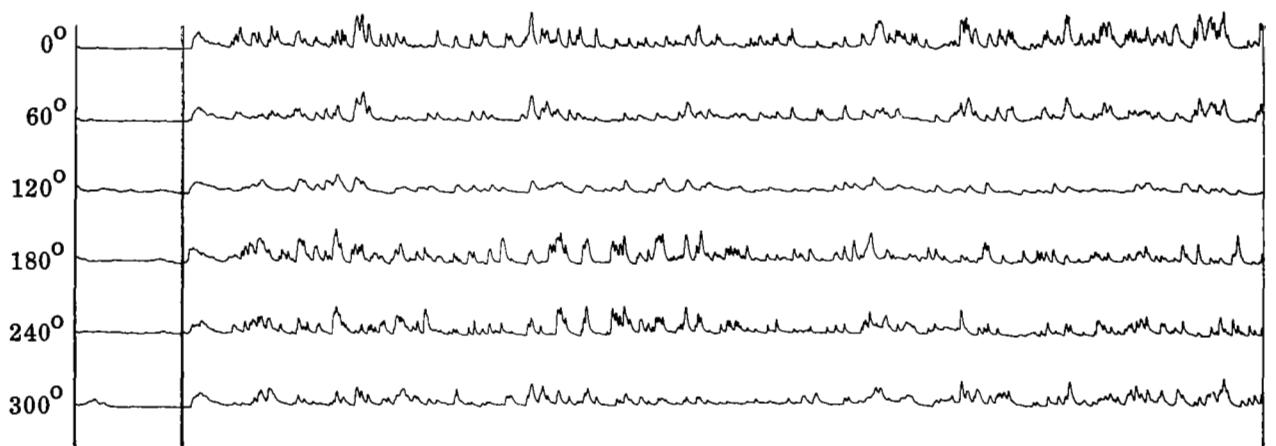
Temperature  
Scale 200°F  
100°F  
0°F

T/C  
Orientation

AFT INLET (Outboard Temperatures)

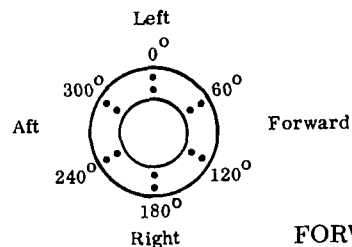


AFT INLET (Inboard Temperatures)



-2 -1 0 1 2 3 4 5 6 7 8 9 10 11 12 13 14 15 16 17 18 19 20  
Time ~ Seconds

FIGURE 24 (cont'd). INLET TEMPERATURE HISTORY - LOW WIND

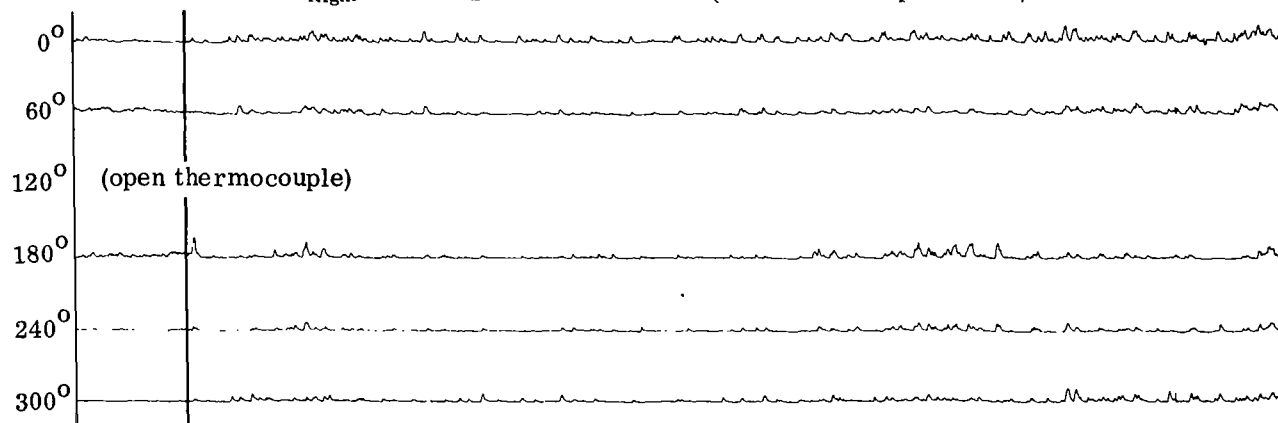


Two Engine Operation - Turbojet  
 $H/D = 4$ ,  $S/D = 7.35$   
 Wind = 20 MPH Headwind

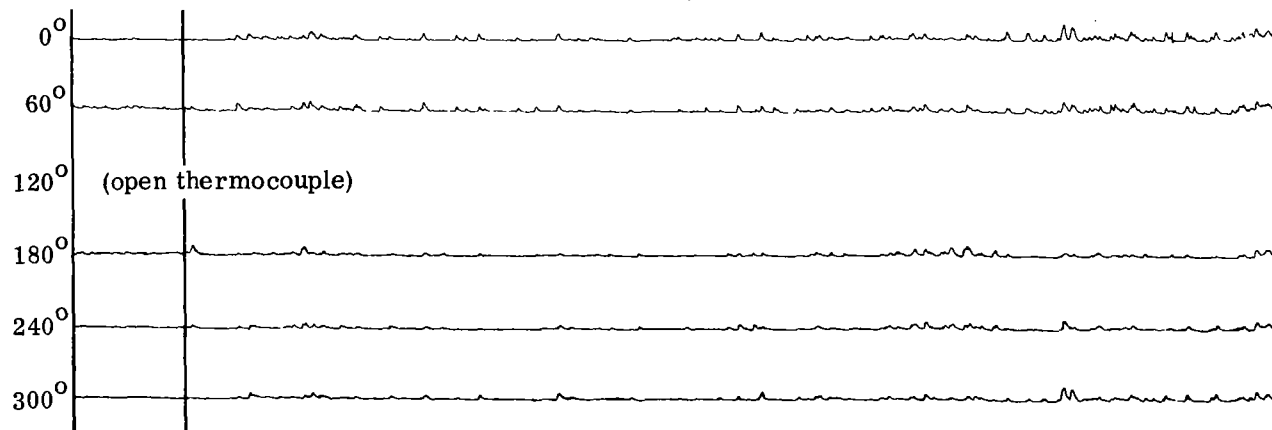
Temperature  
 Scale  
 200°F  
 100°F  
 0°F

T/C  
 Orientation

FORWARD INLET (Outboard Temperatures)



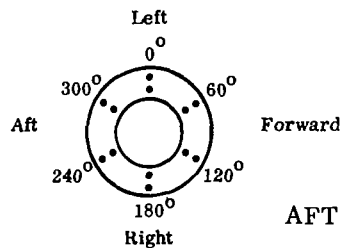
FORWARD INLET (Inboard Temperatures)



-2 -1 0 1 2 3 4 5 6 7 8 9 10 11 12 13 14 15 16 17 18 19 20

Time ~ Seconds

FIGURE 25. INLET TEMPERATURE HISTORY - 20 MPH HEADWIND

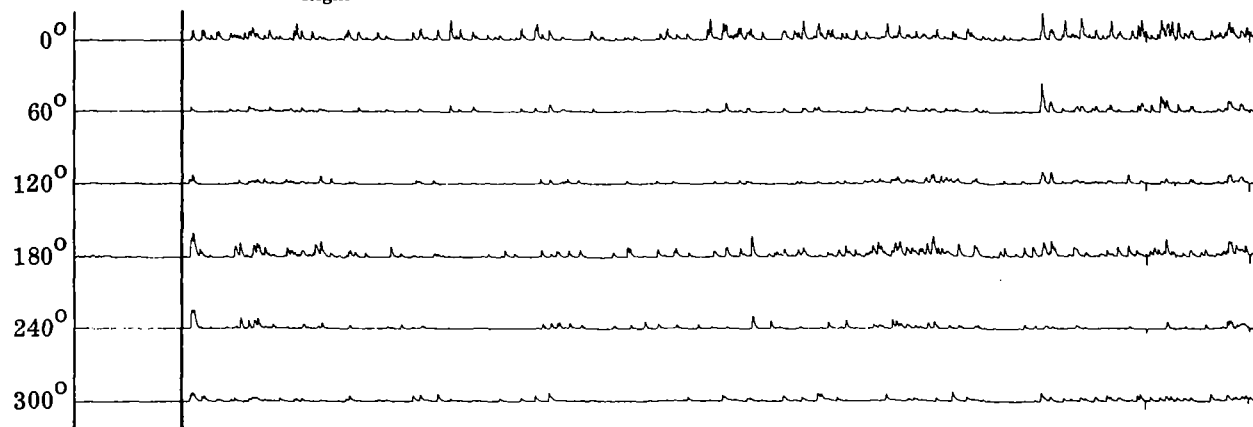


Two Engine Operation - Turbojet  
 H/D = 4, S/D = 7.35  
 Wind = 20 MPH Headwind

Temperature Scale  
 200°F  
 100°F  
 0°F

T/C  
 Orientation

AFT INLET (Outboard Temperatures)



AFT INLET (Inboard Temperatures)

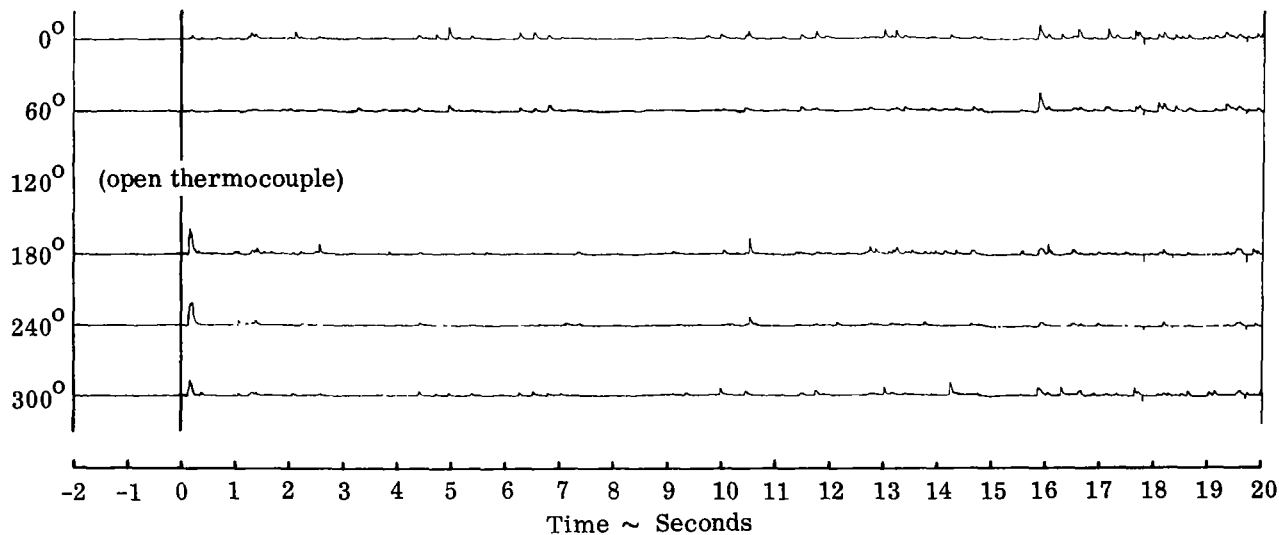


FIGURE 25 (cont'd). INLET TEMPERATURE HISTORY - 20 MPH HEADWIND

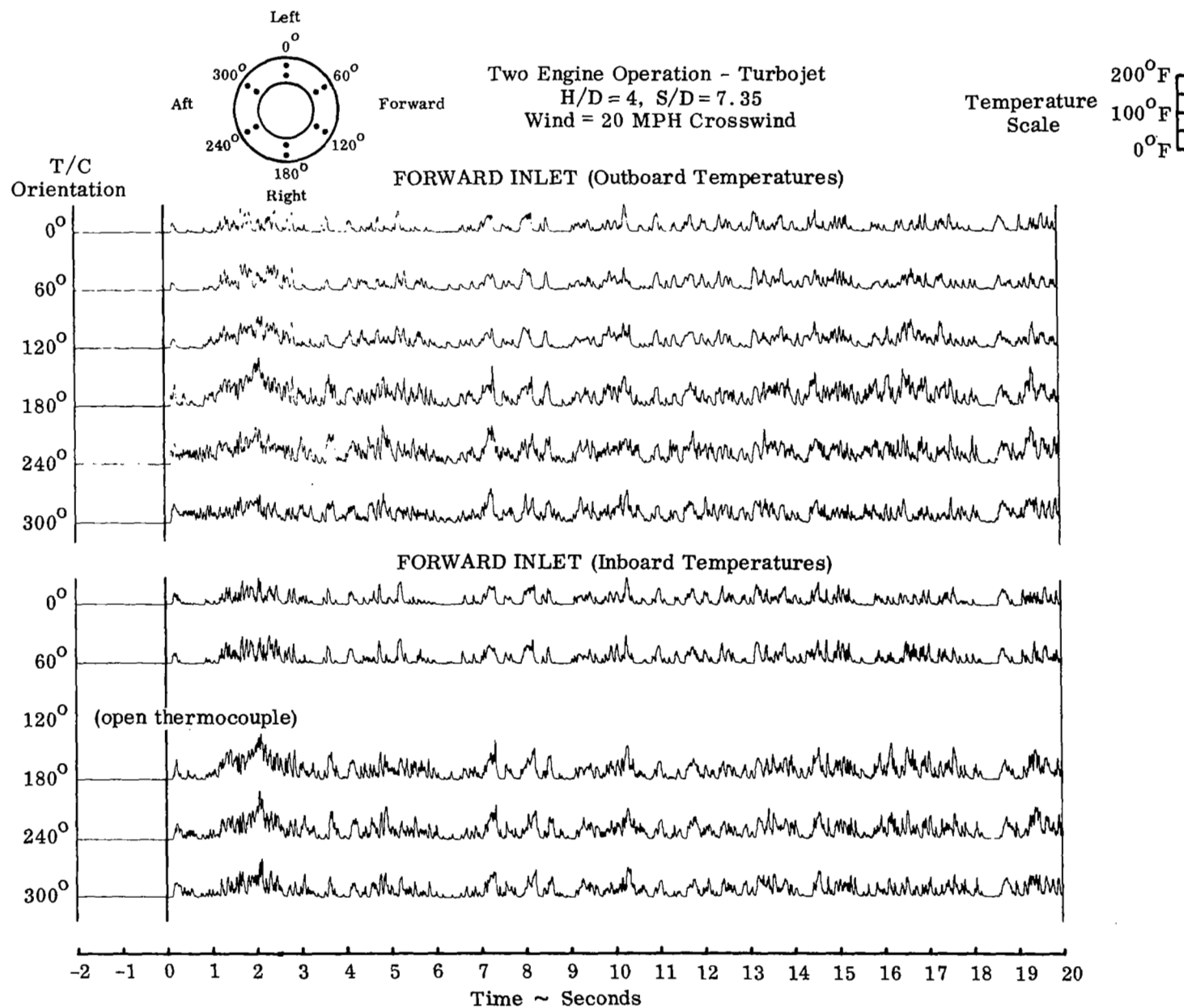


FIGURE 26. INLET TEMPERATURE HISTORY - 20 MPH CROSSWIND

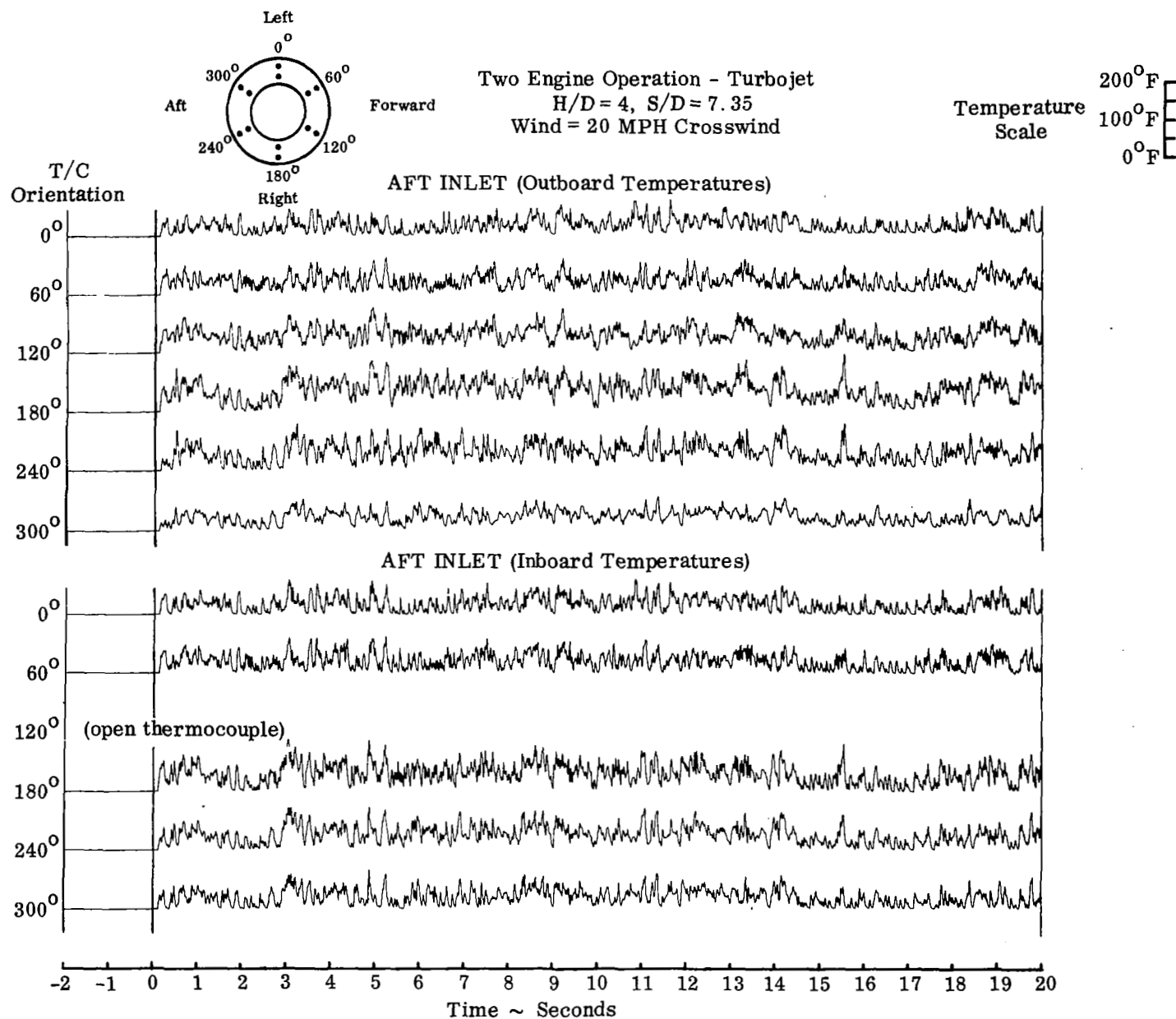


FIGURE 26 (cont'd). INLET TEMPERATURE HISTORY - 20 MPH CROSSWIND

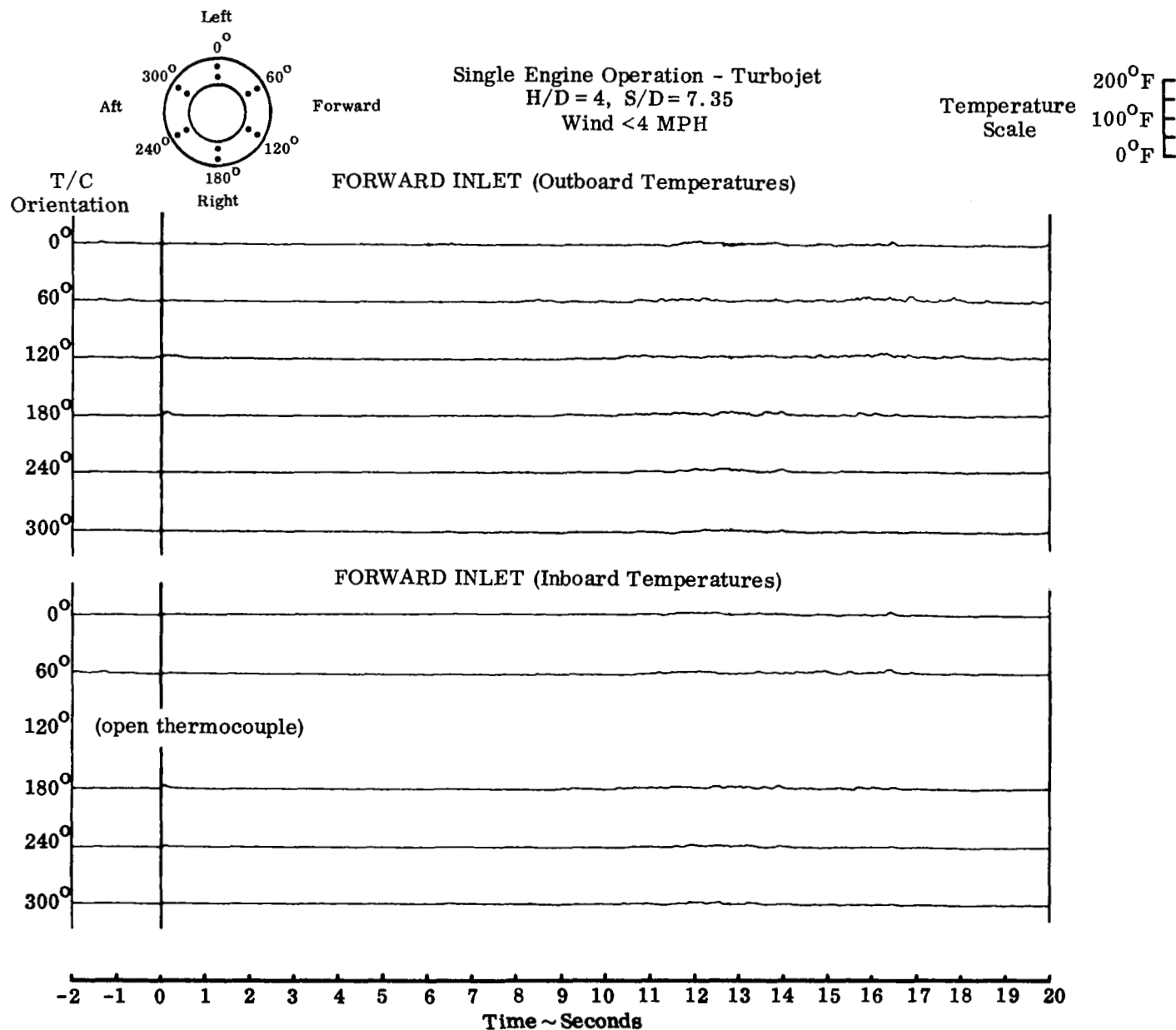


FIGURE 27. INLET TEMPERATURE HISTORY - LOW WIND



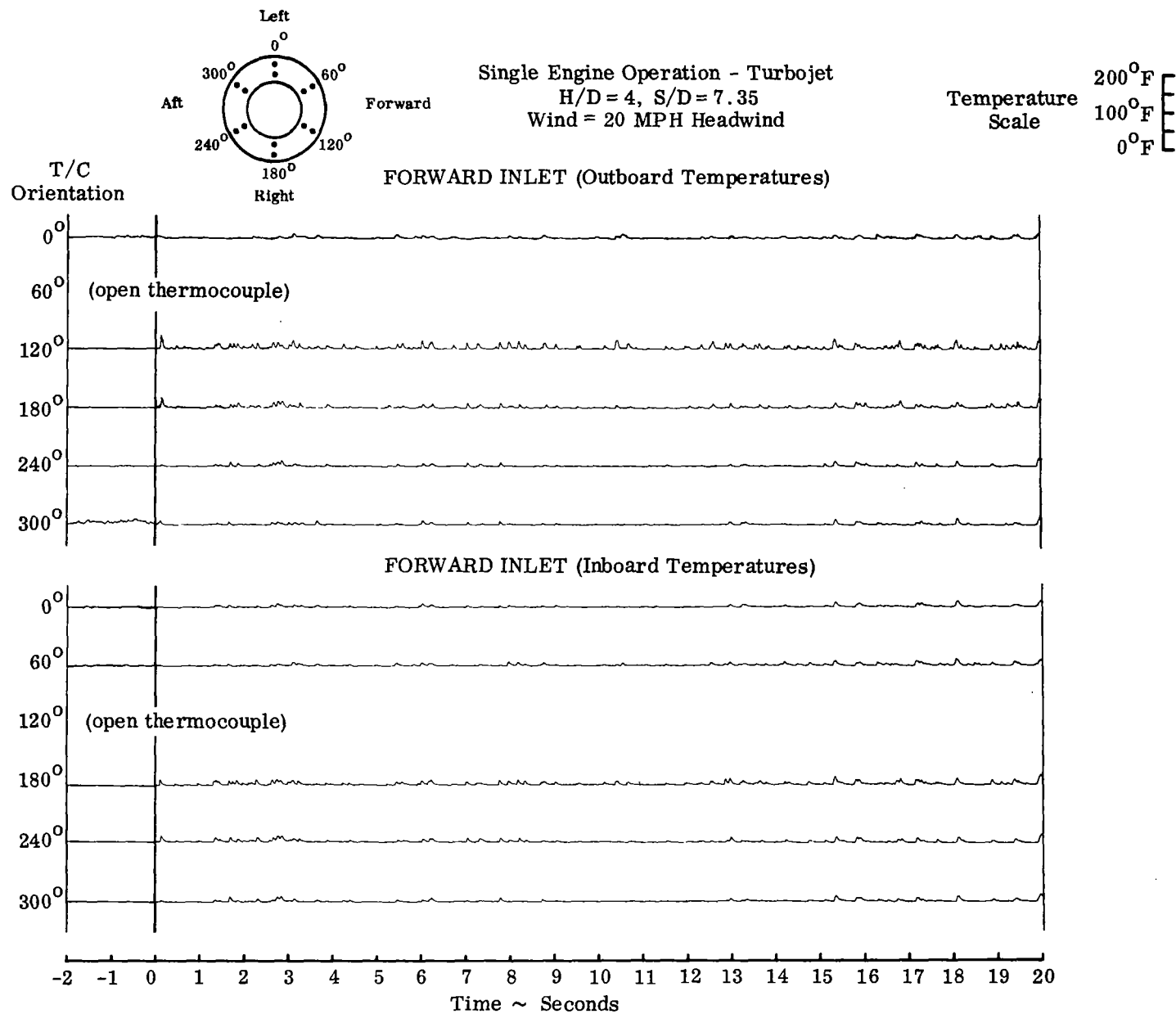


FIGURE 28. INLET TEMPERATURE HISTORY - 20 MPH HEADWIND

Two Engine Operation  
 $H/D = 4$ ,  $S/D = 7.35$   
Wind < 3 MPH

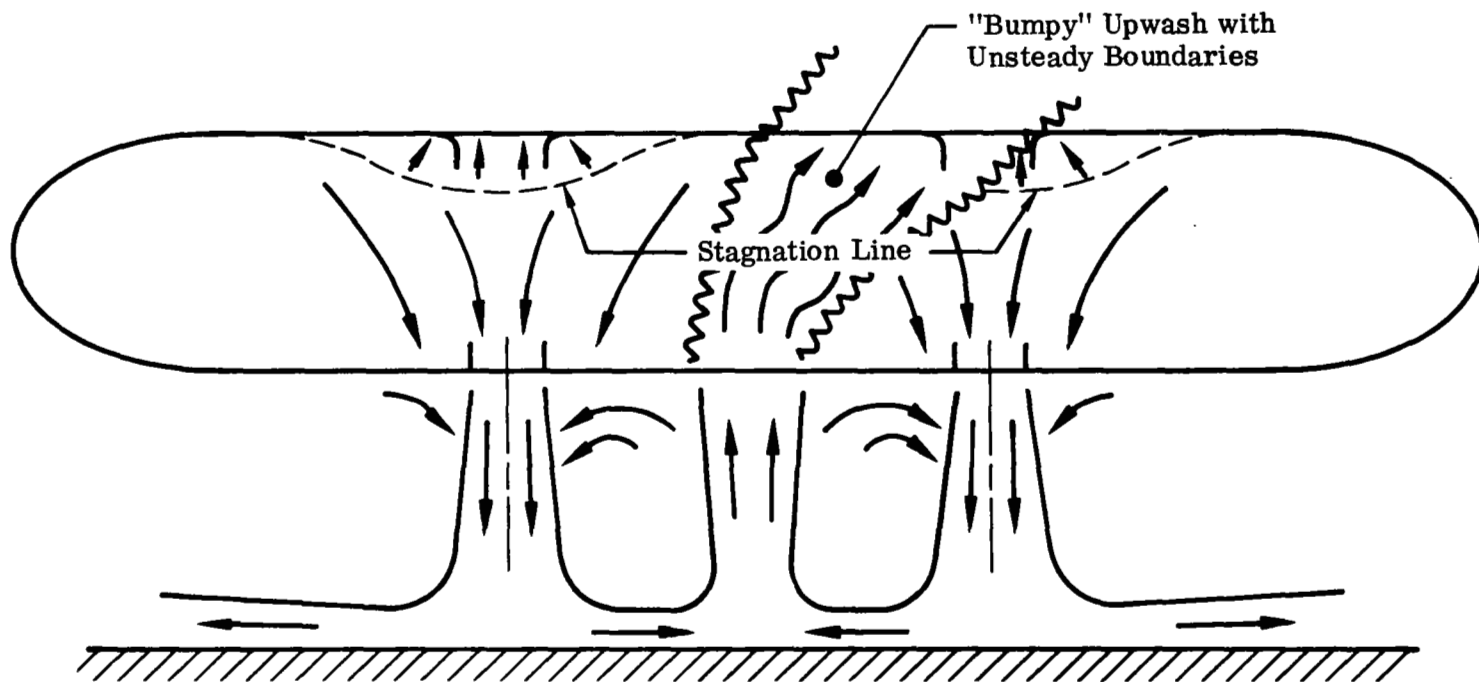
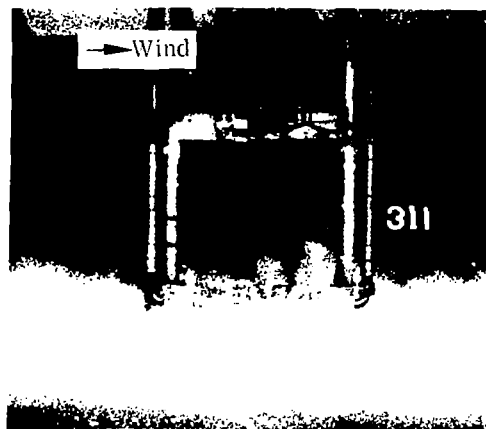
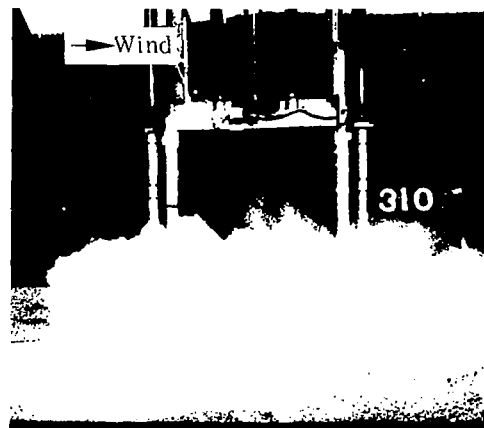


FIGURE 29. FLOW FIELD SCHEMATIC

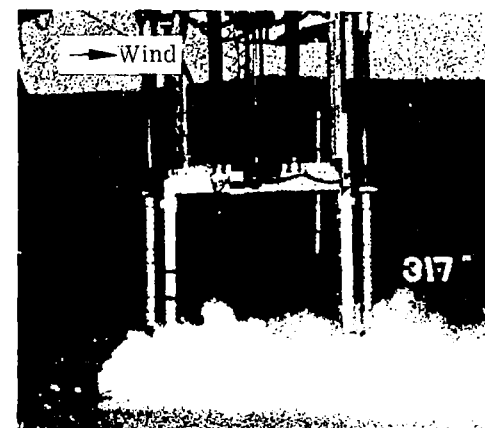
Two Engine Operation  
Turbojet  
 $H/D = 4$   
 $S/D = 7.35$



(a) Wind = 10 MPH



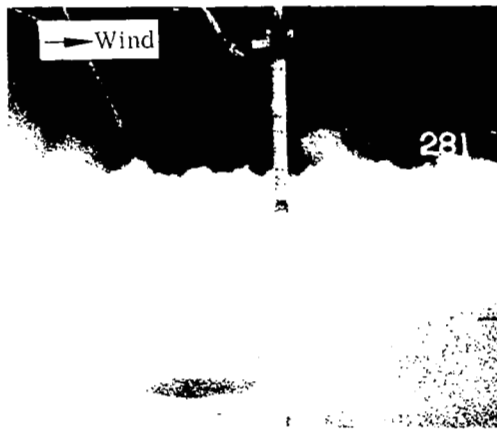
(b) Wind = 20 MPH



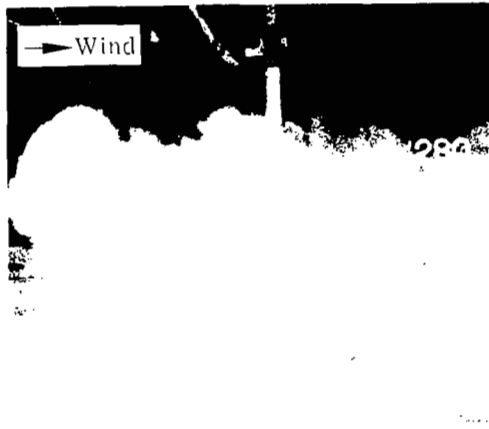
(c) Wind = 30 MPH

FIGURE 30. EFFECT OF HEADWIND ON RECIRCULATING FLOW FIELD

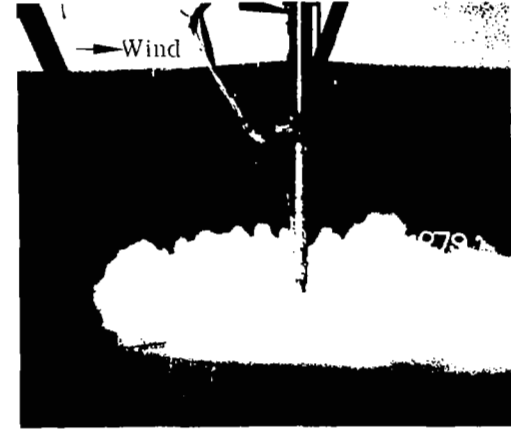
Two Engine Operation  
Turbojet  
 $H/D = 4$   
 $S/D = 7.35$



(a) Wind = 10 MPH



(b) Wind = 20 MPH



(c) Wind = 30 MPH

FIGURE 31. EFFECT OF CROSSWIND ON RECIRCULATING FLOW FIELD

Two Engine Operation - Turbojet  
 $H/D = 4$ ,  $S/D = 7.35$   
 Wind < 3 MPH

# FORWARD INLET

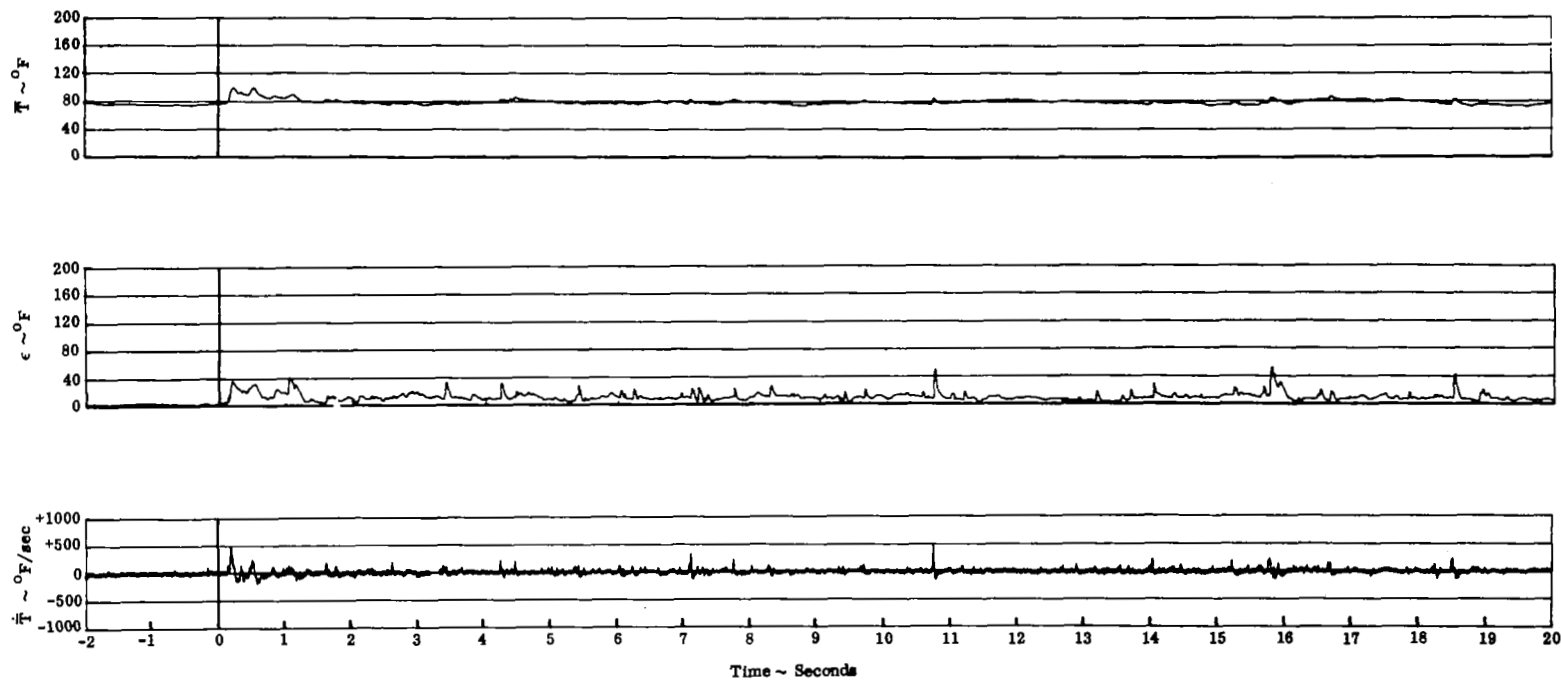


FIGURE 32. INGESTION CHARACTERISTICS HISTORY - LOW WIND

Two Engine Operation - Turbojet  
H/D = 4, S/D = 7.35  
Wind < 3 MPH

AFT INLET

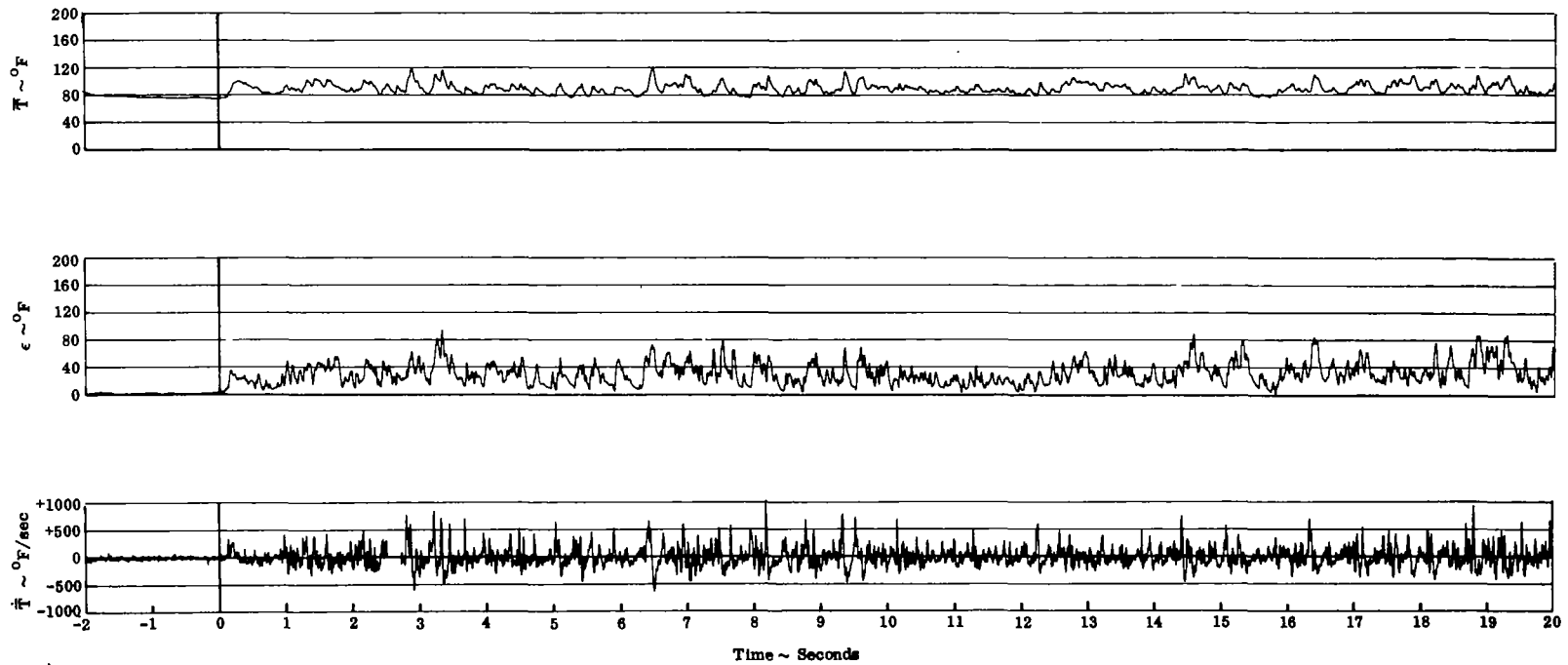


FIGURE 32 (cont'd). INGESTION CHARACTERISTICS HISTORY - LOW WIND

Two Engine Operation - Turbojet  
 $H/D = 4$ ,  $S/D = 7.35$   
 Wind = 20 MPH Headwind

FORWARD INLET

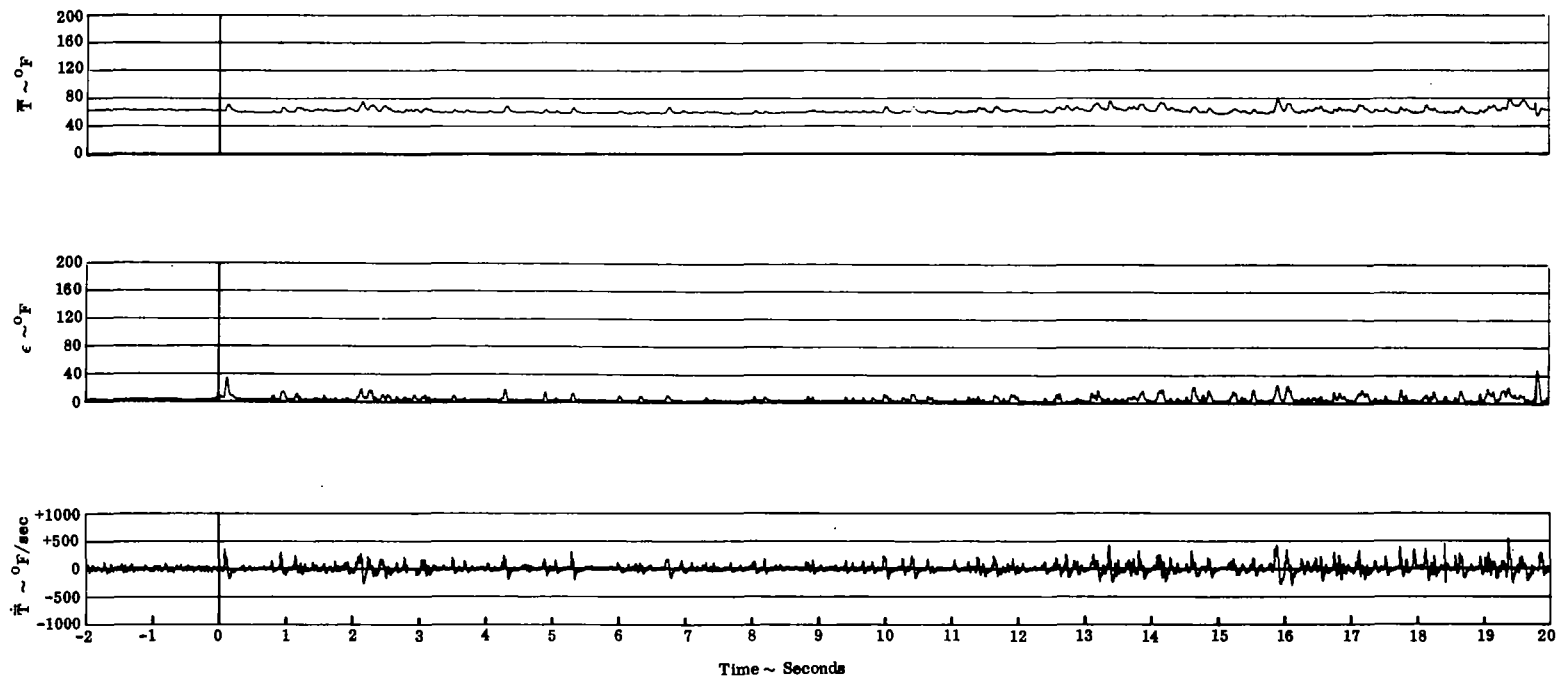


FIGURE 33. INGESTION CHARACTERISTICS HISTORY - 20 MPH HEADWIND

Two Engine Operation - Turbojet  
H/D = 4, S/D = 7.35  
Wind = 20 MPH Headwind

AFT INLET

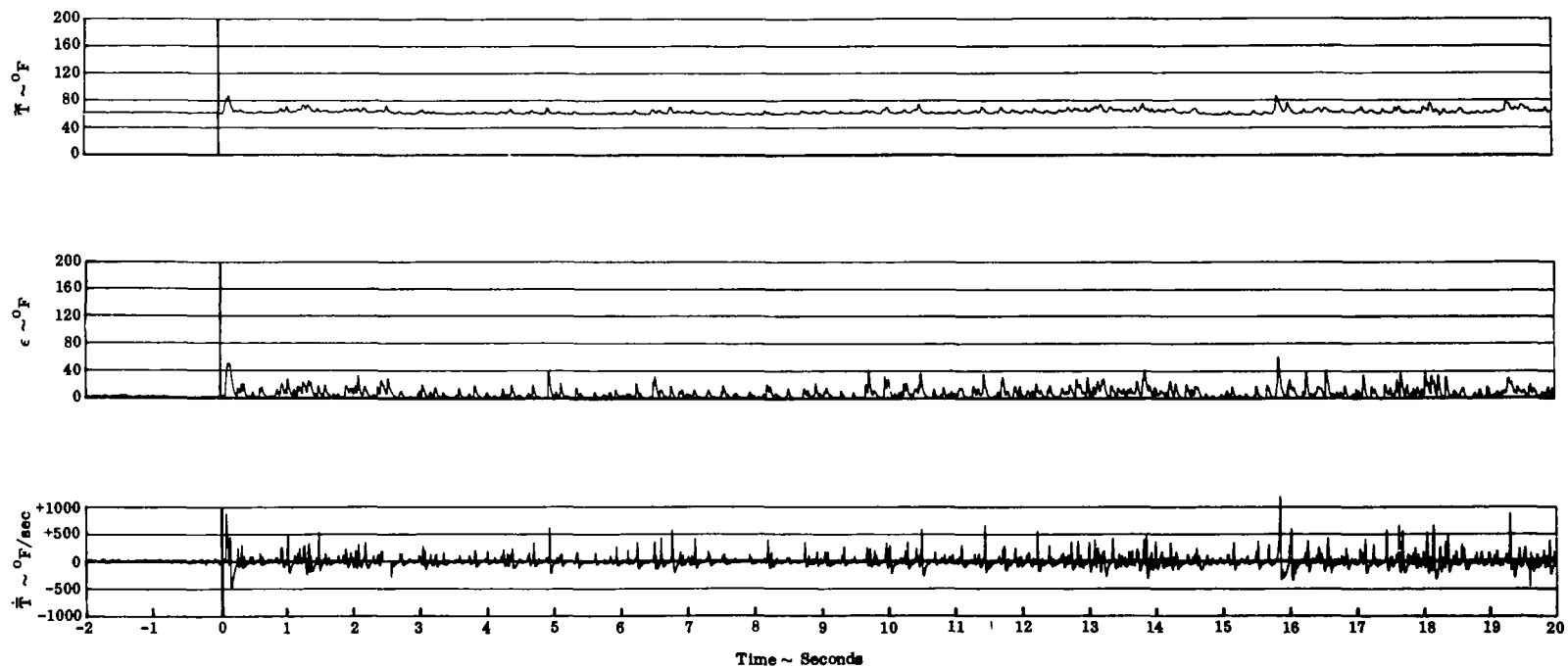


FIGURE 33 (cont'd). INGESTION CHARACTERISTICS HISTORY - 20 MPH HEADWIND



Two Engine Operation - Turbojet  
 $H/D = 4$ ,  $S/D = 7.35$   
 Wind = 20 MPH Crosswind

FORWARD INLET

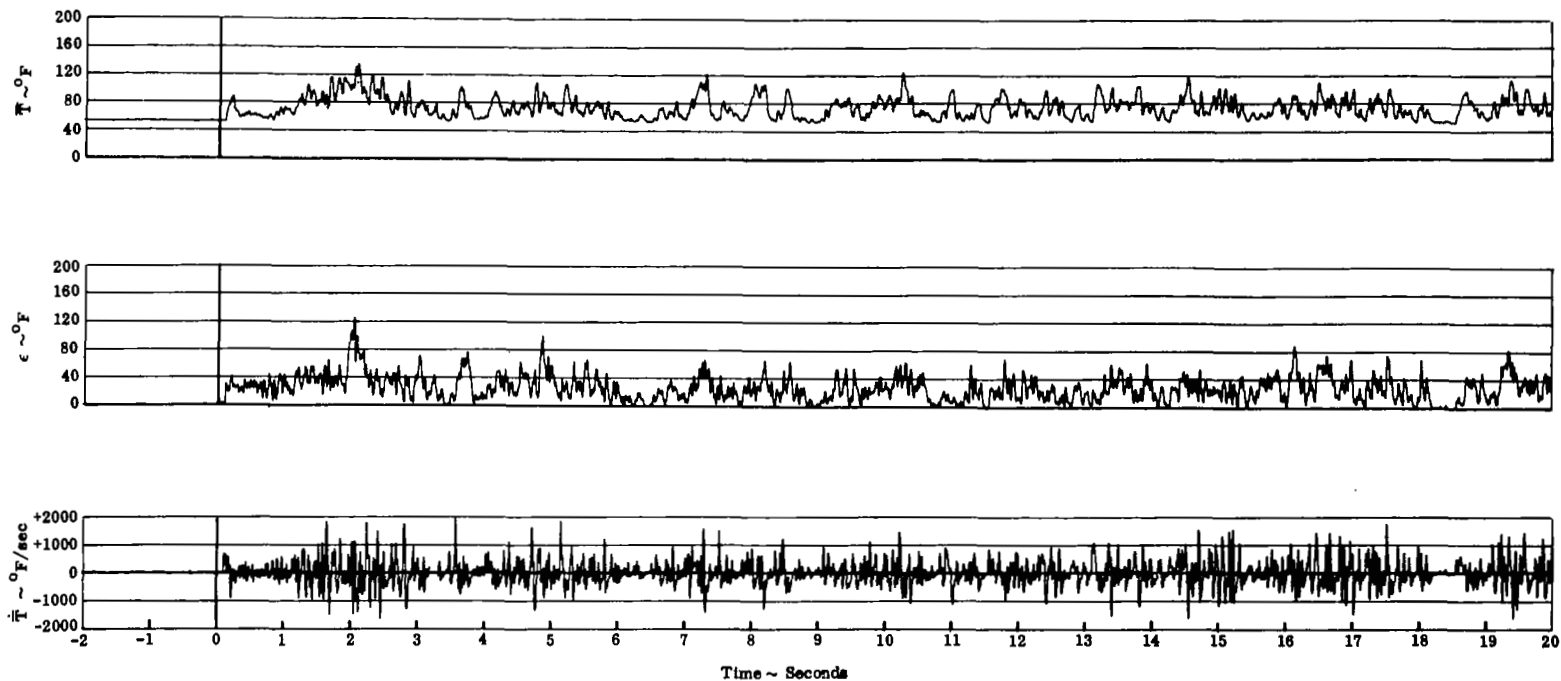


FIGURE 34. INGESTION CHARACTERISTICS HISTORY - 20 MPH CROSSWIND

Two Engine Operation - Turbojet  
H/D = 4, S/D = 7.35  
Wind = 20 MPH Crosswind

AFT INLET

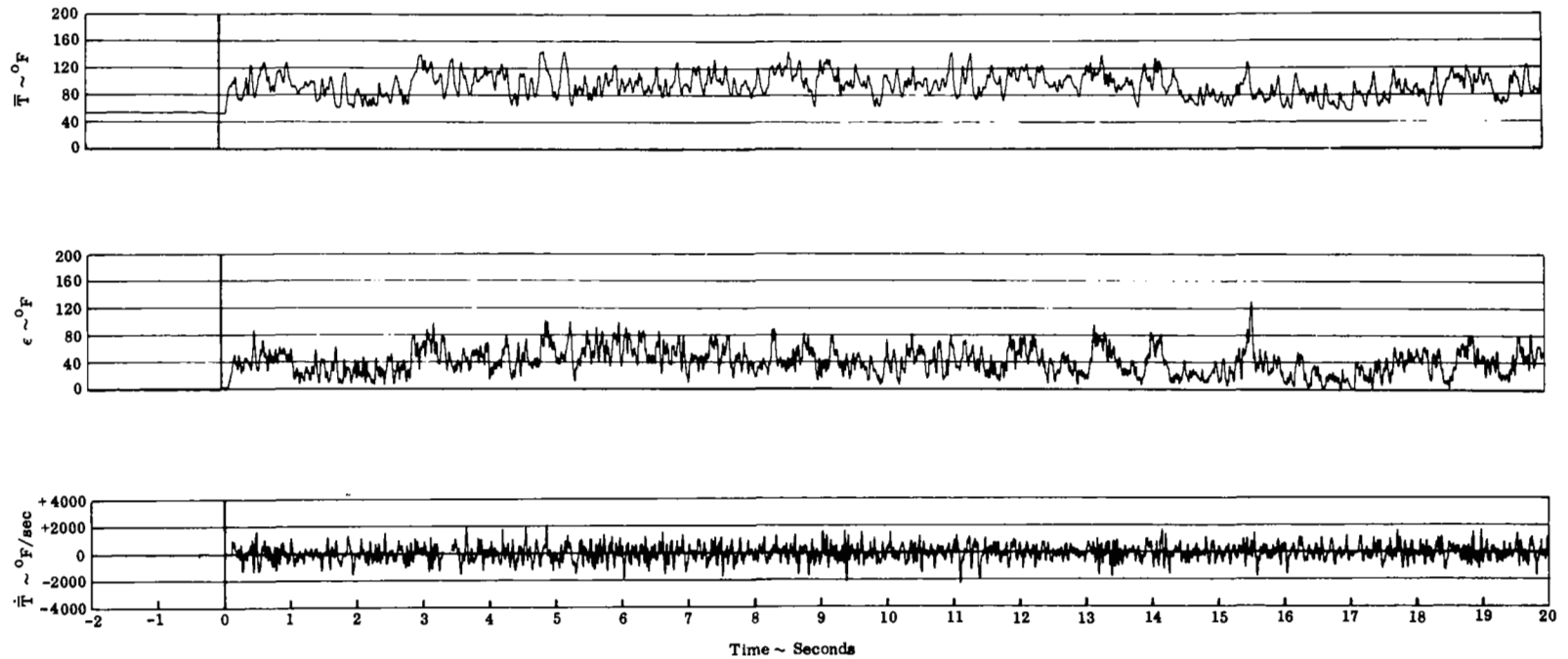


FIGURE 34 (cont'd). INGESTION CHARACTERISTICS HISTORY - 20 MPH CROSSWIND

Single Engine Operation - Turbojet  
H/D = 4, S/D = 7.35  
Wind < 3 MPH

FORWARD INLET

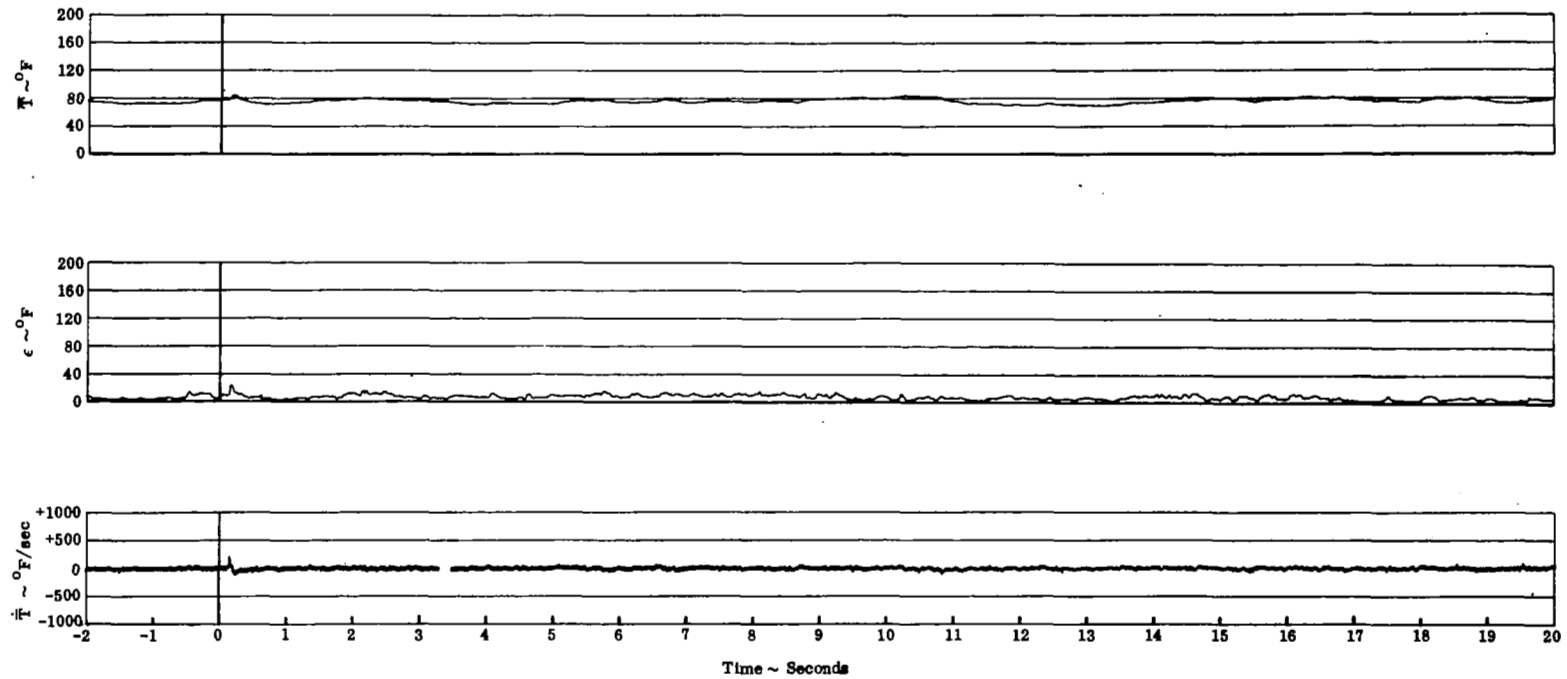


FIGURE 35. INGESTION CHARACTERISTICS HISTORY - LOW WIND

Single Engine Operation - Turbojet  
 $H/D = 4$ ,  $S/D = 7.35$   
 Wind = 20 MPH Headwind

# FORWARD INLET

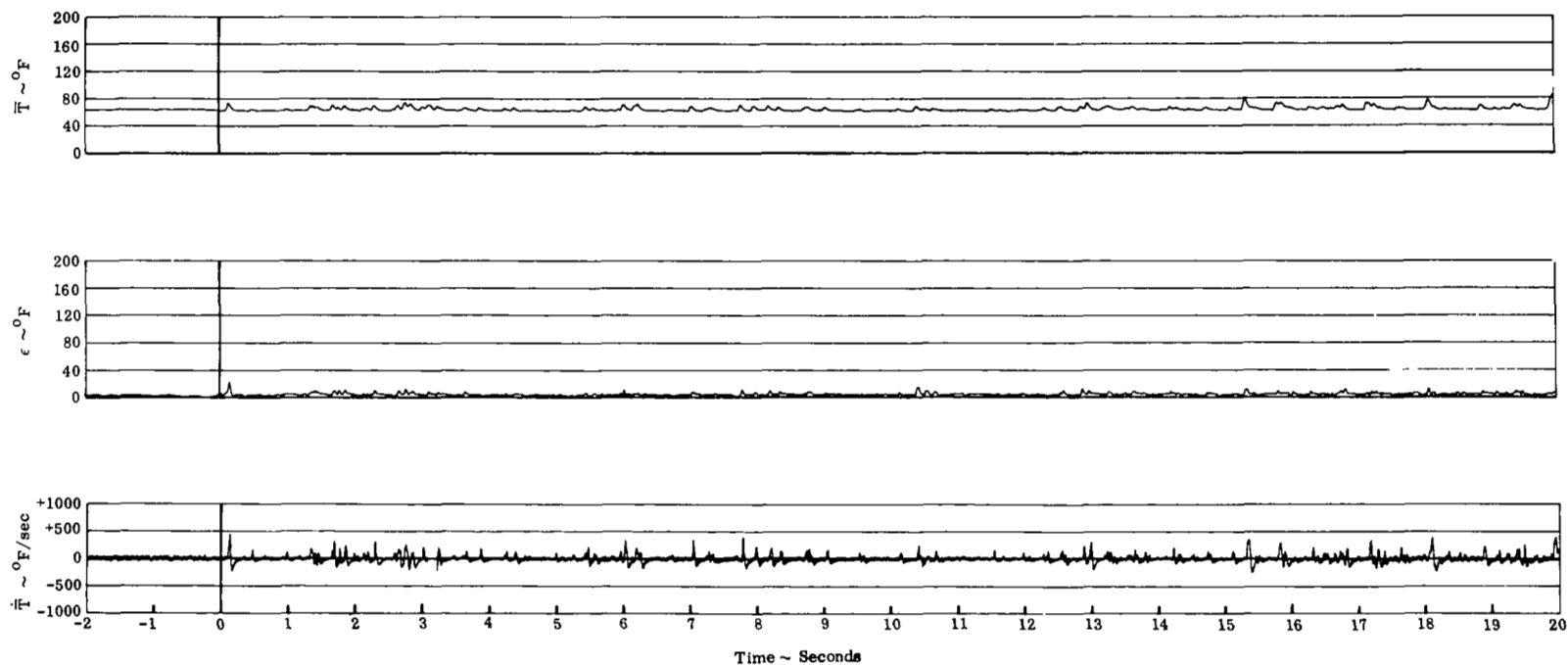


FIGURE 36. INGESTION CHARACTERISTICS HISTORY - 20 MPH HEADWIND

Two Engine Operation  
Turbojet  
Wind < 3 MPH

S/D  
○ 4.90  
△ 7.35  
□ 9.80

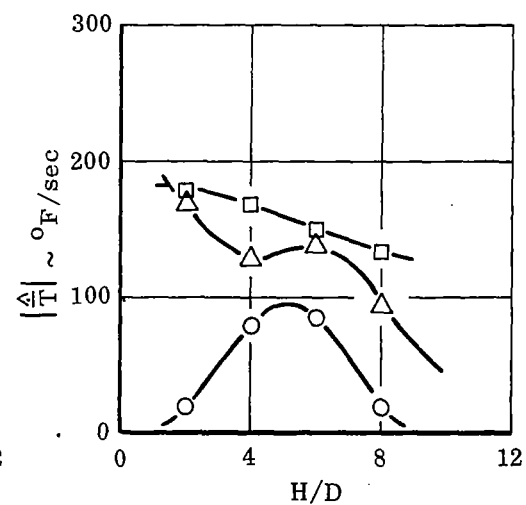
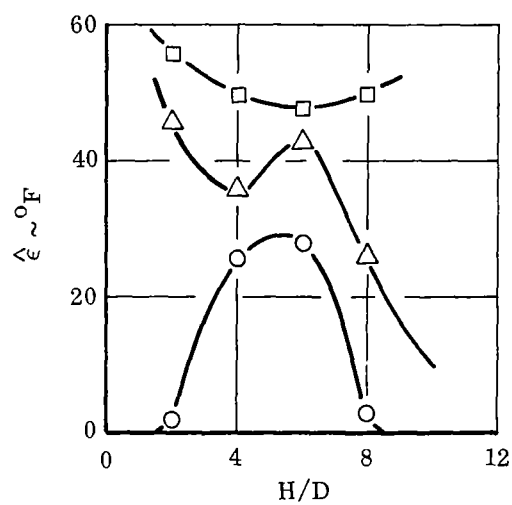
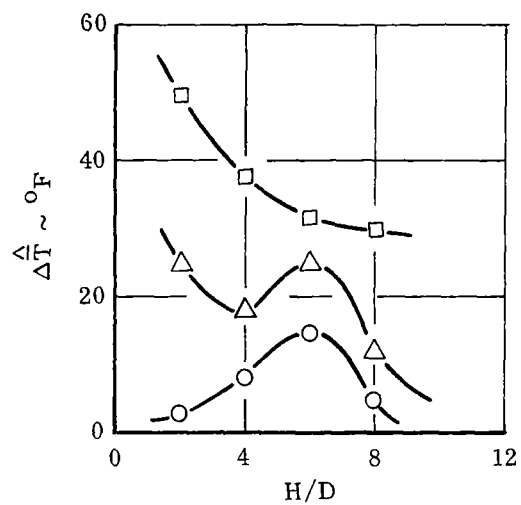


FIGURE 37. EFFECT OF H/D AND S/D ON TIME-AVERAGE  
INGESTION CHARACTERISTICS - TURBOJET

Two Engine Operation  
 Turbojet  
 $H/D = 4$   
 $S/D = 7.35$

○ Headwind  
 △ Crosswind

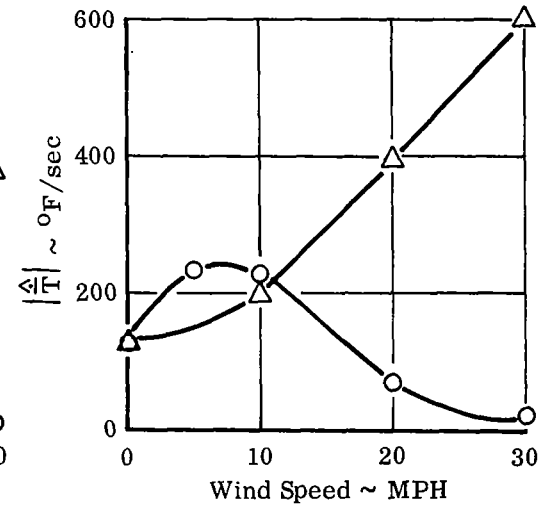
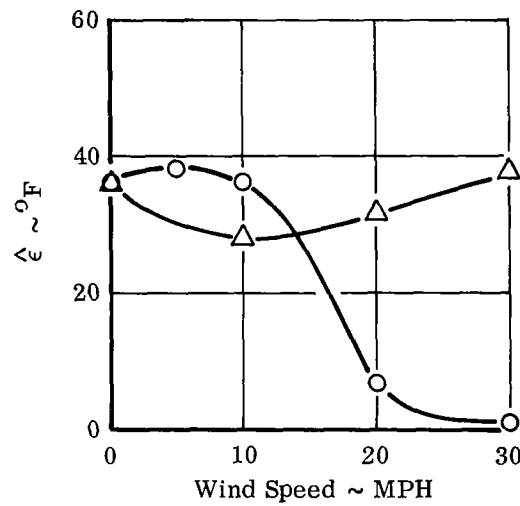
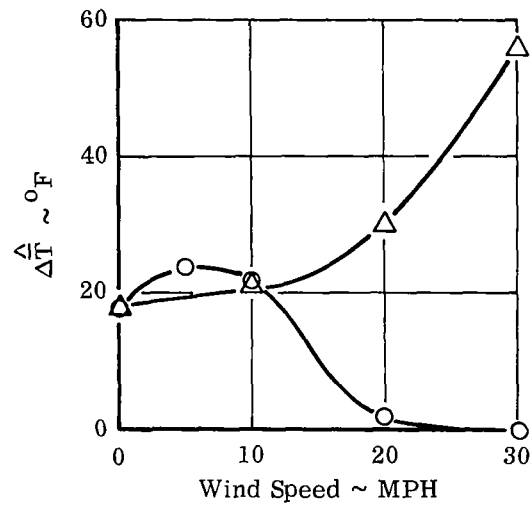


FIGURE 38. EFFECT OF WIND ON TIME-AVERAGE INGESTION CHARACTERISTICS - TURBOJET

Two Engine Operation  
Turbojet  
 $S/D \approx 7.35$

- Wind < 3 MPH  
△ 20 MPH Headwind  
□ 20 MPH Crosswind

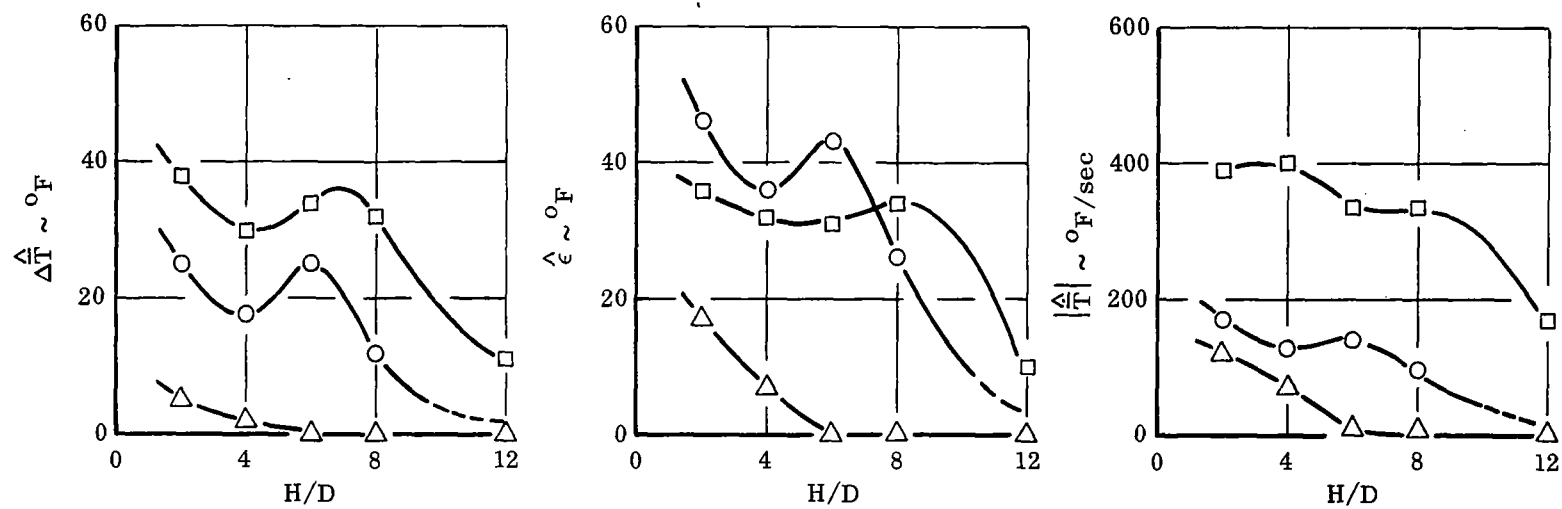


FIGURE 39. EFFECT OF WIND ON TIME-AVERAGE INGESTION CHARACTERISTICS - TURBOJET

Two Engine Operation  
 Turbofan  
 $S/D = 7.35$   
 Wind < 3 MPH

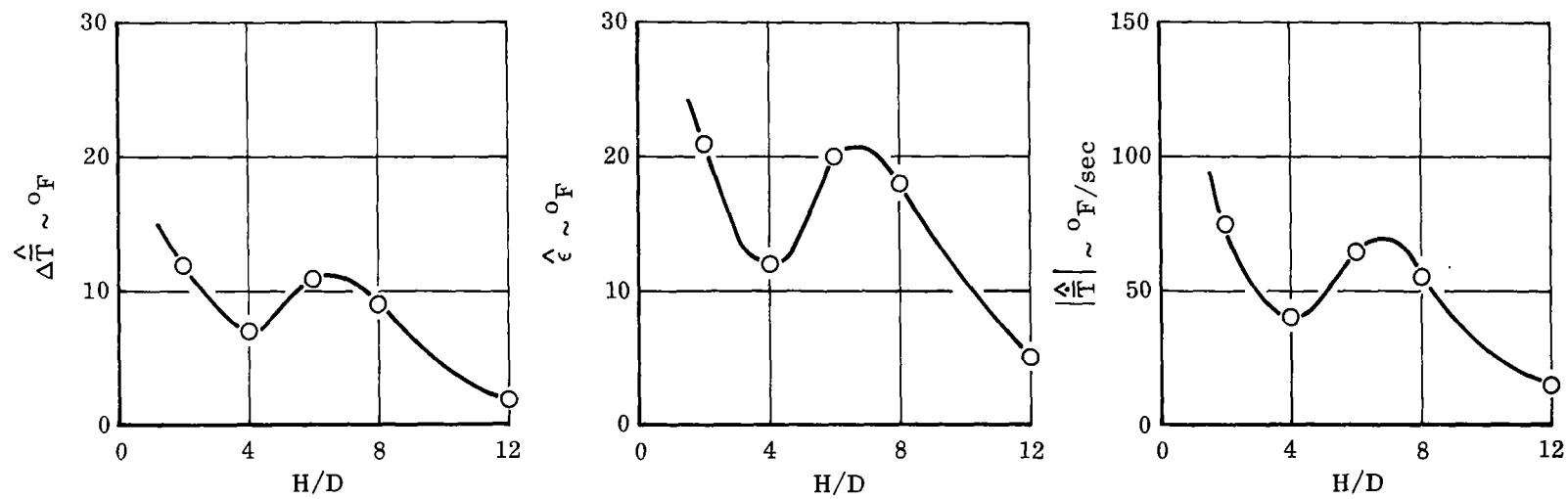


FIGURE 40. EFFECT OF H/D ON TIME-AVERAGE INGESTION CHARACTERISTICS - TURBOFAN



Two Engine Operation  
 Turbofan  
 $H/D = 4$   
 $S/D = 7.35$

○ Headwind  
 △ Crosswind

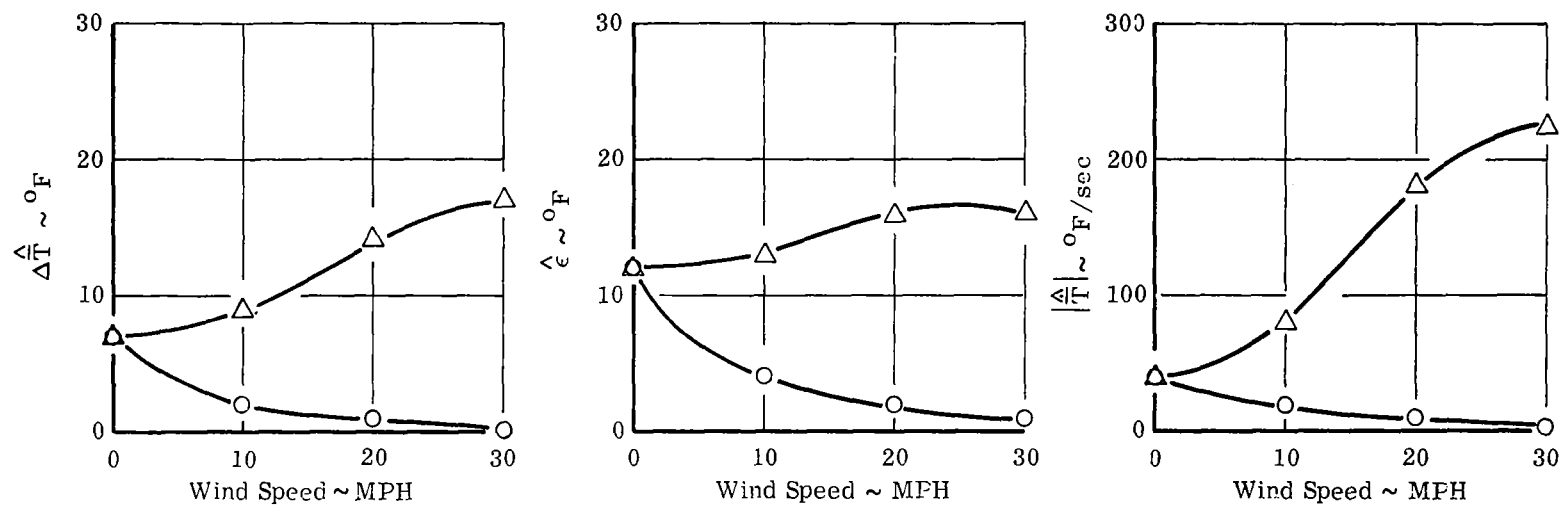


FIGURE 41. EFFECT OF WIND ON TIME-AVERAGE INGESTION CHARACTERISTICS - TURBOFAN

Two Engine Operation  
 Turbojet  
 $H/D = 4$   
 $S/D = 7.35$   
 Wind < 3 MPH

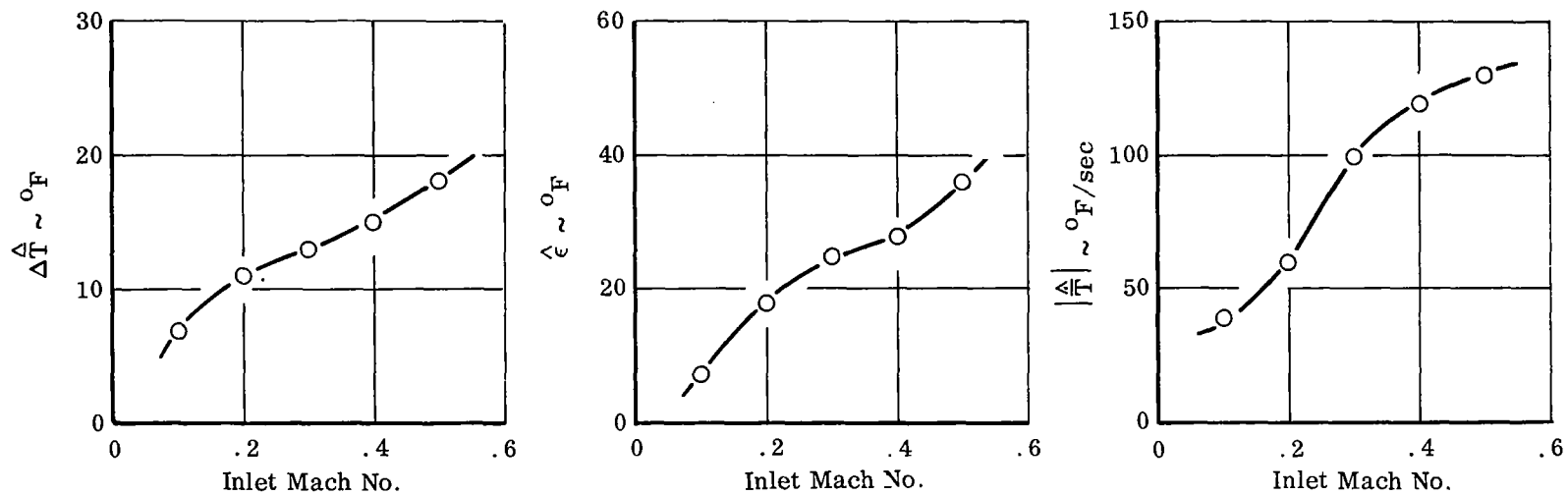


FIGURE 42. EFFECT OF INLET MACH NUMBER ON TIME-AVERAGE INGESTION CHARACTERISTICS

Two Engine Operation  
 $H/D = 4$   
 $S/D = 7.35$   
 Wind < 3 MPH

$T_n$   
 $\circ$  440°F  
 $\triangle$  820°F  
 $\square$  1200°F

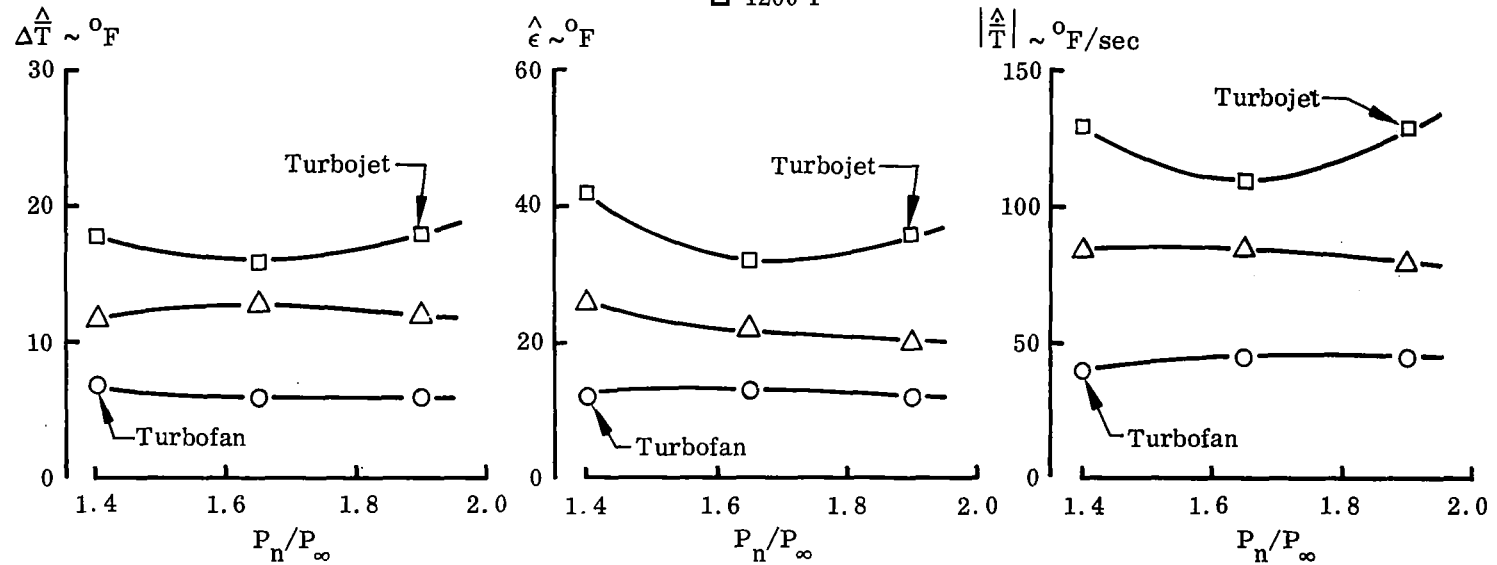


FIGURE 43. EFFECT OF EXHAUST PRESSURE/TEMPERATURE ON TIME-AVERAGE INGESTION CHARACTERISTICS

Two Engine Operation

H/D = 4

S/D = 7.35

Wind < 3 MPH

$T_n$   
 ○ 440°F  
 △ 820°F  
 □ 1200°F

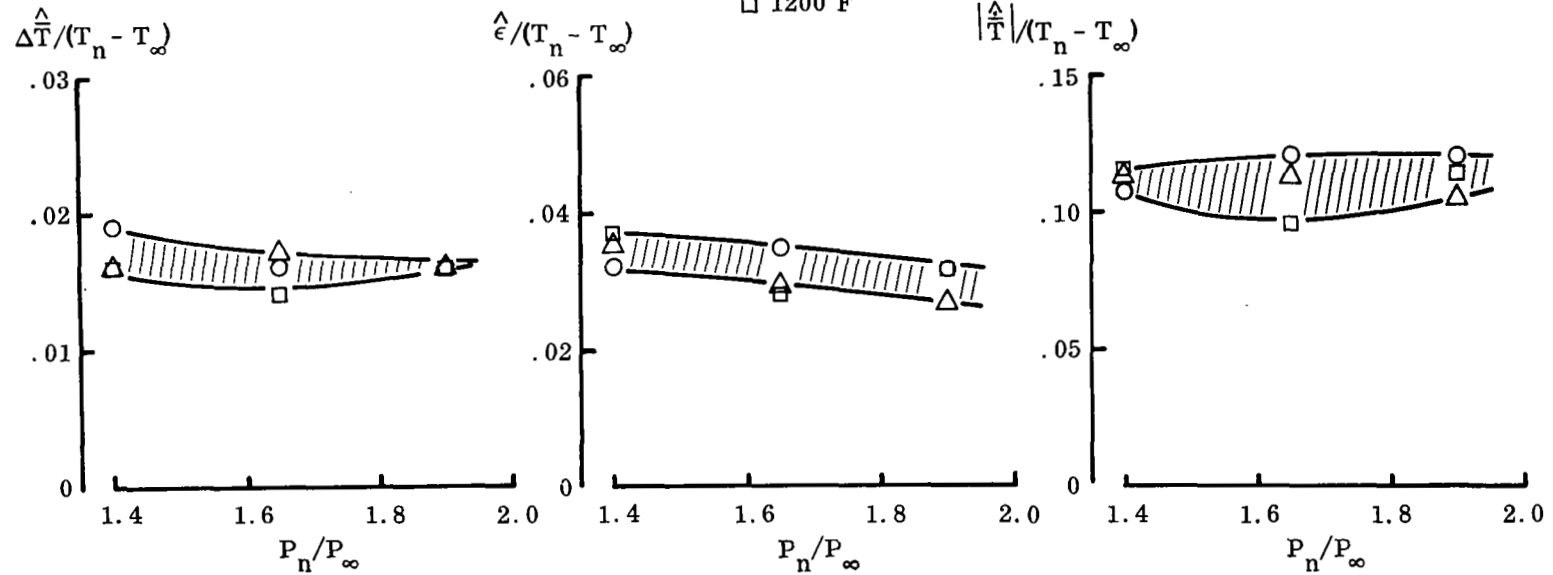


FIGURE 44. EFFECT OF EXHAUST PRESSURE/TEMPERATURE ON TIME-AVERAGE INGESTION CHARACTERISTICS

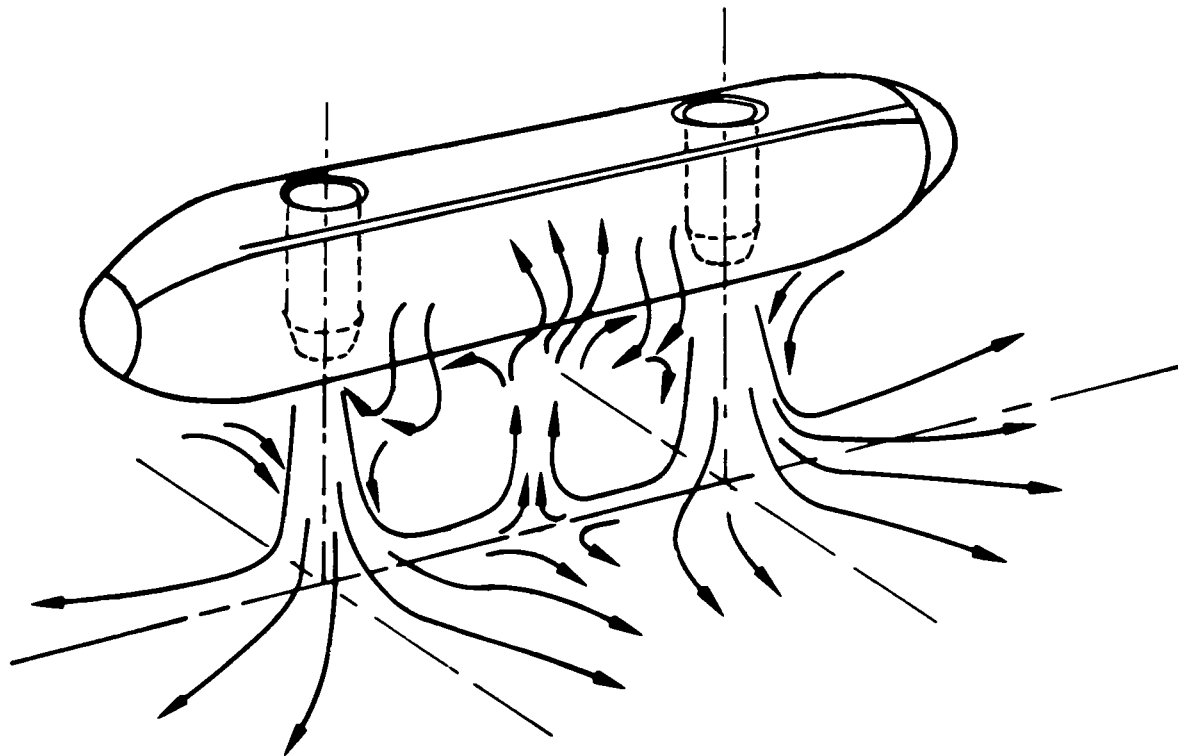


FIGURE 45. FLOW STRUCTURE BETWEEN GROUND PLANE AND POD FOR TWO  
ENGINE OPERATION AT LOW WIND CONDITIONS

Two Engine Operation  
Turbojet  
Wind <3 MPH

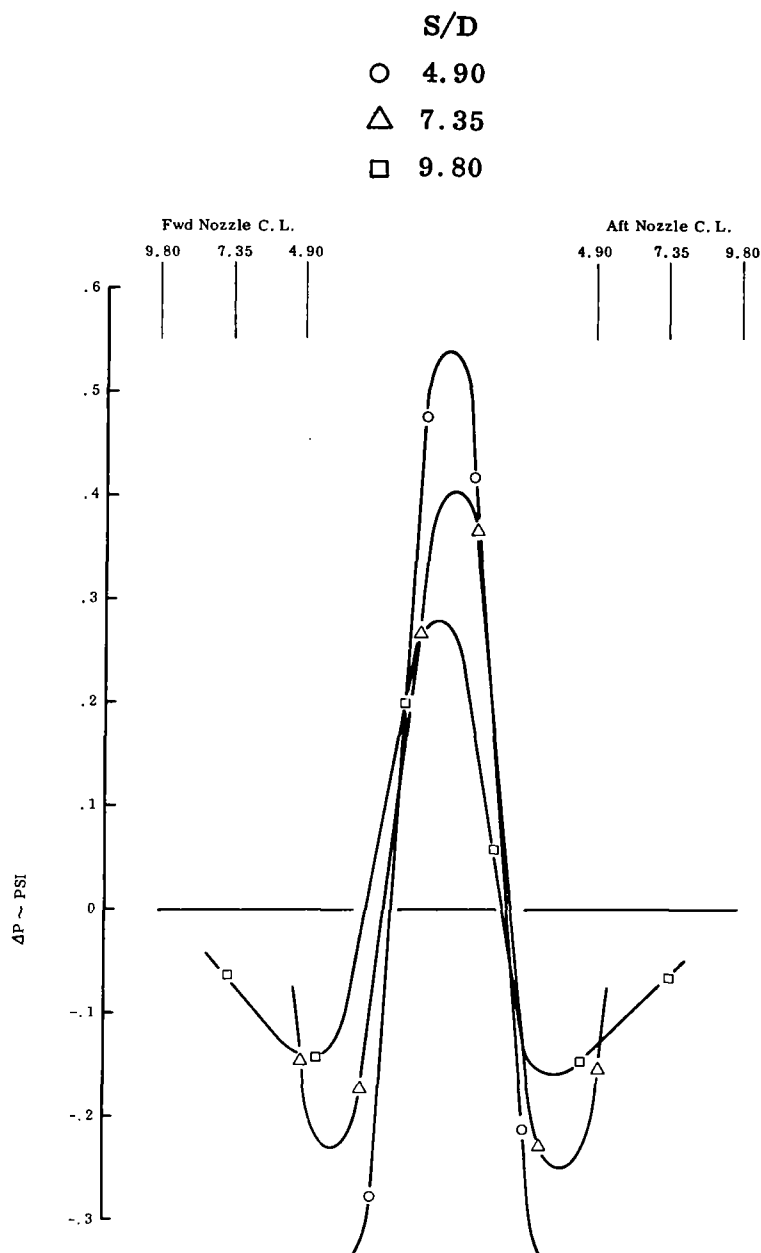
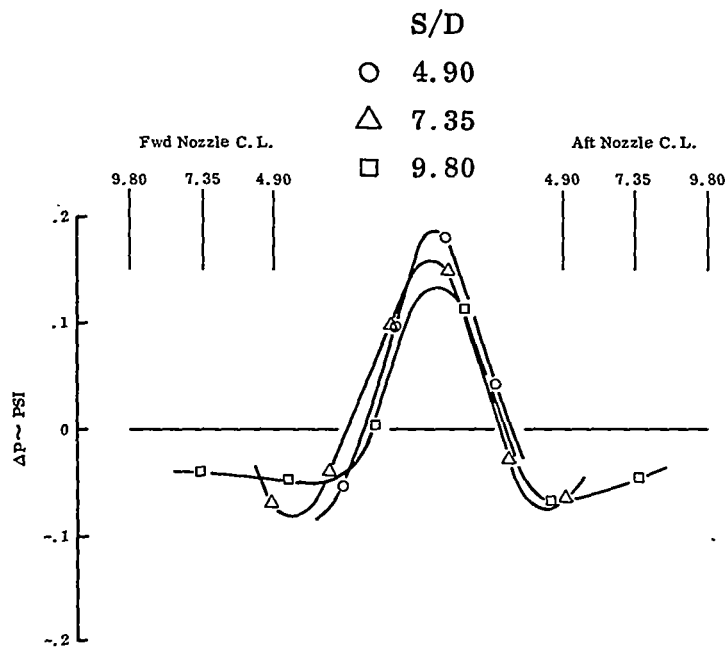
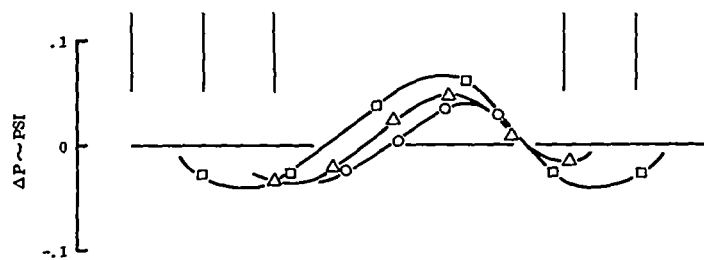


FIGURE 46. EFFECT OF  $H/D$  AND  $S/D$  ON POD PRESSURE DISTRIBUTION - LOW WIND

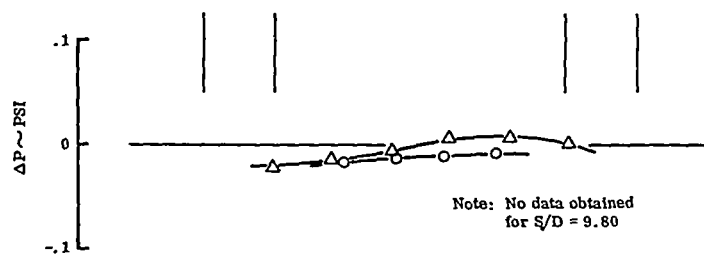
Two Engine Operation  
Turbojet  
Wind <3 MPH



(b)  $H/D = 4$



(c)  $H/D = 6$



(d)  $H/D = 8$

FIGURE 46 (cont'd). EFFECT OF  $H/D$  AND  $S/D$  ON POD PRESSURE DISTRIBUTION - LOW WIND

Two Engine Operation  
Turbojet  
Wind < 3 MPH

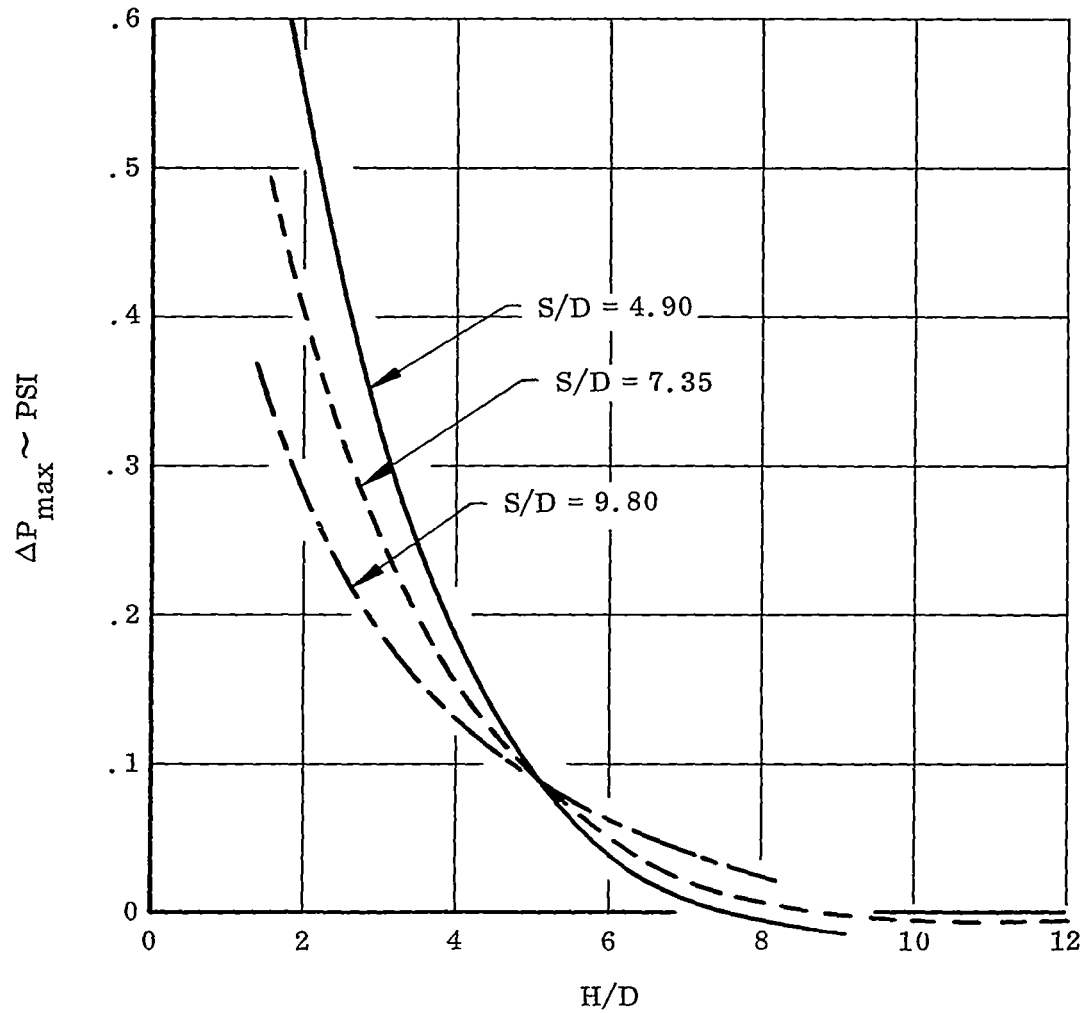


FIGURE 47. EFFECT OF  $H/D$  AND  $S/D$  ON POD PEAK PRESSURE



Two Engine Operation  
Turbojet  
Wind < 3 MPH

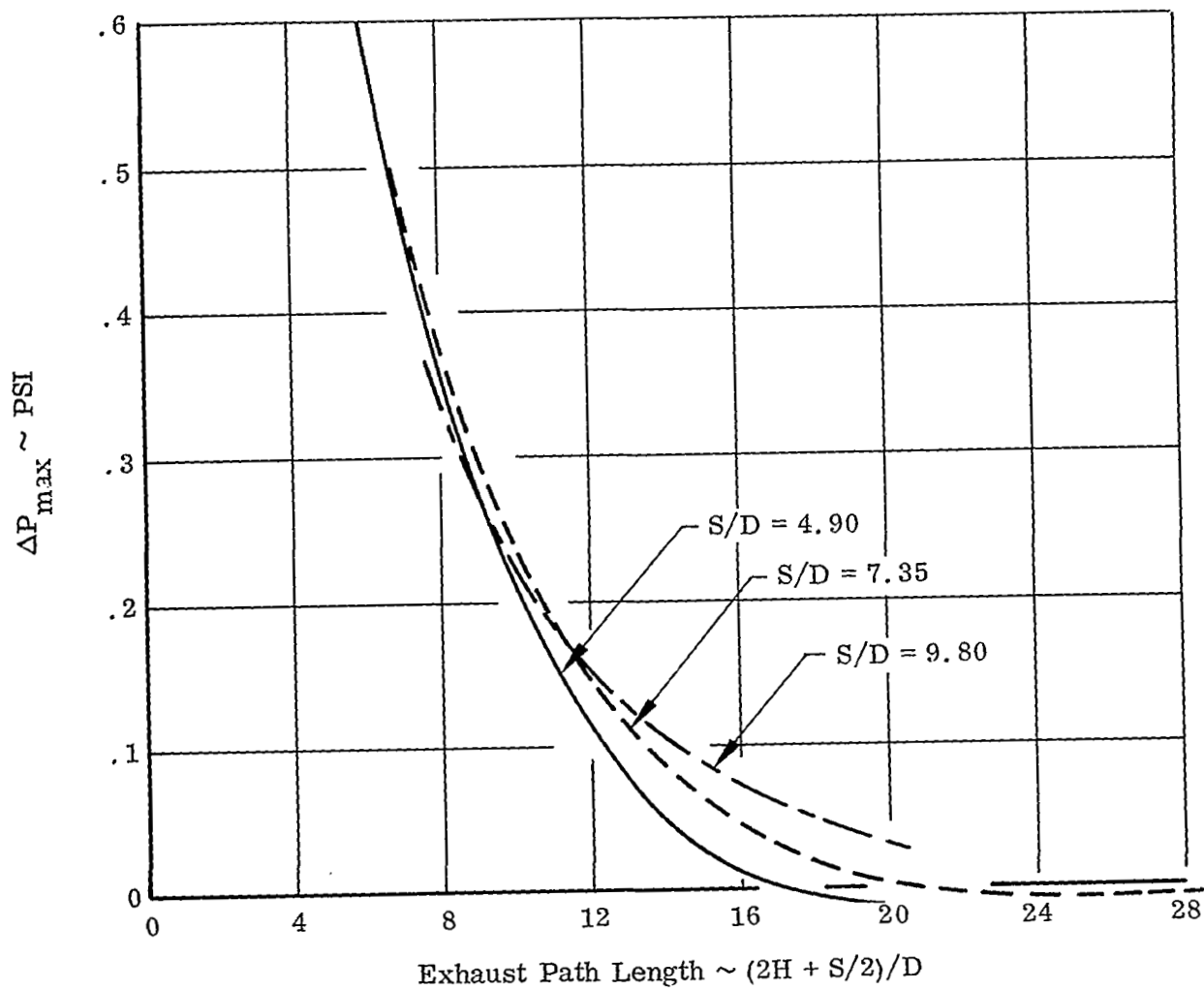
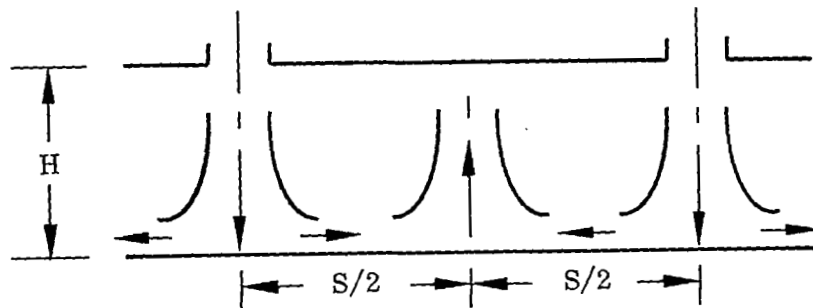
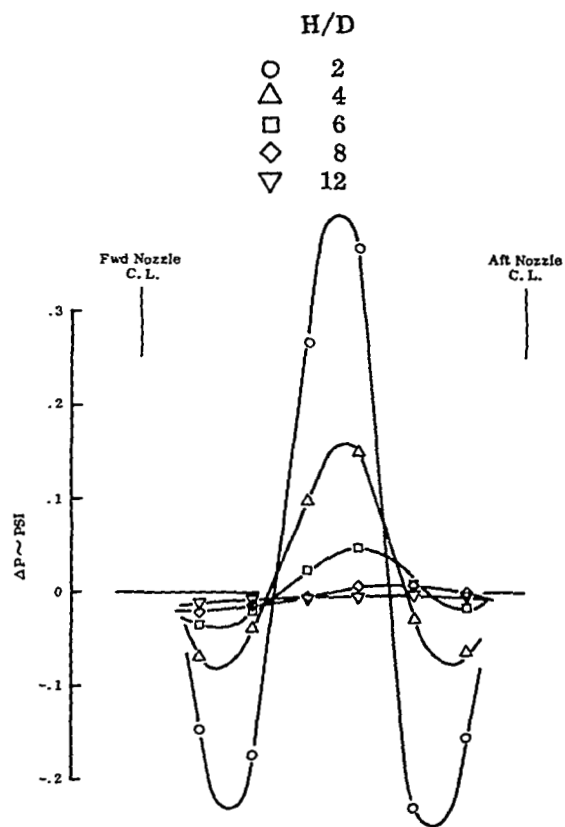
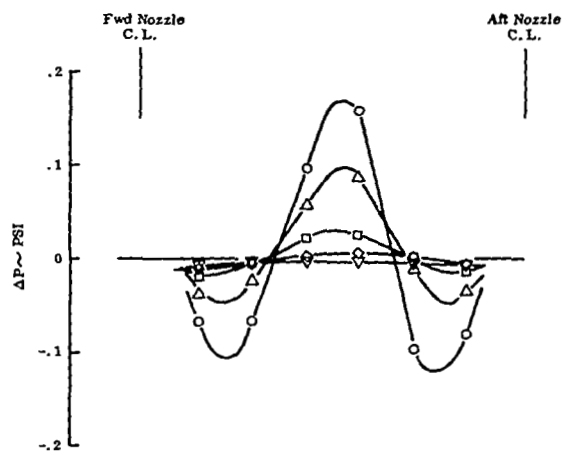


FIGURE 48. EFFECT OF EXHAUST PATH LENGTH ON POD PEAK PRESSURE

Two Engine Operation  
 $S/D = 7.35$   
 Wind < 3 MPH



(a) Turbojet



(b) Turbofan

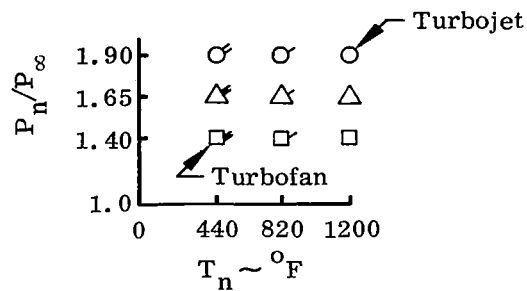
FIGURE 49. EFFECT OF H/D ON POD PRESSURE DISTRIBUTION - LOW WIND

Two Engine Operation

$H/D = 4$

$S/D = 7.35$

Wind < 3 MPH



Exhaust Pressure/Temperature  
Matrix

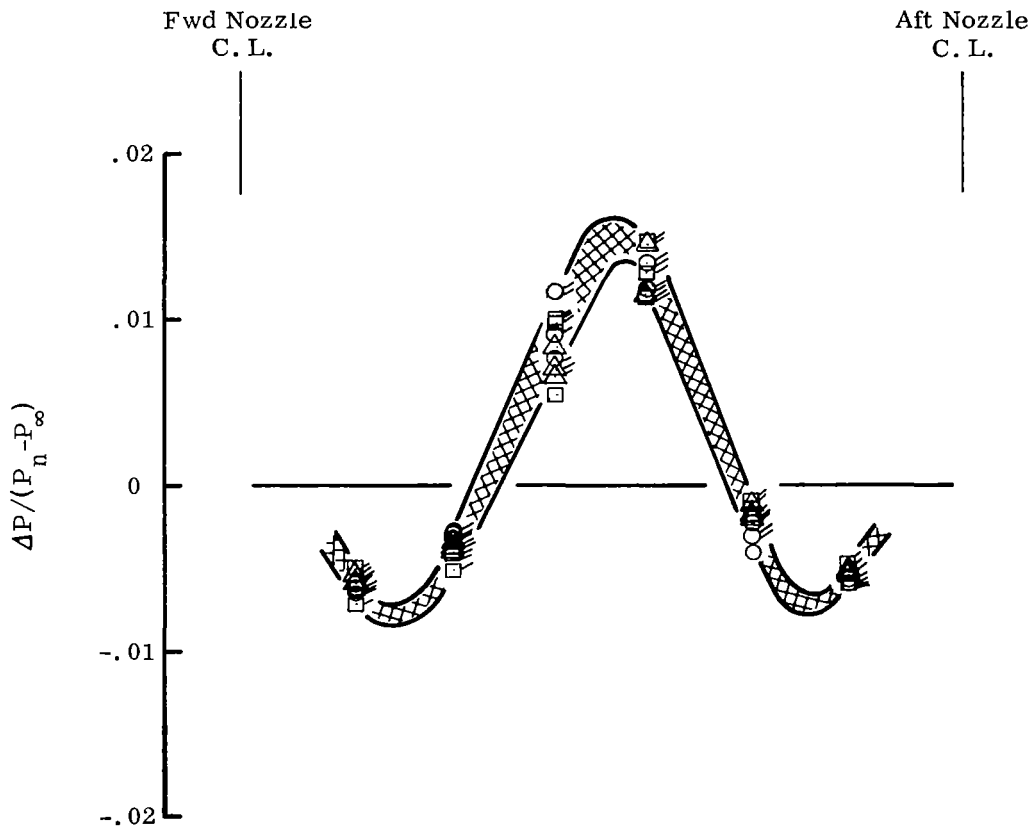


FIGURE 50. EFFECT OF EXHAUST PRESSURE RATIO AND TEMPERATURE  
ON NON-DIMENSIONAL POD PRESSURE DISTRIBUTION

Two Engine Operation  
 Turbojet  
 $H/D = 4$   
 $S/D = 7.35$

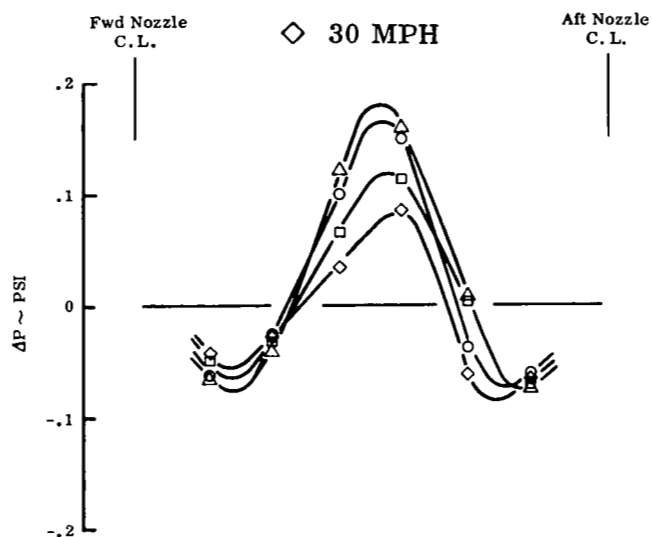
Wind

○ < 3 MPH

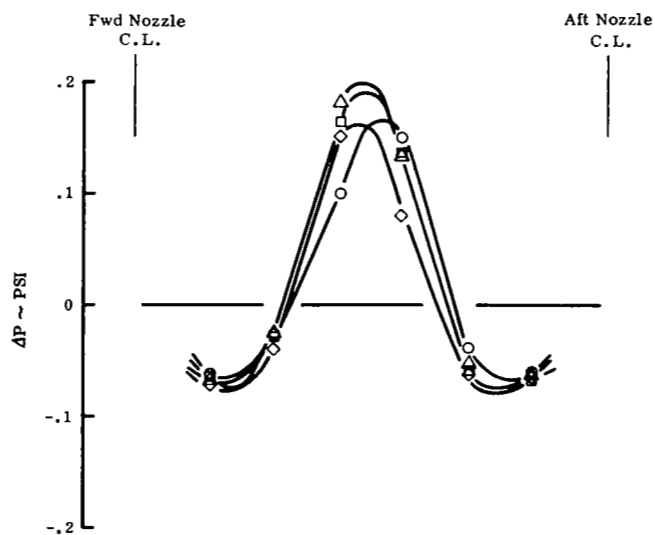
△ 10 MPH

□ 20 MPH

◇ 30 MPH



(a) Headwind



(b) Crosswind

FIGURE 51. EFFECT OF WIND ON POD PRESSURE DISTRIBUTION - TURBOJET

Two Engine Operation  
 Turbofan  
 $H/D = 4$   
 $S/D = 7.35$

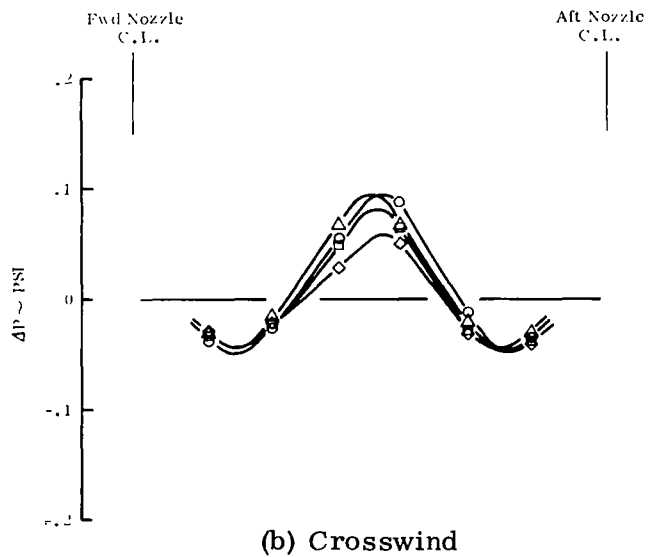
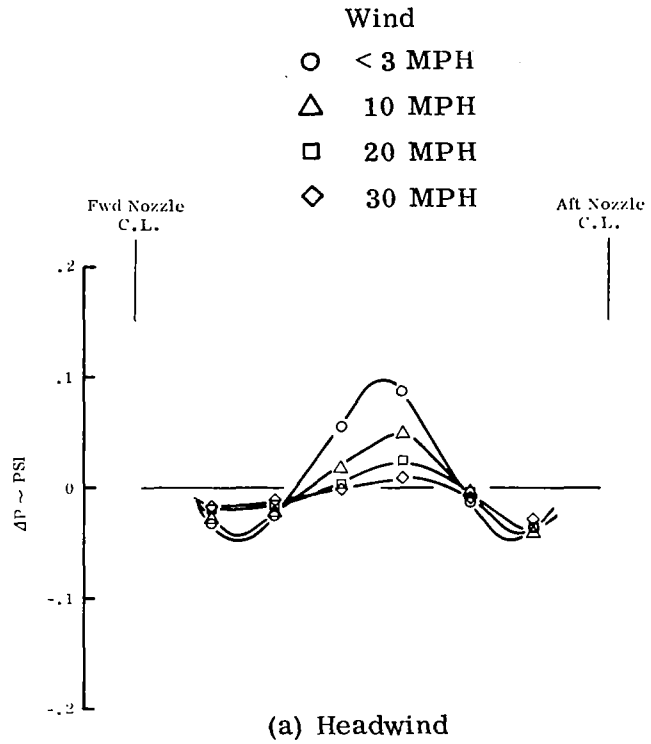


FIGURE 52. EFFECT OF WIND ON POD PRESSURE DISTRIBUTION - TURBOFAN

Two Engine Operation  
 $H/D = 4$   
 $S/D = 7.35$

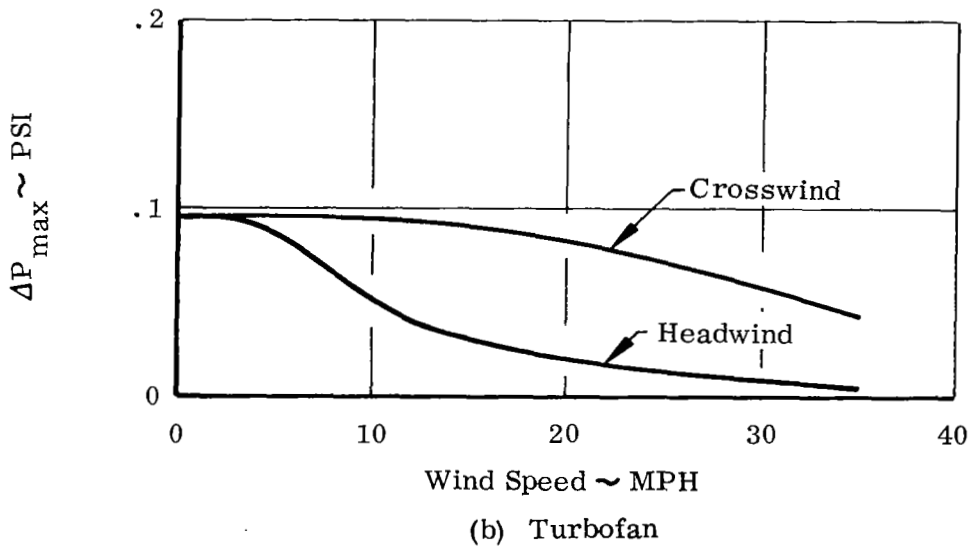
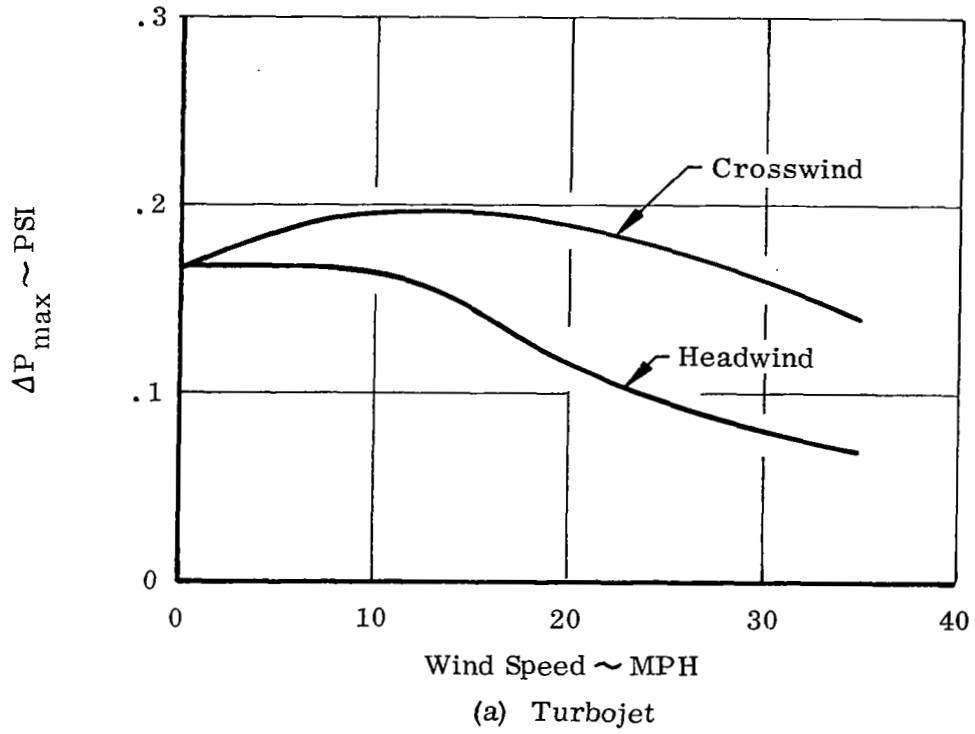


FIGURE 53. EFFECT OF WIND ON POD PEAK PRESSURE

Two Engine Operation  
 Turbojet  
 $S/D = 7.35$   
 Wind = 20 MPH

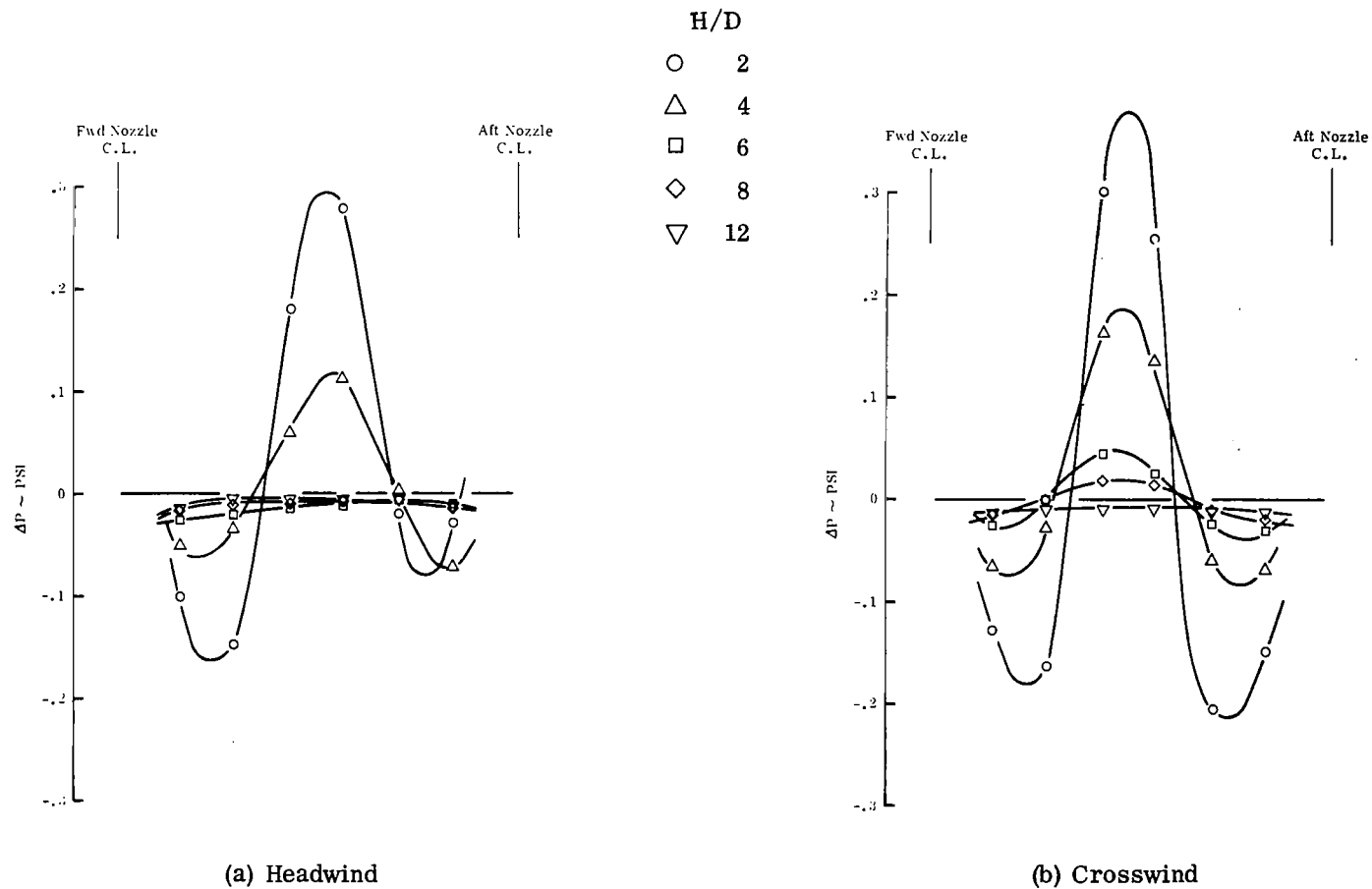


FIGURE 54. EFFECT OF H/D ON POD PRESSURE DISTRIBUTION  
 AT HIGH WIND CONDITIONS

Two Engine Operation  
Turbojet  
S/D = 7.35

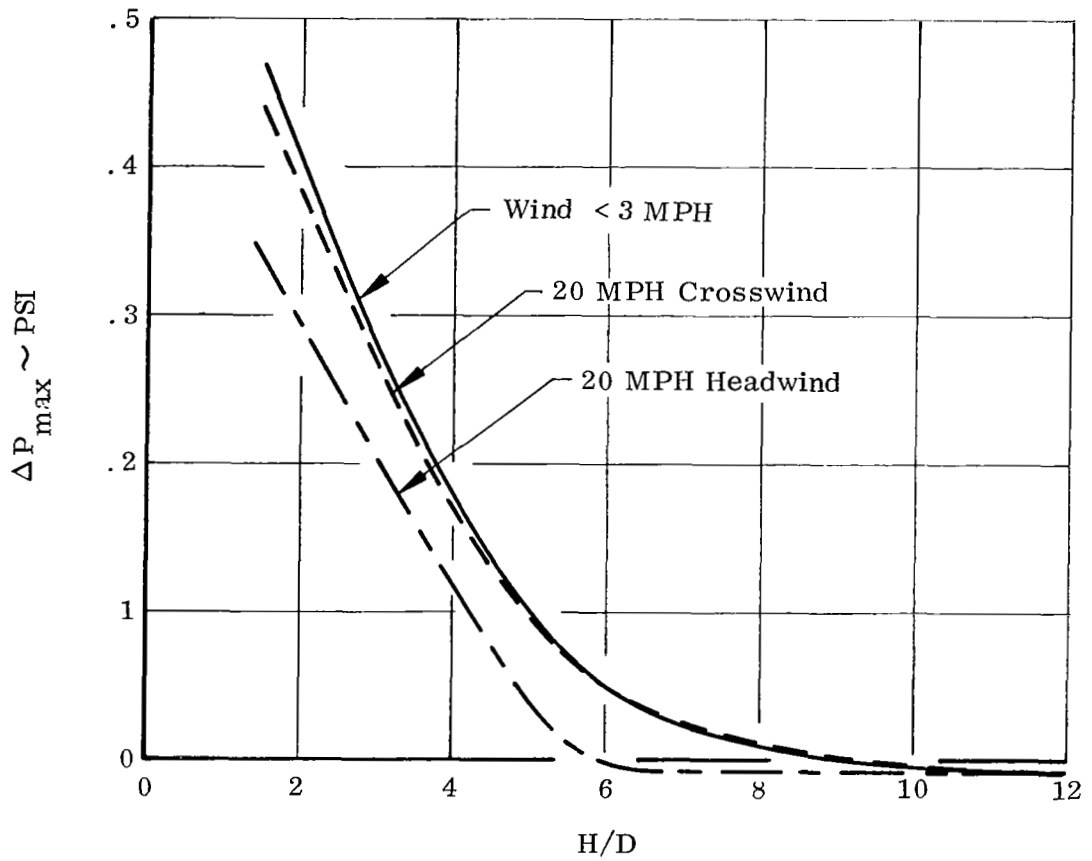


FIGURE 55. EFFECT OF WIND ON POD PEAK PRESSURE



# Single Engine Operation

$$H/D = 4$$

$$S/D = 7.35$$

## Wind

○ < 3 MPH

△ 10 MPH

□ 20 MPH

▽ 30 MPH

Headwind

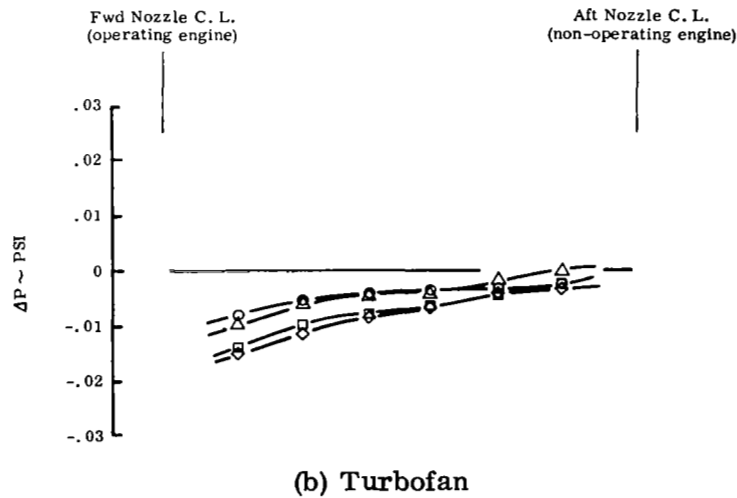
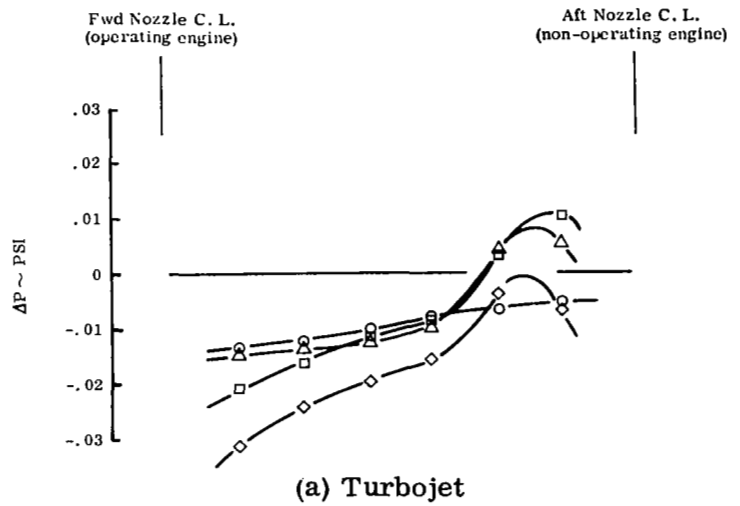


FIGURE 56. EFFECT OF WIND ON POD PRESSURE DISTRIBUTION

Two Engine Operation  
Turbojet  
S/D = 7.35  
Wind < 3 MPH

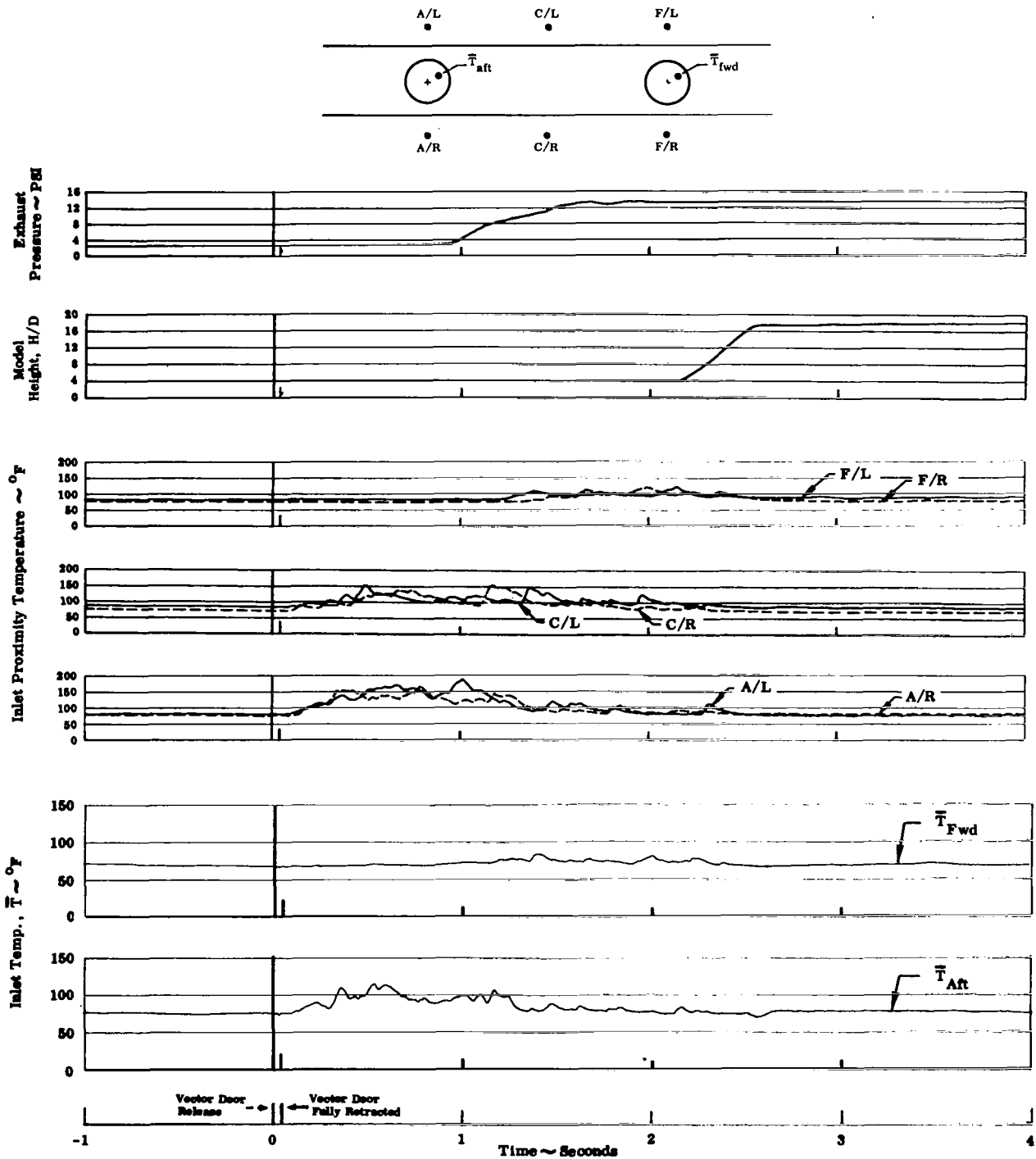


FIGURE 57. TAKE-OFF TRANSIENT - LOW WIND

Two Engine Operation  
Turbojet  
 $S/D = 7.35$   
Wind = 20 MPH Headwind

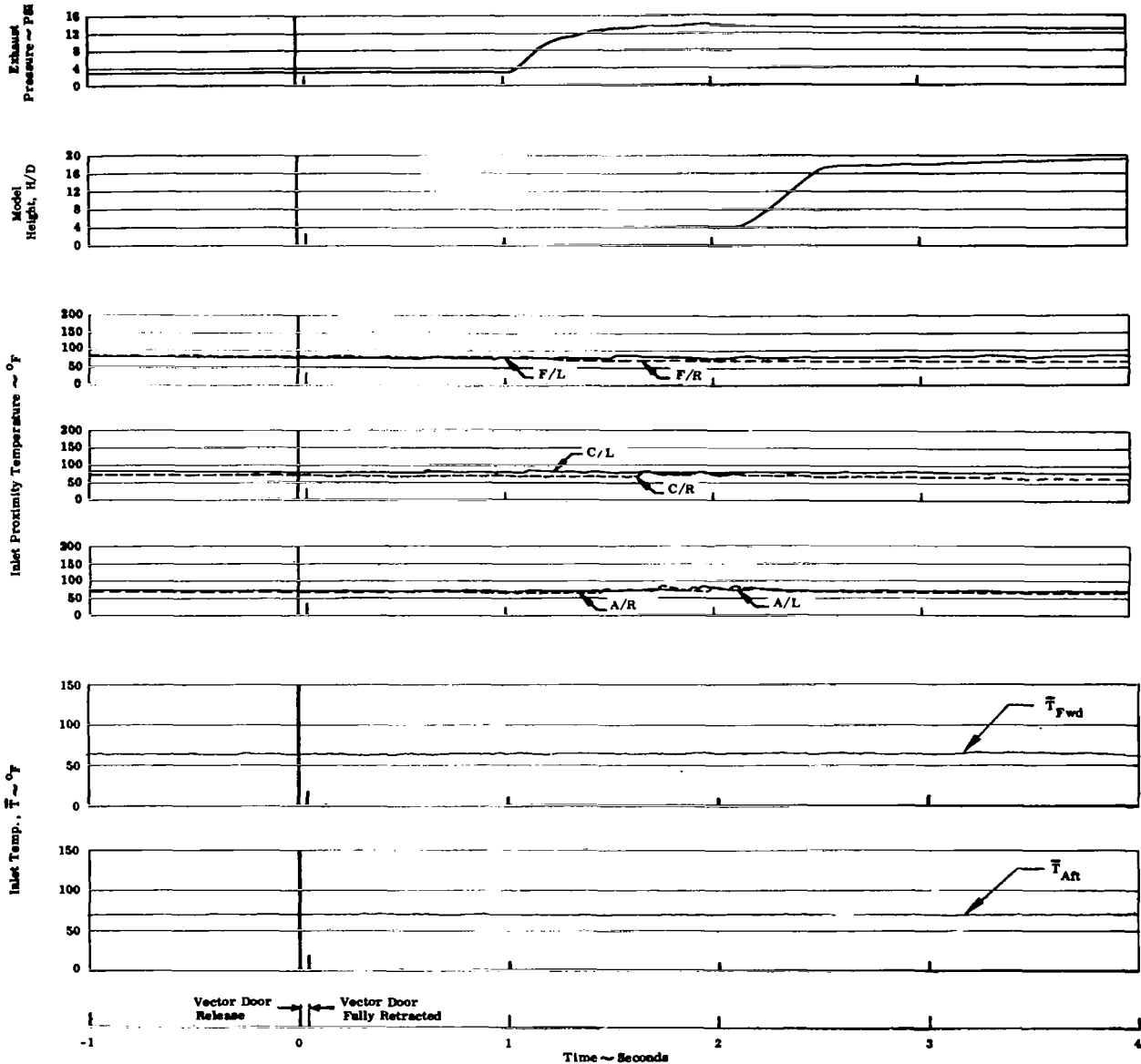
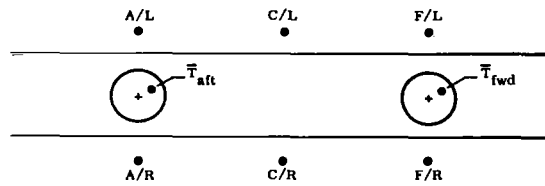


FIGURE 58. TAKE-OFF TRANSIENT - 20 MPH HEADWIND

Two Engine Operation  
Turbojet  
S/D = 7.35  
Wind = 20 MPH Crosswind

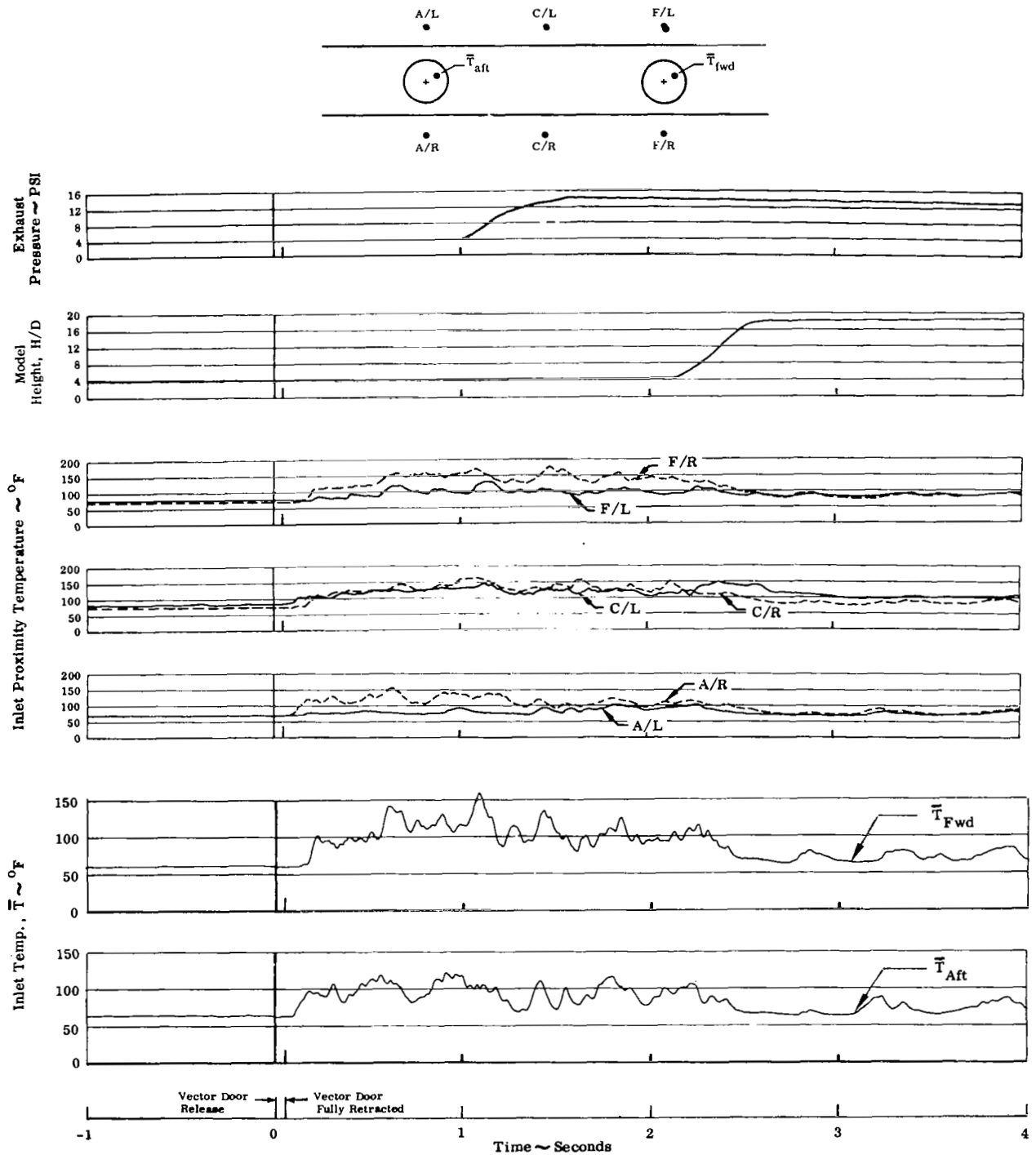


FIGURE 59. TAKE-OFF TRANSIENT - 20 MPH CROSSWIND

Two Engine Operation  
Turbofan  
S/D = 7.35  
Wind < 3 MPH

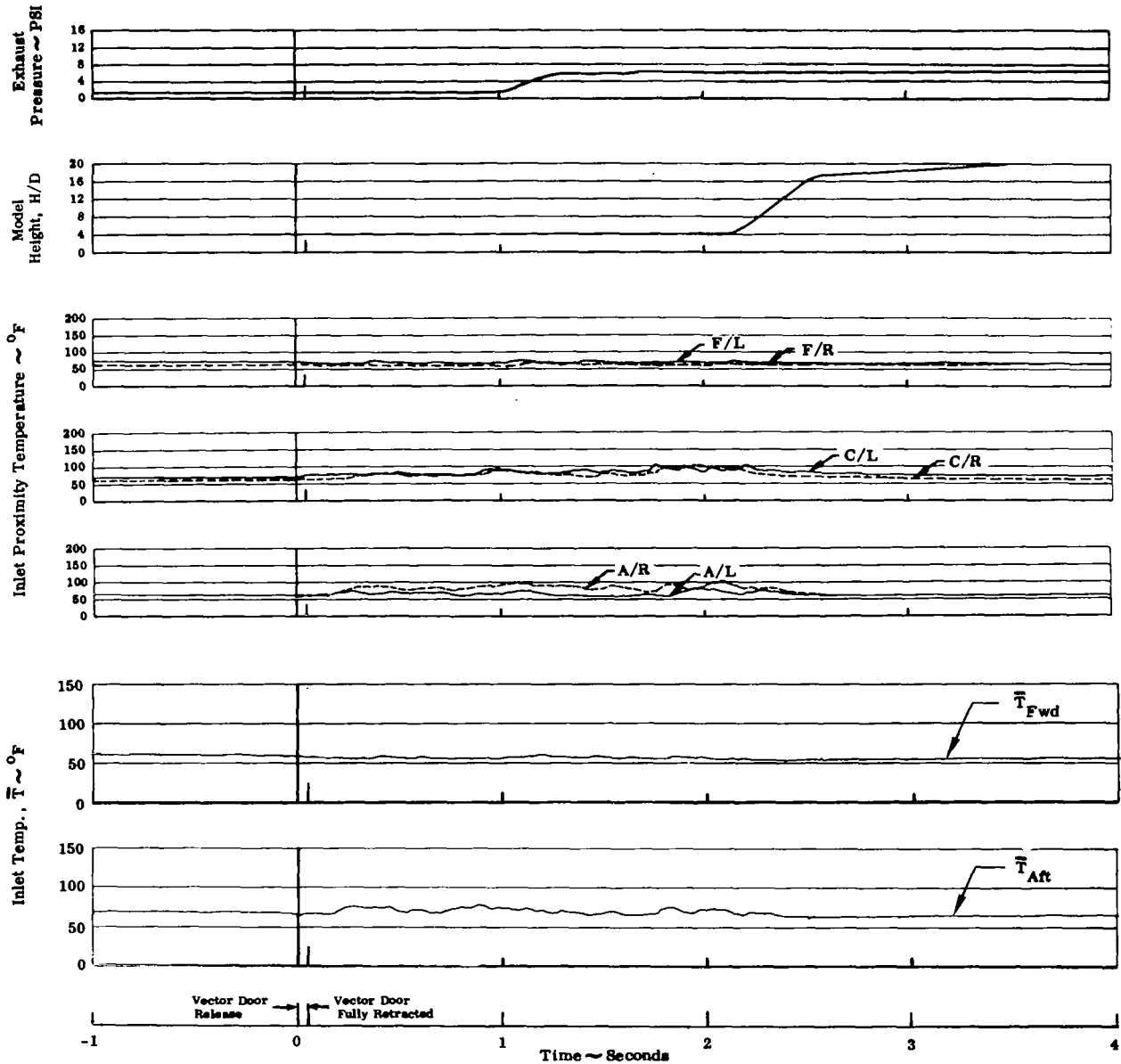
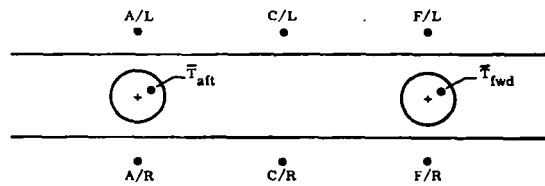


FIGURE 60. TAKE-OFF TRANSIENT - LOW WIND

Single Engine Operation  
Turbojet  
S/D = 7.35  
Wind < 3 MPH

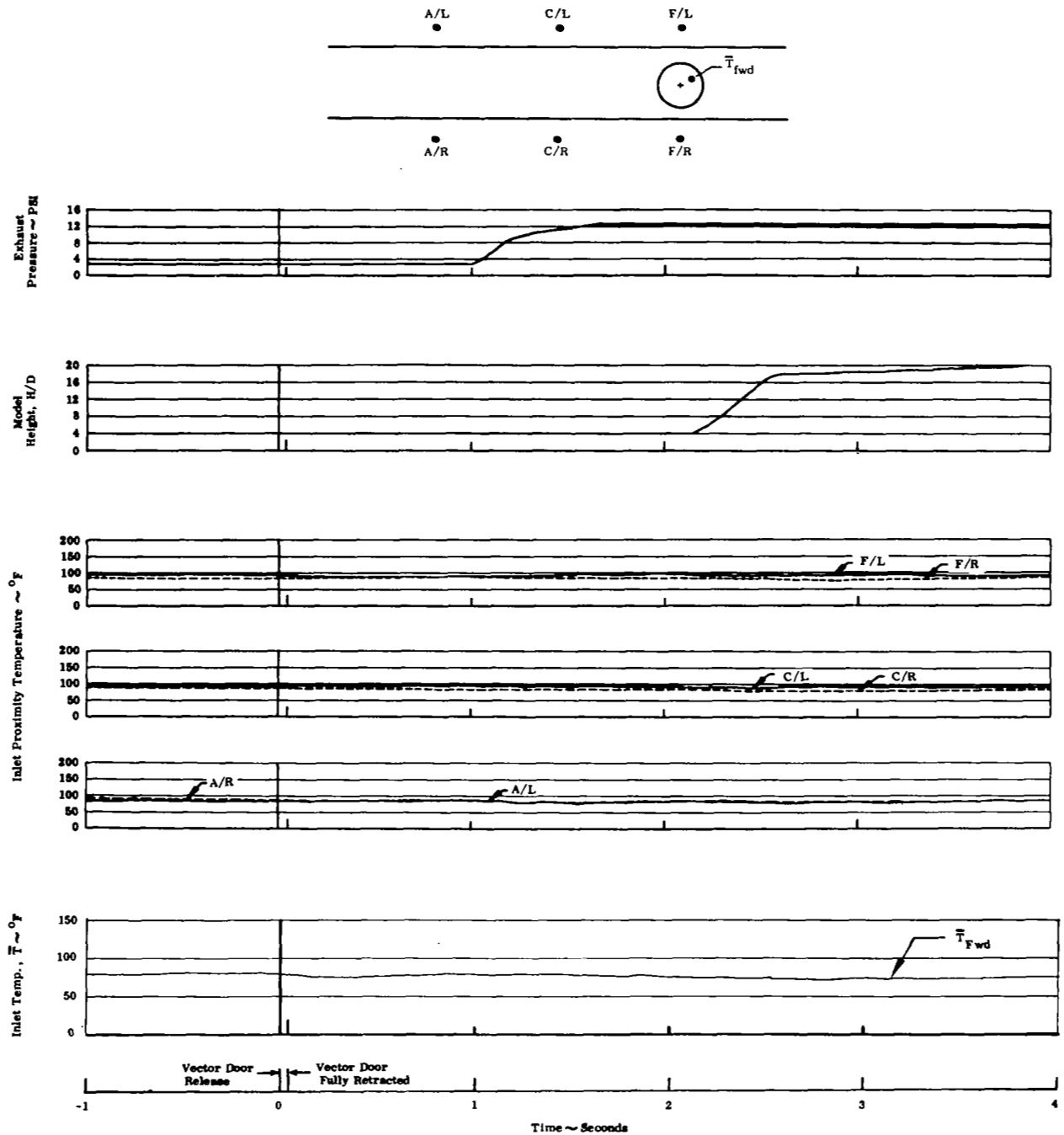


FIGURE 61. TAKE-OFF TRANSIENT - LOW WIND

Two Engine Operation  
Turbojet  
S/D = 7.35  
Wind < 3 MPH

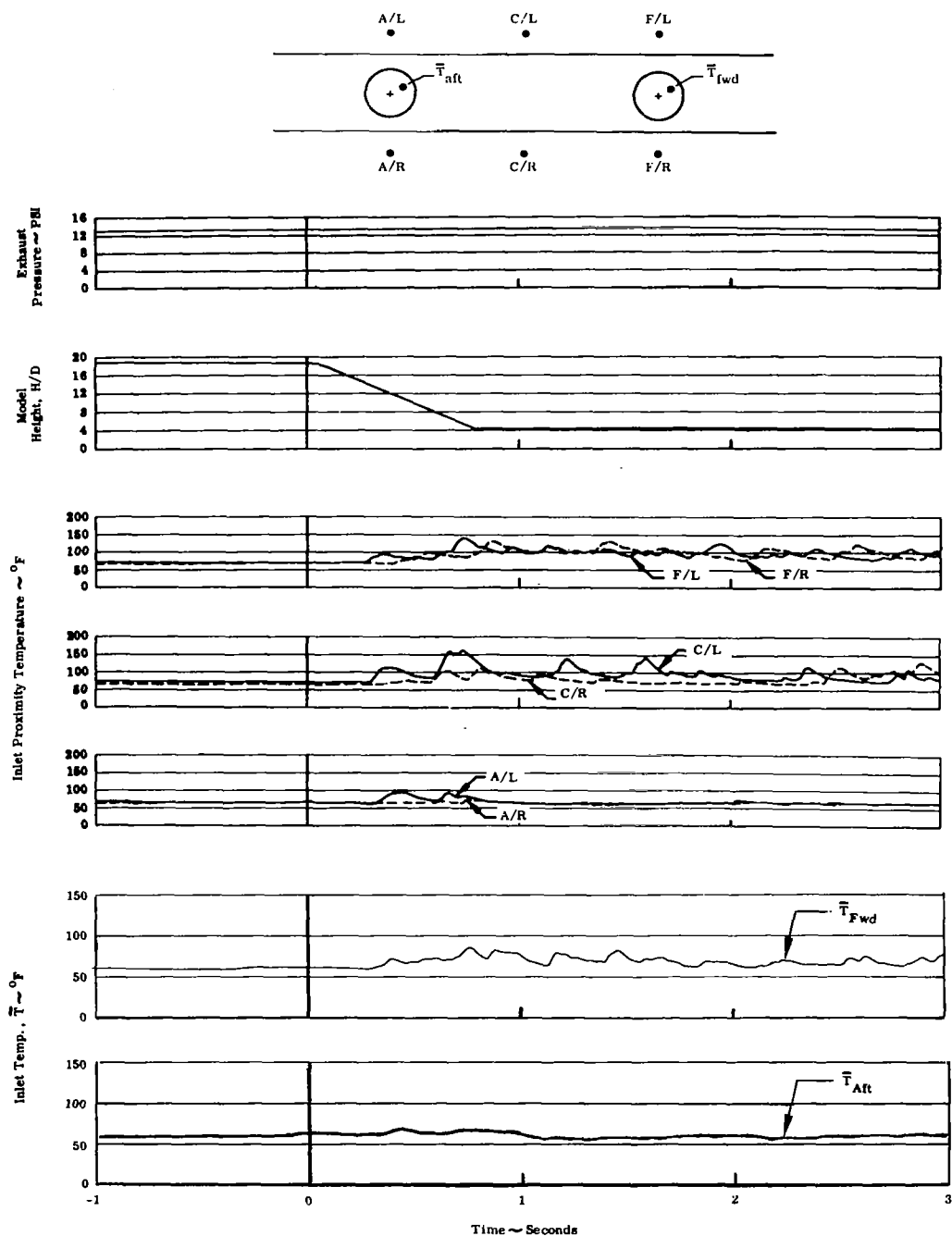


FIGURE 62. LANDING TRANSIENT - LOW WIND

Two Engine Operation  
Turbojet  
S/D = 7.35  
Wind = 20 MPH Headwind

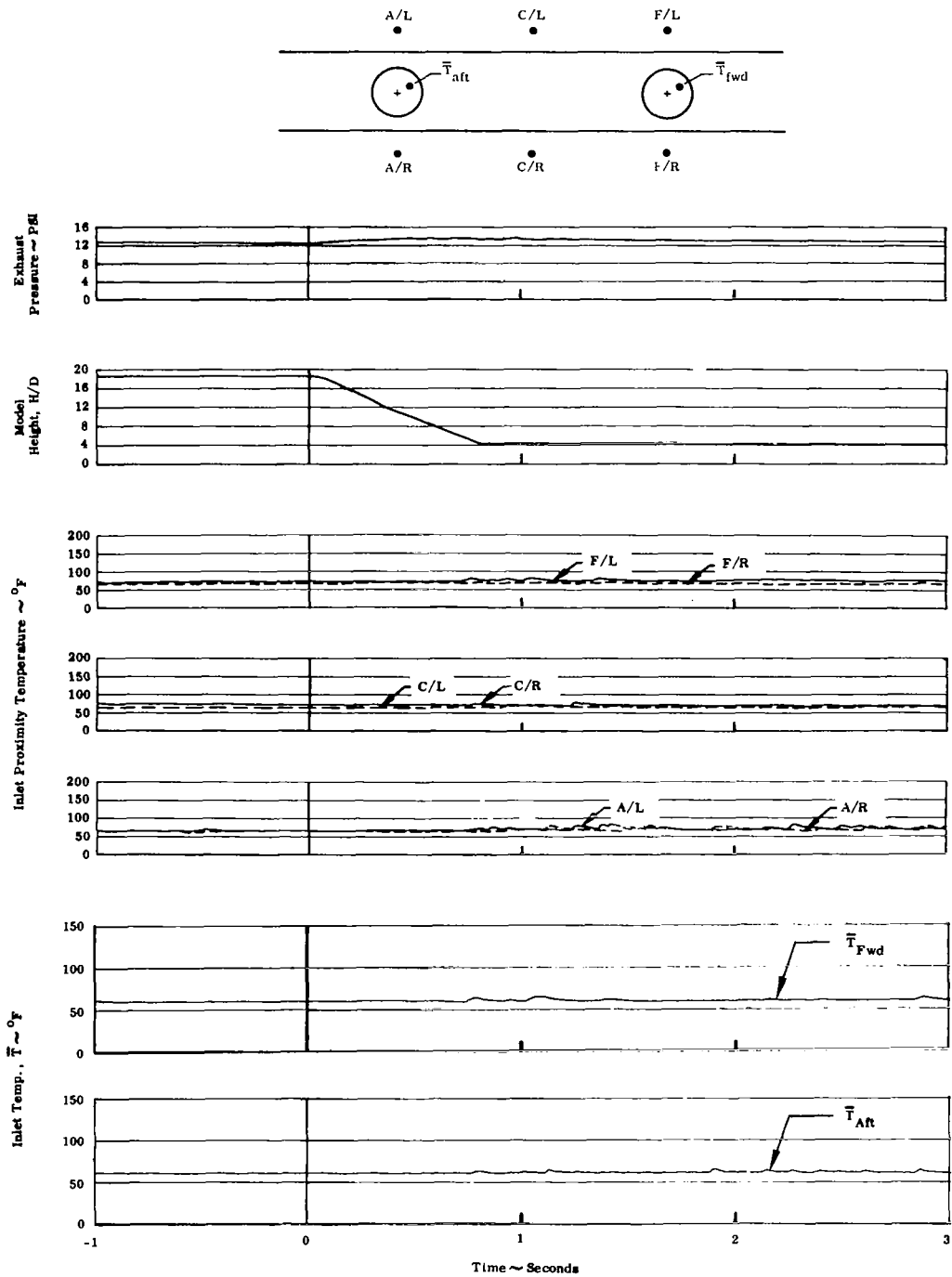


FIGURE 63. LANDING TRANSIENT - 20 MPH HEADWIND



Two Engine Operation  
Turbojet  
S/D = 7.35  
Wind = 20 MPH Crosswind

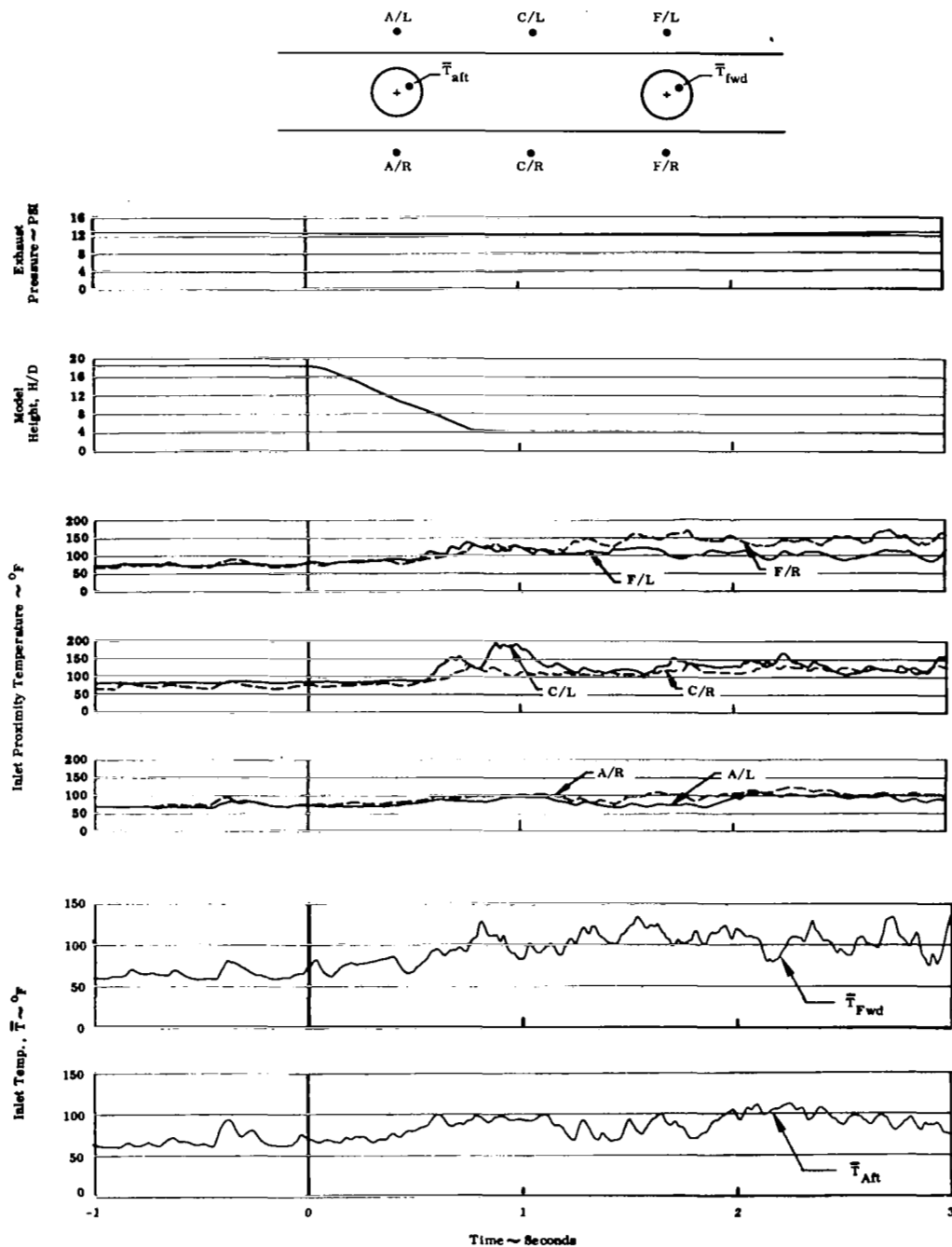


FIGURE 64. LANDING TRANSIENT - 20 MPH CROSSWIND

Two Engine Operation  
Turbofan  
S/D = 7.35  
Wind < 3 MPH

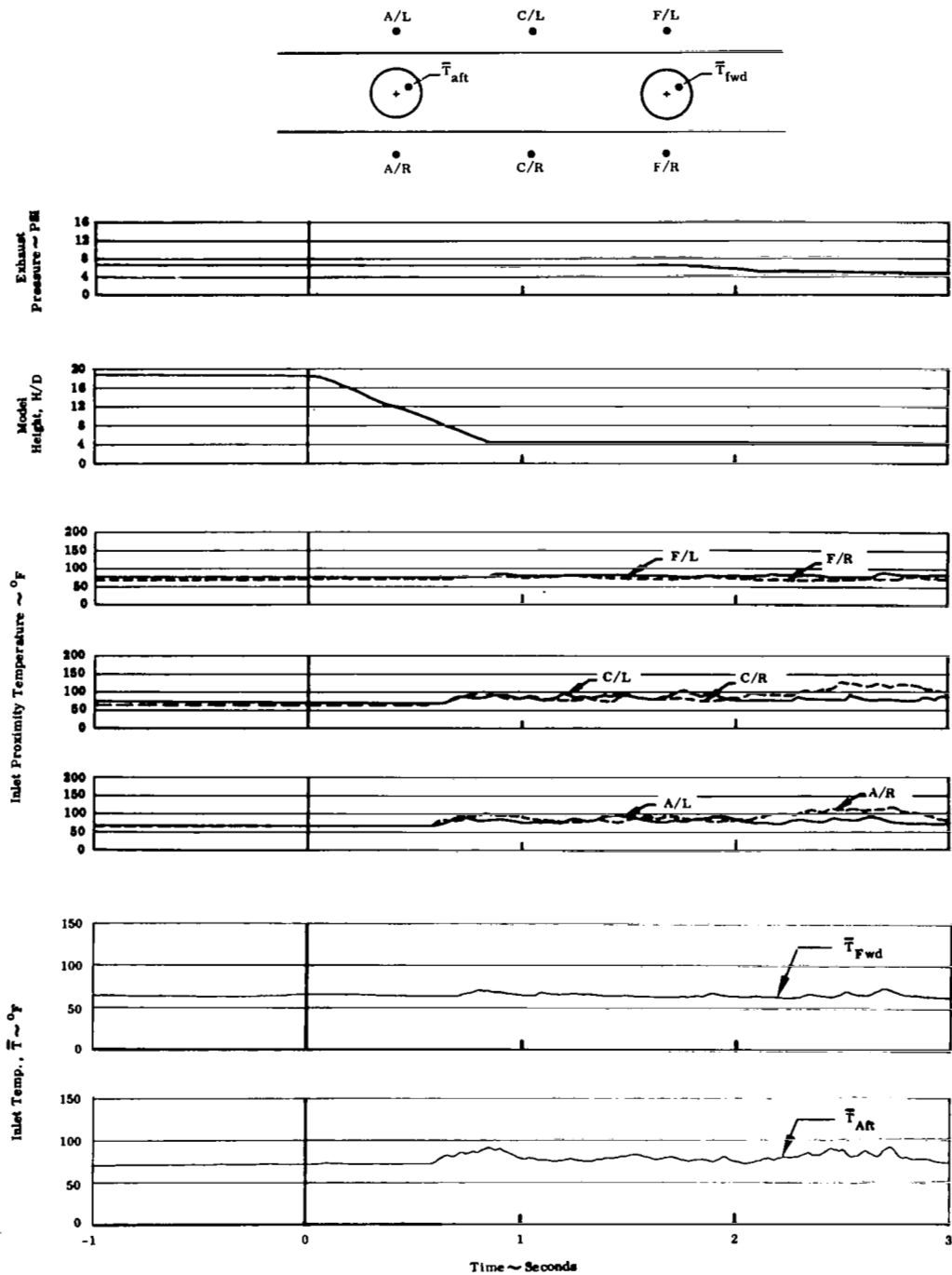


FIGURE 65. LANDING TRANSIENT - LOW WIND

Single Engine Operation  
Turbojet  
S/D = 7.35  
Wind < 3 MPH

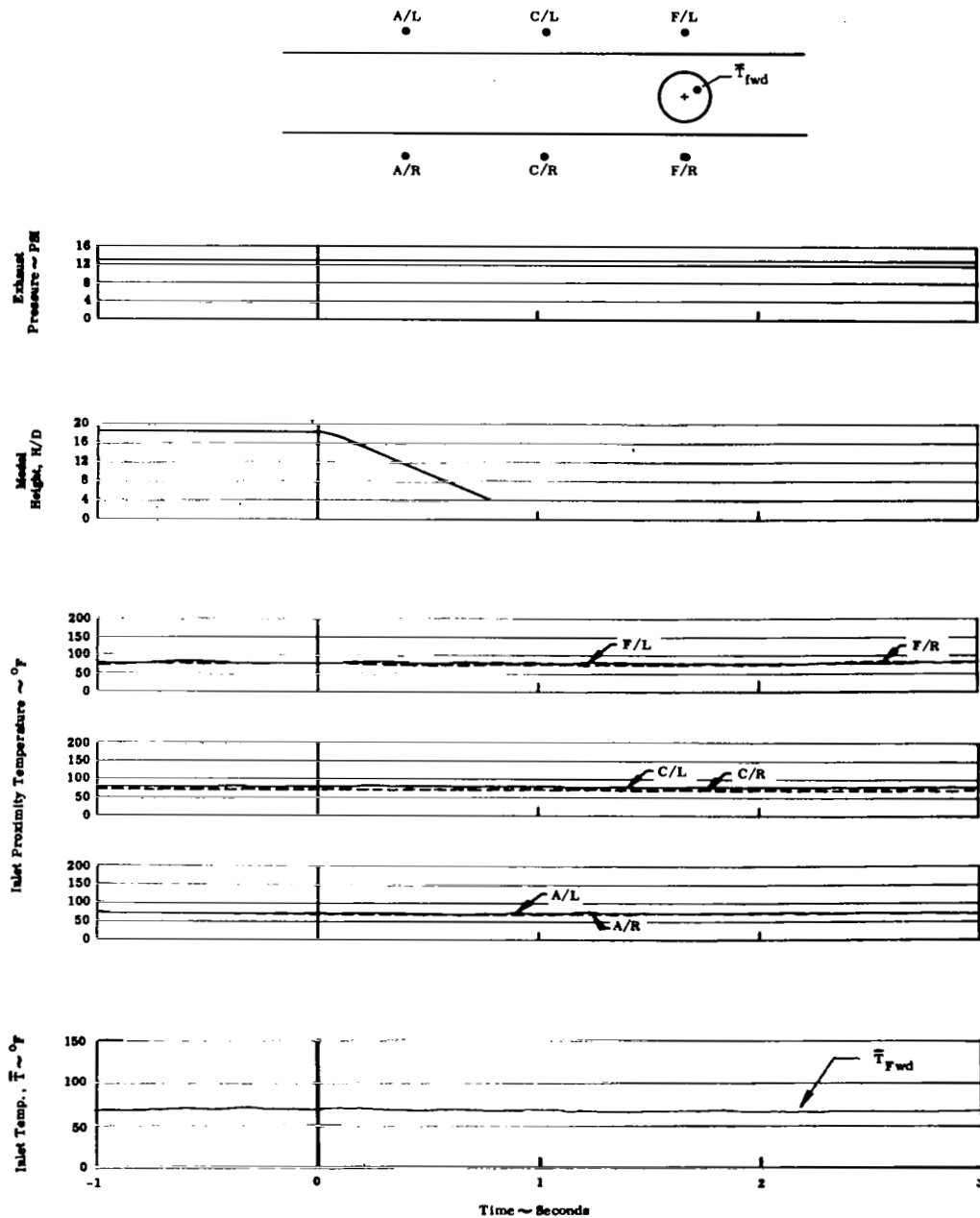


FIGURE 66. LANDING TRANSIENT - LOW WIND